UNIVERSITÀ DEGLI STUDI DI GENOVA

Dibris

ISTITUTO ITALIANO DI TECNOLOGIA

University of Genova-Istituto Italiano di Tecnologia

Bionanotechnology (DIBRIS)

XXX cycle

Multifunctional and Responsive Textile Nanocomposites for High Value Applications

Muhammad Zahid

3997886

Tutors:

Dr. Athanassia Athanassiou

Dr. Ilker S. Bayer

Genova, February 2018

Overview

Textile based multifunctional nanocomposites are getting more popular because of their enhanced technical features together with wearability aspects. Conventional fabrics after surface modifications using nanotechnologies and functional polymers have several applications, such as, water-repelling fabrics, smart fabrics, antibacterial, UV protective and electromagnetic shielding fabrics, sportswear, military uniforms, sensors and medical dressings. For this, synthetic fabrics like polyester, nylon, aramid, are preferred due to their high mechanical strength and resistance to applied chemical finishes, however, these synthetic fabrics don’t degrade in nature and cause environmental pollution. On the other hand, natural cotton fabrics with non-toxic, eco-friendly functional finishes can easily degrade and eliminate these environmental problems.

This thesis aims to develop cotton fabric based multifunctional nanocomposites using simple fabrication techniques. Surface modification of cotton fabrics with environmental friendly, non-toxic polymeric coatings have been demonstrated for superhydrophobic, conductive, self-cleaning and antibacterial textiles. After a general introduction about conventional and functional textiles, some state of the art developments, their realistic features and drawbacks have been discussed in the first chapter. Subsequently, this thesis have been divided into 4 independent parts with detailed results and discussions for imparted functionalities as follow,

- The first part is dedicated to fabricate superhydrophobic cotton fabrics using a sustainable, environmental friendly treatment approach. A multilayer superhydrophobic treatment have been developed with minimal amount of C6 fluorinated chemicals.
- In the second part, highly conductive cotton fabrics have been developed for strain-sensing and supercapacitor applications. A synergic effects of PEDOT:PSS conductive polymer and graphene on electrical conductivity of cotton fabrics have been studied.
- The third part demonstrates a simple and scalable process to produce antibacterial and self-cleaning cotton fabrics using photocatalytic Mn-doped TiO_2 nanoparticles. Photocatalytic degradation of a colouring dye and antibacterial properties have been characterized under both ultraviolent and visible irradiations.
- Last part describes a simple and efficient recycling process for textile fabric wastes. An energy efficient route of cellulose dissolution into trifluoroacetic acid (TFA) solvent and then solution casting, have been demonstrated to regenerate amorphous cellulose films. Furthermore, graphene nanofillers are mixed with cellulose solutions for thermal and electrical properties.

Acknowledgements

First and foremost thanks to Dr. Athanassia Athanassiou who has been there as my tutor for the whole 3 years and providing me this opportunity to work in an interdisciplinary group as Smart Materials. Many thanks are also due to Dr. Ilker S. Bayer for supervising me during all my research activities and being such generous in his support and constructive ideas. Thanks for being an example to follow. I would like to thank the technicians of Smart Materials (Lara, Riccardo, Marco and Giorgio) for their availability and infinite help. Also thanks to all the Smart Materials Group, especially Dr. Jose A. Heredia-Guerrero and Luca Ceseracciu for our collaborations. I cannot forget my other fellows: Muhammad Tamoor Masood, Pietro Cataldi and Aldo Pignatelli.

I have also to thank my family, in particular my parents, for their prayers and motivation. Also you my little angel, my Bablu, Haniya thanks a lot. Finally thank you, Zareen Gull, my wife and my better half for your infinite patience and devotion during all these years. Without you nothing would have been possible. Thanks.

Table of Contents

Chapter: 1 Functional textiles; background, state of the art and prospectives

Chapter: 2 Fabrication of hydrophobic cotton fabrics by sustainable materials

Chapter: 3 PEDOT:PSS/Graphene based conductive cotton fabrics

Chapter: 4 Mn-Doped TiO_2 Nanoparticles for Antibacterial and Self-Cleaning Fabrics

Chapter: 5 Thermal interface materials (TIMs) from regenerated cellulose

Chapter: 1

Functional textiles; background, state of the art and prospectives

1.1 Background

Functional textiles are the textiles used for their extended features, for instance, antibacterial, flame retardancy, UV protection, anti-static, water repelling and electro-conductivity, instead of their aesthetic and decorative purposes[1,2]. On the other hand, conventional textiles are preferred for their wearability, softness and comfort. Our ancestors learned to use them as long as more than 30,000 years ago. For clothing, short stapled fibres or continuous filaments are spun into yarns/threads, and then these yarns are intermeshed/interlaced together to form a 3D structure named as fabric.

In the beginning, textile was a product of home industry and people produced textile to meet their own needs. Once production exceeded their own needs, the textiles were traded for other goods. Thanks to industrial revolution around 1760, textile could be produced more cheaply and in much larger quantities using the steam engine driven mechanical looms (a machine to produce fabric)[3]. This was necessary because the population was growing exponentially. Therefore, the weaving process turned into a processing industry. At that time most of the textile fabrics consist of natural materials, such as, cotton, linen, wool and silk. However, due to limited availability of natural resources, synthetic materials were adopted. In 1930, first synthetic fibre nylon was made and later, for example, polyester followed in the 20th century[4]. These days synthetic fibres are still being invented from petroleum resources. Fig. 1.1 shows classifications of different natural and synthetic fibres, their origins and possible processing techniques[5].

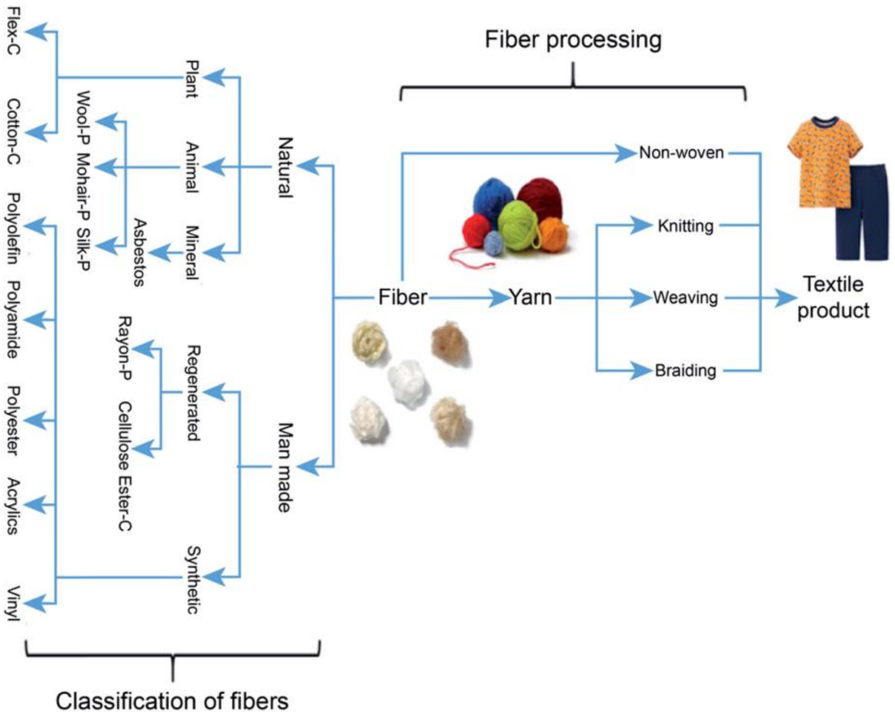

Fig. 1.1. Classifications of textile fibers and their processing techniques

In 2016, the global consumption of textile fibre for fabric production was reported at 99 million tons with 1.5% annual growth. Synthetic fibres were leading with 62.7% market share followed by cotton fibres at 24.3% (Source; Lenzing AG)[6]. Despite their unmatched comfort, resilience, biocompatibility and nonabrasiveness[7], annual consumption of natural cotton is far behind their counter parts (synthetic fibers). Some of the main reasons behind this are their hygroscopic nature, low chemical and microbial resistance. Therefore, majority of the conventional textile products are made from natural (like cotton) materials but their technical applications are rare. Despite these delicate characteristics, these natural fibres can easily be modified for technical applications using different surface finishes and treatments.

Nowadays, there is a new revolution on the textile industry with apparition of new technologies that could add special functions and properties to the fabrics. For example, there has been significant improvement in functionalities on textile, like, antibacterial/anti-odour fabrics, antistatic fabrics, self-cleaning fabrics, hydrophobic fabrics, conductive fabrics, wearable sensors, UV protective fabrics and fabrics reinforced composites, as shown in Fig. 1.2[8,9]. In this sense, functional polymers and nanoparticles play a key and significant role in this technological evolution since they show outstanding surface properties that allow to multiply their effect in comparison with bulky traditional additives and materials.

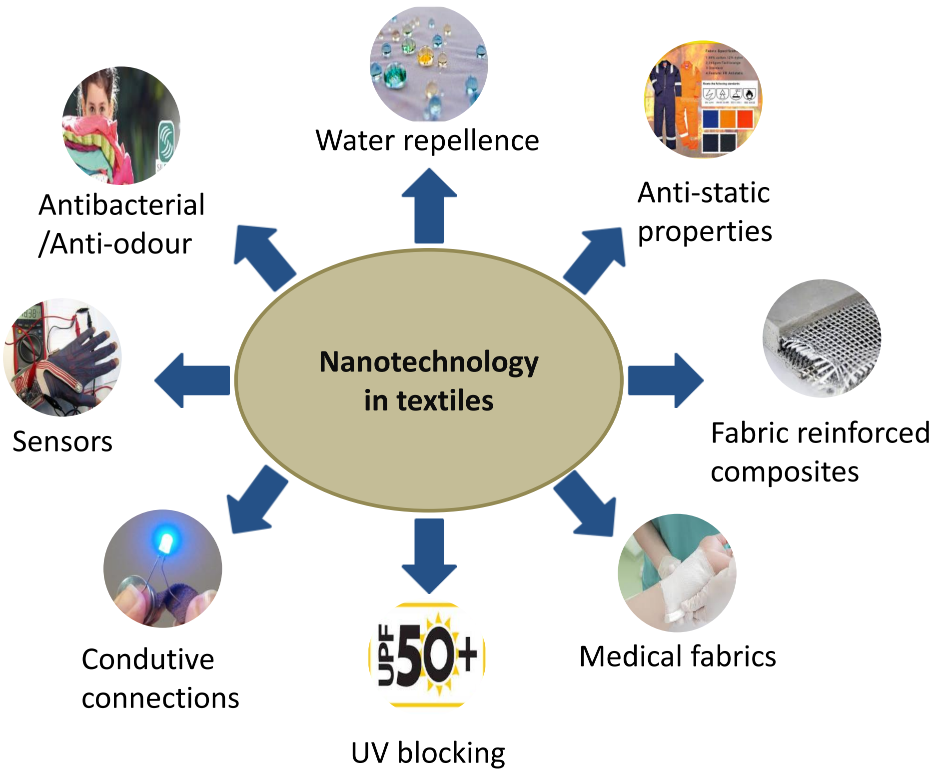

Fig. 1.2. Types of functional textiles functionalized with nanotechnologies (Source: google images).

1.2 State of the art technologies

The use of textile fabrics for technical applications was started with the invention of synthetic fibres in 19th century. Initially, textiles fabrics were made for high strength applications, namely, aramids, glass and carbon fibers. Later, with the advancements in nanotechnology and polymer chemistry, several other functionalities were also imparted to natural and synthetic textiles. Although, some other techniques of functionalizing textile fabrics are also present, for instance, additive manufacturing at fibre spinning stage and plasma treatments, post surface modifications by functional polymers are more advantageous[10]. They can be adopted using several simple and scalable fabrication techniques, such as, dip coating, *in-situ* polymerization, chemical vapour deposition (CVD), layer-by-layer (LBL) deposition, spray coating and flat-bed rod coating. In the following sections, some interesting functional features imparted to textile fabrics will be described with literature review.

1.2.1 Hydrophobic and water repelling textiles

Naturally occurring plants, such as, lotus leaf demonstrate excellent water repelling and self-cleaning properties. Rain droplets don’t spread on these surfaces and form spherical shapes. A slight inclination of the surface makes droplet roll-off and take up any dirt particle on its way to down. Microscopic study of the lotus leaf exhibited presence of several papillae on the surface having hierarchical structures and specific waxes[11,12], as shown in Fig. 1.3. Low surface free energy waxes backed by micro/nano-structured papillae (2-5 µm) were responsible for this superhydrophic nature of the lotus leaf with water contact angle (WCA) and water roll-off angle (WRA) around 160° and 2°, respectively.

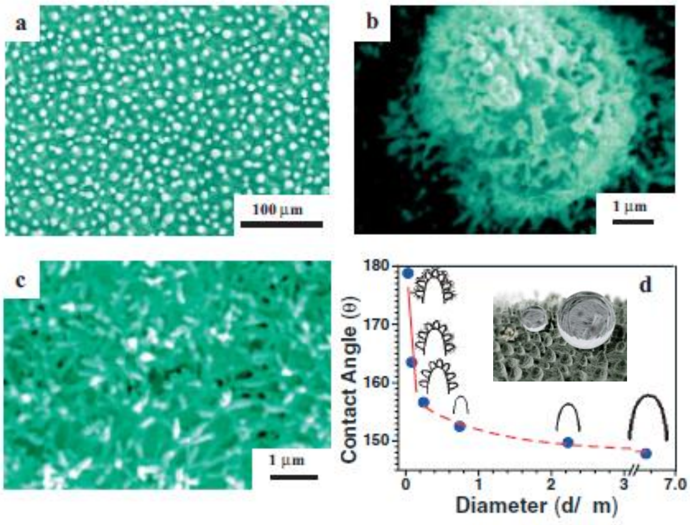

Fig. 1.3. (a) large-area SEM images of lotus leaf, (b) enlarged image of single papilla, (c) lower surface of the lotus leaf and (d) the fitted curve based on calculated data of water contact angle and geometrical size of papilla[11].

In the recent decades, an increasing number of efforts have been made to mimic aforementioned lotus leaf effect for many applications, such as, sports, fashion, military uniforms, weather protections, packaging. For this, surface modification technique using low surface free energy polymer coatings with incorporated nanostructures, such as, silica nanoparticles, silver nanoparticles and ZnO nanorods etc are of great interest for academia and industry[10,13]. In particular, textiles fabrics functionalized with fluorinated polymers demonstrate enhanced droplet mobility on their surfaces. Fluorinated polymers, specifically with long fluorinated chains (C ≥ 8 known as C8 chemistry), have surface free energy as low as 18 mN/m[14]. Therefore, the fabric surfaces when treated with these fluorinated polymers exhibit similar surface chemistry and hydrophobic nature. Chemical structures of some commercially available polymers with C8 chemistry are shown in Fig. 1.4.

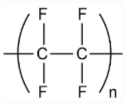

Poly(tetrafluoroethylene)
PTFE

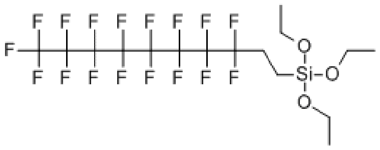

1H,1H,2H,2H-perfluorodecylethoxysilane
PFDES

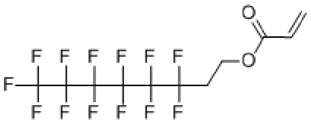

Perfluorodecyl acrylate
PFDA

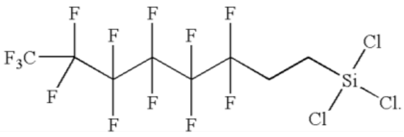

1H,1H,2H,2H-perfluorooctyltrichlorosilane
PFTS

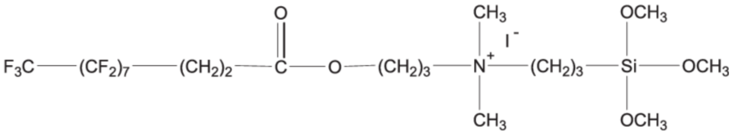

$$F_3C-(CF_2)_7-(CH_2)_2-\overset{\overset{O}{\|}}{C}-O-(CH_2)_3-\underset{CH_3}{\overset{CH_3\ \ I^-}{N^+}}-(CH_2)_3-\underset{OCH_3}{\overset{OCH_3}{Si}}-OCH_3$$

Perfluorooctylated quaternary ammonium silane coupling agent
PFOSC

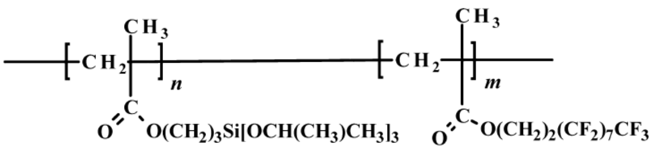

Poly [3-(triisopropyloxysilyl)propyl methacrylate]-*block*-poly-
[2-(perfluorooctyl) ethyl methacrylate]
PIPSMA-*b*-PFOEMA

Fig. 1.4. Some common perfluorinated polymer based hydrophobic finishes for textiles fabrics with C8 chemistry[15–20].

Textile fabrics treated with fluorinated polymers having C8 chemistry and blended with nanoparticles (NPs) demonstrate WCAs surpassing 150° and WRAs below 10°[15–26]. These fabrics are generally characterized as superhydrophobic fabrics. For instance, Gore-Tex is a famous commercial fabric that provides excellent water repelling and water resistance properties together with breathability[27]. Gore-Tex fabrics are prepared using poly(tetrafluoroethylene) (PTFE) coatings on polyester fabrics. An additional PTFE membrane is provided to resist the water infiltration up to 30 pounds per square inch pressure (psi). For reference, an average weighted person can exert 16 psi on his knee while kneeling down. Therefore, Gore-Tex fabrics not only repel the water droplets but also resist their transportation across the fabric. These are very important aspects of the hydrophobic textiles and hardly reported in the literatures. In Gore-Tex fabrics, these highly hydrophobic characteristics are attributed to the presence of a PTFE membrane present in fabric structures. Despite their good water repelling properties, C8 fluorinated polymers are regarded as a source of toxic chemicals in the environment. As such, when C8 fluorinated polymers degrade, they produce perfluorooctanoic acid (PFOA) and perfluorooctane sulfonate (PFOS). PFOA and PFOS have very low bio-elimination rate, are persistent in nature and likely to be carcinogenic[28,29]. Therefore, environmental protection agency (EPA) banned their excessive usage and invited major manufacturers (DuPont, 3M, etc.) to replace them with environmental friendly polymers[30]. Consequently, new C6 fluorinated polymers with ≤ 6 fluorinated carbon atoms were developed. This new generation of fluorinated polymers are environment friendly as they degrade into perfluorohexanoic acid (PFHxA) with high bio-elimination rate and non-toxicity[31]. Since then, these C6 chemicals have gained a considerable attention of commercial manufacturers and researchers. For instance, Sebdani *et al.* and Liu *et al.* have developed superhydrophobic fabrics using commercially available C6 fluorinated polymers for isotropic and anisotropic water repellencey, respectively[32,33]. In the first study, the authors developed a novel surface roughening technique using alkaline hydrolysis of PET fabrics. WRA and self-cleaning properties of C6 functionalized fabrics with chemically induced roughness were compared against SiO_2 NPs imparted superhydrophobic fabrics. Whereas, Liu *et al.* designed unidirectional hydrophobic cotton fabrics for moisture management, desalination of seawater and oil/water separation applications. Pereira *et al.* and Zhou *et al.* prepared superhydrophobic cotton fabrics using 1H,1H,2H,2H-perfluorooctyltriethoxysilne (PTES) with 6 fluorinated carbon atoms[23,34]. PTES exhibited superamphiphobic (CAs ≥ 150° for both oil and water) behaviour when mixed with SiO_2 and tetraethylorthosilicate (TEOS), however, when combined with polyaniline demonstrated a water/oil separation properties. In another study, Deng *et al.* developed a poly(1H,1H,2H,2H-nonafluorohexyl-1-acrylate) grafted superhydrophobic cotton fabric with CA exceeding 150° threshold[35], where poly(1H,1H,2H,2H-nonafluorohexyl-1-acrylate) carries only 2 fluorinated carbon atoms. Simply, textiles fabrics treated with C6 chemicals are getting more attention of the researchers because of their hydrophobicity and eco-friendly nature. Besides their nontoxicity, fluorinated polymers with decreasing number of fluorine atoms display reduced amphiphobic properties[36]. For reference, surface free energies of fluorinated polymers with increasing fluorine atoms along their backbone are given in table 1.1.

Table 1.1. Surface free energy of different fluorinated polymers[36].

Polymer	Structural formula	Critical surface free energy (dynes/cm)
Polyethylene	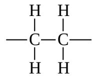 $-\overset{H}{\underset{H}{C}}-\overset{H}{\underset{H}{C}}-$	31
Poly(vinyl fluoride)	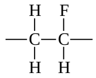 $-\overset{H}{\underset{H}{C}}-\overset{F}{\underset{H}{C}}-$	28
Poly(vinylidene fluoride)	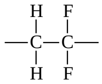 $-\overset{H}{\underset{H}{C}}-\overset{F}{\underset{F}{C}}-$	25
Polytrifluoroethylene	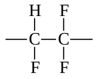 $-\overset{H}{\underset{F}{C}}-\overset{F}{\underset{F}{C}}-$	22
Polytetrafluoroethylene (PTFE)	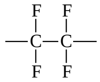 $-\overset{F}{\underset{F}{C}}-\overset{F}{\underset{F}{C}}-$	18

Parallel to C6 fluorinated polymers, silicone based surface finishes also have been developed and used in hydrophobic textile fabrics in the recent past. Textile fabrics treated with silicone resins having long alkyl chains demonstrate very high WCAs on their surface. Namely, hexadecyltrimethoxysilane (HDMTS)[37–39], octyltriethoxysilane (OTES)[40,41], trichloro(octadecyl)silane (OTS)[42], methacryl-heptaisobutyl polyhedral oligomeric silsesquioxane (MAPOSS)[43] and polymethylsilsesquioxane (PMSQ)[44–46] are more commonly blended with NPs to impart superhydrophobic properties to textile fabrics. Silicone based resins are mostly applied for oil/water separation as they don’t exhibit any oliophobicity. For instance, Li *et al.* have reported a robust superhydrophobic cotton/spandex fabric (99% cotton) filled with polyurethane (PU) sponge for ultrafast collection of oil from water. Cotton fabrics were treated with octadecyltrimethoxysilane (OTMS) and silica NPs to impart water repellent properties[47]. Similarly, Xue *et al.* prepared PET fabrics using –$Si(CH_3)_3$ functionalized silica NPs by sol-gel process using 1,1,1,3,3,3-hexamethyl disilazane as precursor[48]. The prepared PET fabrics demonstrated very stable superhydrophobicity (WCA 150°) against 1000 abrasion cycles and oil separation from oil/water mixtures. In another study, Xue *et al.* utilized polydimethylsiloxane (PDMS) coatings over hierarchical silica NPs layers. The prepared fabrics using PDMS/silica NPs demonstrated similar oil/water separation properties[49]. Only PDMS also have been utilized in water repellent fabrics without NPs[49,50]. Although, PDMS is inexpensive, transparent, non-toxic and biocompatible, the PDMS coated surfaces are likely to be deformed under prolonged contacts with water droplets and droplets spread on their surfaces with time, as recently described by Mishra *et al.*[51]. Conclusively, both C6 fluorinated and short alkyl chain silicone resins still have some functional limitations that require a proper investigation and effective fabrication techniques to prepare stable water repellent and water resistant fabrics like Gore-Tex. In this thesis (chapter 2), this issue have been addressed and a sequential bilayer treatment have been designed using C6 fluorinated chemistry and PDMS resin in combination.

1.2.2 Electrically conductive textiles

Conductive fabrics are successfully used for various applications in smart textiles, such as thermo-regulated wearables[52], static charge dissipation[53], electromagnetic interference (EMI) shielding[54], wireless signal transmission and power storage[55,56]. Particularly, signal and power transmitting fabrics in which integrated electronic components (resistors, sensors, capacitors, etc.) are interconnected, are regarded as the core features in smart textiles for medical, sports, fitness and military gear[57–59]. As these conductive textile interconnections are worn over the curvilinear human body, a number of attributes, such as light weight, flexibility, porosity (breathability), wear abrasion and mechanical strength are of extreme importance[57]. Fig. 1.5 summarizes some common conducive materials that are utilized for conductive textiles[59].

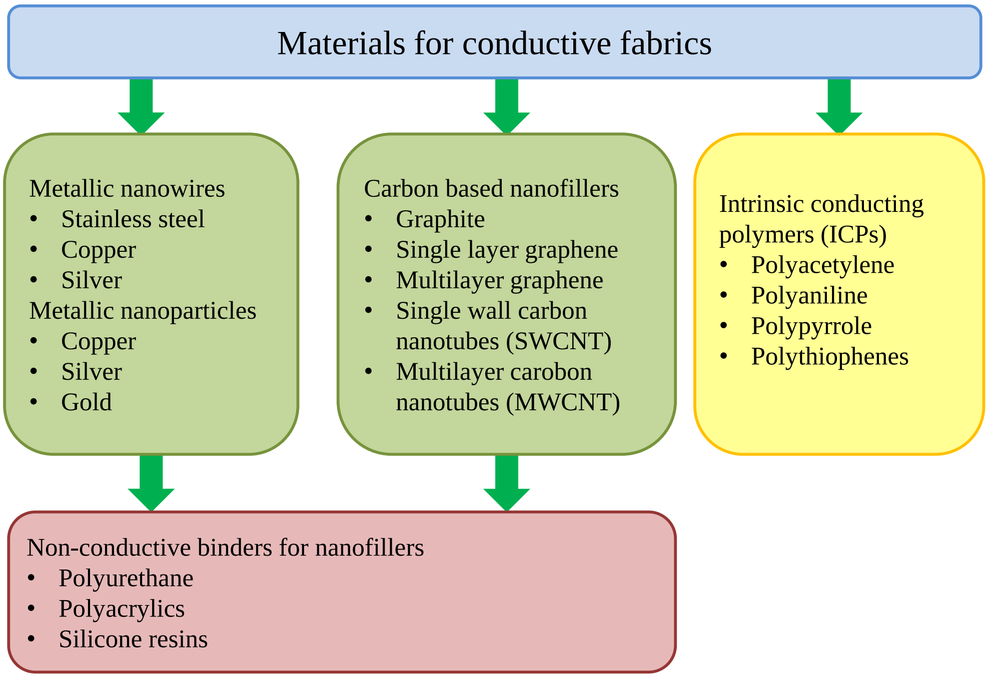

Fig. 1.5. List of common conductive nanofillers, binders and conjugated polymers for fabrication of electro-conductive textiles.

In the past, conductive textiles fabrics have been extensively implemented by incorporating metallic mirco/nano wires/particles into fabric structures during the manufacturing processes[55]. For this, there are three common techniques available for different processing stages (Fig. 1.6).

- At fibre manufacturing stage; metallic nanoparticles are mixed with polymer melts during melt spinning process and then extruded through spinneret, however, this technique is only applicable for synthetic fibres.
- At yarn manufacturing stage; conventional fibres (cotton, wool, silk, polyester, nylon) are spun together with metallic micro/nano-wires or foils during yarn manufacturing process and subsequently woven into fabrics by weaving process.
- At fabric manufacturing stage; in this approach, pure metallic yarns (stainless steel, silver, copper) are woven into fabric structures during weaving process according to the required design.

Conductive fabrics prepared by these abovementioned techniques demonstrate high conductivity, functional stability and durability, however, significant wear and tear of processing parts is disadvantageous. Moreover, the prepared conductive fabrics by mantellic wires were found to display significant stiffness levels and bulkiness[60,61].

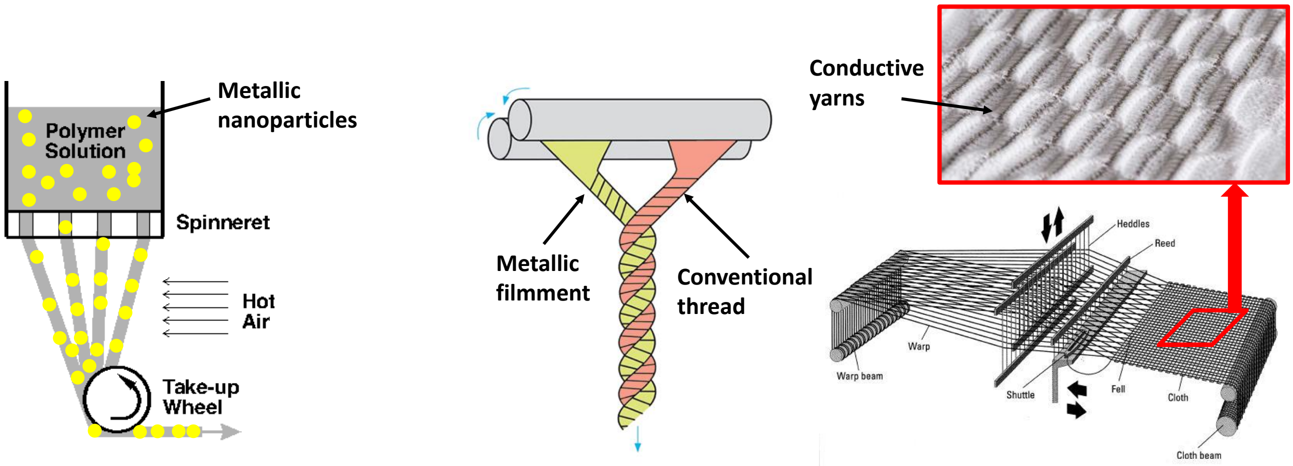

(a) (b) (c)

Fig. 1.6. Incorporation of metallic nanoparticles/wires during (a) fibre, (b) yarn and (c) fabrics manufacturing process for smart textiles (source: google images).

Alternatively, industrial scale metallization of textiles by vapour or electroless deposition (dipping in electrolytic salt solutions) has been vigorously investigated[62,63]. Electroless deposition is still popular , however, issues related to coating homogeneity, folding/bending or abrasion induced coating loss, oxidation and corrosion are still challenging[64]. Recently, carbon based materials, such as carbon nanotubes, nanofibers, graphene and colloidal graphite for conductive interconnections have also been implemented as suitable materials[56,59,64,65]. The main drawback associated with nanoscale carbon materials for conductive fabrics is their poor adhesion to fibre surfaces and hence the use of additional binders is required[66,67]. This causes a significant loss of fabric properties (breathability, flexibility), increase in final weight (> 50%)[66,68] and makes the finished products expensive as the binders are mostly electrically insulating polymers. Considering these design and cost impediments, there is still room to develop highly flexible, conformal and lightweight fabrics using facile alternative processes.

Since the first discovery of conductive polyacetylene in 1977 by noble laureates Hideki Shirakawa and his co-workers[69], the intrinsically conducting polymers (ICPs) have been developed and extensively investigated for electronic applications. Because of their excellent features, like, light weight, flexibility, conformal and film forming abilities, ICPs deserve special attention in conductive textiles as well[70]. A number of conjugated polymers and their derivatives have been successfully utilized to produce conductive textiles such as polyaniline[71,72], polypyrrole[52,62,73,74] and polythiophenes[75–80]. Their chemical structures are shown in Fig. 1.7. In particular, poly(3,4-ethyeledioxythiopene) (PEDOT) doped with poly(styrenesulfonate) (PSS) is quite attractive as it can be processed in aqueous solutions/inks, as well as in environmentally friendly solvents[81]. It also features highly conjugated back-bone, environmental stability, biocompatibility and conformal flexibility [81,82].

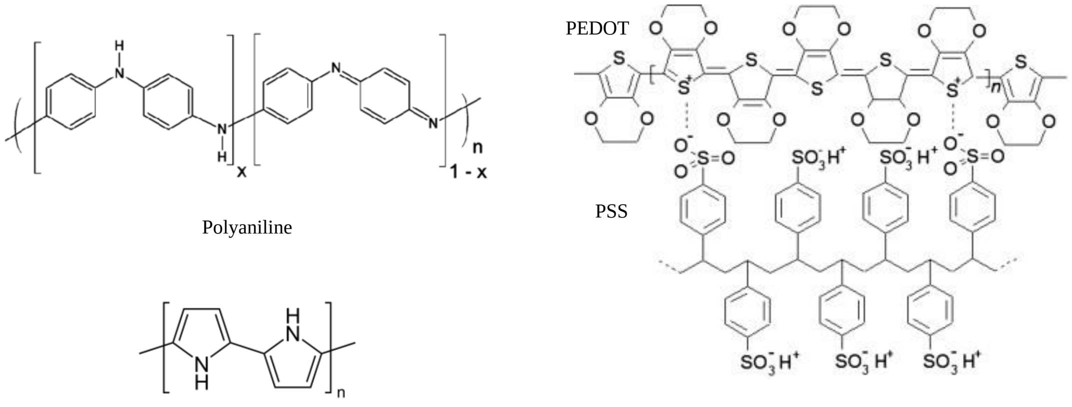

Polyaniline

Polypyrrole

Poly(3,4-ethylenedioxythiophene):poly(styrene sulfonate)
PEDOT:PSS

Fig. 1.7. Chemical structures of different ICPs.

PEDOT:PSS films have been used in several electronic applications in the past[83–86]. Meanwhile, PEDOT:PSS coatings for conductive textile fibres were also developed especially for synthetic fibres, such as, nylon[87], spandex[75], polyester (PET)[75,88,89] and their blends[75]. The PSS backbone attached to the PEDOT segments serves three different purposes at a time, i) stable dispersion, ii) charge balancing and iii) a template polymer. However, this PSS template polymer with excess of polysulfonic acid groups (see Fig. 1.7) renders the PEDOT:PSS solutions highly acidic[90,91] and cause pH levels to remain below 2. Synthetic fibers, like, polyester, nylon, aramid, when coated with PEDOT:PSS can easily withstand this extreme conditions. On the other hand, this is a severe drawback for cotton fabrics[76] as acid hydrolysis readily degrades cotton[92]. This aspect is rarely mentioned and most often overlooked in the literature, while it causes significant loss in mechanical resistance. For instance, Ding et. al. produced flexible electrochromic cotton fabrics using PEDOT:PSS treatment with electrical conductivity of 0.12 S/cm[75]. They did not discuss any mechanical properties of the fabrics before or after treatment. Mattana et. al. reported cotton fibres based organic transistors using PEDOT:tosylate (an analogous of PSS) and a primer coating of gold nanoparticles[93]. They reported that even though a resistance per unit length of 25 kΩ/cm was measured, a significant loss of Young’s modulus and elongation loss occurred in the fabrics. Very recently, Yeon et. al. stressed degradation of cotton fabric by PEDOT:PSS solutions and in prevention of this drawback, they substituted PSS with sodium dodecyl sulfate (SDS)[80]. They used a cotton-based fabric (98% cotton/2% polyurethane) for this study. The SDS modified conductive fabric demonstrated a sheet resistance of 24 Ω/sq. at 1.7 mg/cm2 mass loading and they were highly stretchable (strain-150%). Note that it is very challenging to produce electroconductive textiles having low surface resistance < 10 Ω/sq. without resorting to high levels of material/coating loadings (mg/cm^2), which significantly alters various fabric attributes, such as breathability, flexibility and washing induced wear**.** Although, these limitations can easily be overcome by a synergic effect of both ICPs and conductive nanofillers when mixed together, as in the works of Matana *et al.*[93], Hu *et al.*[94] and Tian *et al.*[95]. Here in chapter 3, a similar approach of mixing PEDOT:PSS with graphene fillers have been adopted. The detrimental effects of PEDOT:PSS on cotton fabrics have been successfully circumvented by neutralizing sulfonic acid groups.

1.2.3 Antibacterial and self-cleaning fabrics

Another very important application of nanotechnology in textiles is fabrication of antibacterial and self-cleaning textiles. Functionalization of fabrics to render them antibacterial and self-cleaning have gained more attention due to rise in health and safety awareness[96–99]. Moreover, microenvironment of the conventional fabrics (perspiration, deposited contaminants, dyes) possesses suitable conditions for bacterial growth and might potentially result in cross infection, transfer of diseases or odour on skin contact[100]. Therefore, it is crucial to apply functional finishes on conventional fabrics to prevent these health risks.

In the past, a large number of antibacterial fabrics have been produced using silver, copper and gold nanoparticles[100–102]. However, even though these nanoparticles have good antibacterial potential, they are very expensive, present high surface abrasion, instability in the environment and considered cytotoxic[103–105]. On the other hand, textile fabrics functionalized with photocatalytic titanium dioxide nanoparticles (TiO_2 NPs) eliminate these barriers and demonstrate non-toxic, biocompatible, inexpensive and highly stable textile finishes[103,106,107].

The photocatalytic mechanism of TiO_2 NPs has been well established and investigated for its extended applications. Briefly, when photons with energy ($h\nu 1$) equal to or greater than the band gap of TiO_2 (~3.3 eV for the anatase phase) are irradiated on their surface, an electron is promoted from valance band (VB) to conduction band (CB) leaving a hole with positive charge in the VB, as shown in Fig. 1.8. At this stage the induced electron-hole pairs have two possibilities, either recombine and dissipate the input energy as heat or get trapped in metastable surface states. In the later scenario, the photo induced electron-hole pairs can react with electron donors and electron acceptors adsorbed on the semiconductor surface. After reaction with absorbed moisture and oxygen on their surfaces, these electron-hole pairs can produce hydroxyl radicals ($OH^\bullet$) and superoxides (O_2^-), respectively, with high redox oxidizing potential[108–110]. Depending upon the exact conditions, the holes, OH$^\bullet$, O2$^-$, H_2O_2 and O_2 itself can play important roles in the photocatalytic reaction mechanism.

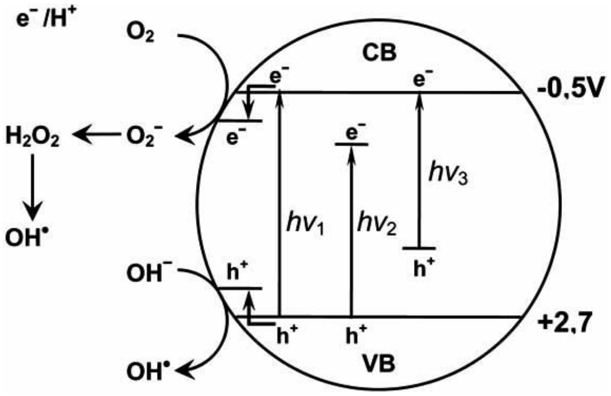

Fig. 1.8. Mechanism of TiO_2 photocatalysis: *hv*1: pure TiO_2; *hv*2: metal-doped TiO_2 and *hv*3: nonmetal-doped TiO_2[108].

Besides their photo-induced antibacterial nature, TiO_2 NPs also display photocatalytic degradation of several chemical compounds, such as, dyes (methylene blue, congo red)[111] and odorous gases (ammonia, mustard)[112,113] under ultraviolent (UV) irradiations. UV induced hydroxyl radicals (OH$^\cdot$) and superoxides (O2$^-$) on the surface of TiO_2 NPs degrade these chemical compounds[108]. The main drawback of TiO_2 NPs is that they only manifest photocatalytic activity under UV irradiations corresponding to their band gap (~3.2 eV)[8]. This issue has been addressed in the past and doped TiO_2 NPs with narrow band gap (ca. 2.75 keV) have been prepared using different metallic and non-metallic doping elements (Ag, Cu, Pt, C, N)[108,114]. The visible light photoactivity of metal-doped and nonmetal-doped TiO_2 is attributed to new energy levels produced in the band gap of TiO_2 by dispersion of doping elements in the TiO_2 matrix. Consequently, electron can be excited from the defect state to the TiO_2 conduction band by photon with energy equals *hv*2 and *hv*3 (see Fig. 1.8) for metal doped and nonmetal-doped TiO_2 NPs, respectively[115]. Particularly, TiO_2 NPs doped with transition metals exhibit improved trapping of electrons and reduce electron-hole recombination rate that results in enhanced photocatalytic activity under visible irradiations[108].

Therefore, doped TiO_2 NPs exhibit similar antibacterial and self-cleaning properties under visible irradiations as that of undoped states under UV. Textile fabrics deposited with doped TiO_2 NPs have good potential for stain proofing and antibacterial fabrics as well as for water and air purification applications, as shown in Fig. 1.9. Additionally, unlike NPs suspensions, textile fabrics deposited with doped TiO_2 NPs can also be recycled several times without any post treatment filtration[116,117].

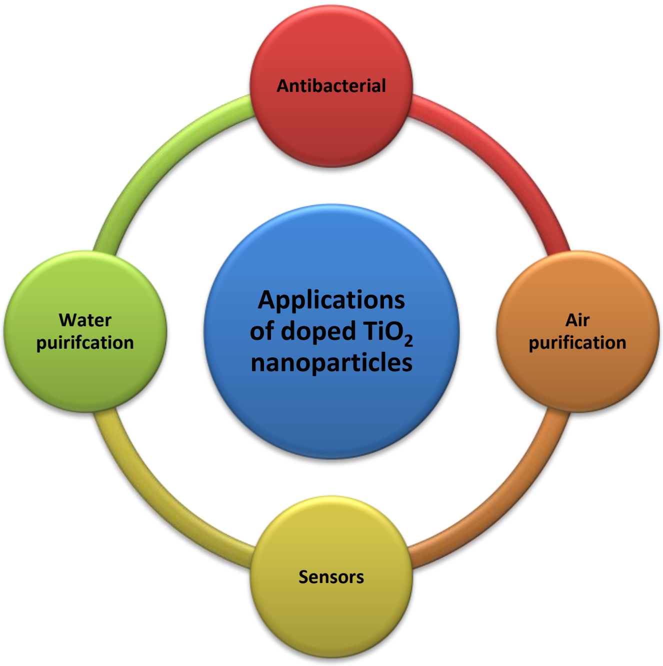

Fig. 1.9. Photocatalytic applications of doped TiO_2 nanoparticles

In the past decade, doped TiO_2 NPs have garnered much attention of the researchers for functional textiles. For instance, Gaminian *et al.* have prepared a polyester fabric with Cu_2O doped TiO_2 NPs for degradation of Methylene Blue (MB) dye under visible light[118]. The authors have investigated the role of different *in-situ* synthesis parameters (concentration, pH) on self-cleaning properties of the prepared fabrics. Rana *et al.* developed a cotton fabric with Ag/AgBr doped TiO_2 NPs using a simple spray coating technique[119]. The prepared cotton fabrics demonstrated good UV blocking, hydrophobic, oil-water separating and antibacterial properties. The authors have also reported a 18% improvement in mechanical strength of the treated fabrics. Recently, Khani *et al.* deposited copper doped TiO_2 NPs onto cotton fabric nanocomposite for wound care applications[120]. The prepared wound dressing demonstrated an enhanced cell viability and good resistance against gram positive and gram negative bacterium. As seen above, although it is a well-established area of the research and different doped TiO_2 NPs have been efficiently incorporated to textile structures[97,118,121,122], there is still room for improvements using inexpensive and highly photoactive doped TiO_2 NPs for textile fabrics. This functional aspect also have been studied in this thesis (chapter 4). For this purpose, multifunction cotton fabrics have been developed using Mn-doped TiO_2 NPs and exhibit antibacterial and self-cleaning properties.

1.3 Scope of this study

The message extracted from the literature review, potential applications, implemented materials, and fabrications techniques, it is quite obvious that there is still room for improvements in these research areas. For instance, use of sustainable/eco-friendly textile finishes, minimal amounts of volatile solvents, cost efficient processes, retained fabrics inherent properties, easy and scalable fabrication techniques can be easily adopted to functionalize textile fabrics for high value applications. The chemical modification of cotton textiles with non-toxic materials could adjust properties of the finial fabrics for different purposes and meet the environmental legislation requirements.

The aim of the present study was to create new pathways towards the production of highly-engineered textiles from environmental friendly materials. The research strategy in this study covered the following points:

- To synthesize and characterize cotton based functional textiles (chapter 2-4)
- To carry out the modification of cotton fabrics through sustainable approaches (chapter 2-4).
- To preserve inherited characteristics of the native textiles after functionalization (chapter 2-4).
- To investigate potential applications of the prepared materials (chapter 2-4).
- To develop a simple and scalable recycling process for waste fabrics (chapter 5).

Chapter: 2

Fabrication of hydrophobic cotton fabrics by sustainable materials

2.1 Introduction

Textiles are intensively used materials in daily life. However, direct outdoor use of textiles including the synthetic ones such as nylon, polyester, acrylic etc. for weather protection and water proofing require surface treatment or multilayer approaches[123,124]. Textiles made from natural fibers such as cotton, wool, silk etc. are particularly unsuitable for weathering owing to their inherent hydrophilicity and structural instability upon contact with water[125]. Nevertheless, recently increased environmental awareness as well as potential large scale applicability of some techniques towards water proofing natural fibers have increased exploitation of these inexpensive natural fibers for applications with requirements of water and oil repellency[126,127]. Modifying fiber surfaces by changing their roughness and chemistry is considered to be the only way to achieve water repellent natural fibers [46,128]. This is still a challenging task and requires an efficient combination of low surface energy chemistry with hierarchical micro/nano-scaled roughness[129]. The most common approaches reported in the literature involve utilization of fluorine or silicone chemistry with nanoparticle (i.e. SiO_2, ZnO, TiO_2) immobilization on fiber surfaces[130–133]. In order to achieve water repellent textiles, various fabrication techniques such as solution immersion[17,47], plasma modification[134], layer by layer assembly[135], chemical vapor deposition[46] and sol-gel methods[136] have been implemented. Some of these non-wettable textiles have been successfully demonstrated in applications like filtration, oil-water separation and patternable wetting[10,137,138].

2.2 Objectives

The main objectives of this study is to prepare sustainable superhydrophobic cotton fabrics with WCAs ~150°, high droplet mobility on the surface and good resistance to water transportation across the fabric. Secondly, minimal use of fluorinated chemicals and volatile organic compounds (VOCs) is also considered as per aforementioned environmental regulations. The prepared superhydrophobic cotton fabrics are characterized for their morphology, chemical interactions, mechanical strength and resistance to wear abrasion and ultrasonic washing.

2.3 Materials and methods

2.3.1 Materials

Plain woven and bleached 100% cotton fabric (named as fabric-A) with 135 ± 5 g/m^2 mass density and having 56/cm warp and 40/cm weft threads was purchased from a local market. Another fabric (fabric-B) was supplied by Cotonificio Albini (Italy) having 83/cm warp threads, 36/cm weft threads and 120 ± 5 g/m^2 mass density. All the characterization results reported herein are based on fabric-A, however, identical results were measured with fabric-B. Fabric-B displayed higher hydrostatic head compared to fabric-A due to its higher warp density (83/cm). Fabrics were prewashed with a normal laundry cycle to remove possible contamination before use. Fluorinated acrylic copolymer (Capstone ST-100 with C-6 chemistry) 20% (w/v) aqueous latex dispersion was purchased from Garzanti Specialities S.p.A (Italy) and an acetoxy cure single component polydimethylsiloxane (PDMS, Elastosil E43)[139] was purchased from Wacker Chemie AG (Germany). As per the manufacturer, the silicone resin has 600% maximum elongation upon cure. Its inherent viscosity is 3×10^5 mPa.s. Reagent grade solvents heptane and methanol (Sigma Aldrich) were used as received. Fumed silica nanoparticles (Aerosil, R812), with an average particle size distribution between 7 nm and 40 nm, were purchased from Evonik industries (Germany) and used as received. Milli-Q distilled water was used for all hydrophobic characterization techniques.

2.3.2 Sample preparation

Prewashed and ironed cotton fabrics (10×10 cm^2 sample size) were first treated with fluorinated acrylic copolymer solution by diluting the as-received water-based solution (Capstone ST-100) down to 1% by weight using methanol. For treatments containing silica nanoparticles, various amounts of SiO_2 nanoparticles were added into the diluted polymer solution so that nanocomposite coatings with 100/0, 90/10, 80/20, 70/30, 60/40, 50/50 polymer/nanoparticle weight ratios on dry basis were obtained. The solutions were tip sonicated for 15 seconds with 20 kHz, 750W and amplitude at 40% (vibra cell™ XCV-750, Sonics and Materials Inc. USA). Note that the polymer/nanoparticle solutions were very stable with no agglomeration or precipitation as long as the nanoparticle concentrations (with respect to polymer weight) did not exceed 30%. Then, the fabrics were soaked in the solutions for 30 minutes for complete impregnation. Treated fabrics were dried by a hot air gun for 10 seconds and afterwards cured in oven at 120°C for 1 hour.

The final silicone polymer layer was applied as follows: As received acetoxy-cure PDMS silicone resin was diluted by heptane such that solutions with 10%, 15%, 20%, and 25% polymer by weight were obtained. Pretreated cotton fabrics were coated with these silicone solutions using an EC-200 rod coater (Chem Instruments Inc., USA) with a linear coating speed of 28 cm/min. As a result of several experimental coating trials with different PDMS concentrations, the best treatment concentration was found to be 15 wt %. This was based on the final feel, softness and the thickness of the fabric. Coated fabrics were allowed to crosslink at room temperature for 24 hours at 65% humidity. As control (reference) samples, only fluoropolymer/SiNPs (CF) and only PDMS (CS) single layer coated cotton fabrics were also made. Table 2.1 shows the identification details of different samples used in this work. Herein, the SiXX coding attributes to the percentage of silica nanoparticle on dry bases against fluorinated polymer, followed by a PDMS encasing. For instance, samples Si0 and Si30 corresponds to 0 wt.% and 30 wt.% silica nanoparticles in the coating formulations, respectively. Dry weight pick-up signifies the percent additional weight gained by the textile due to the polymer treatment.

Table 2.1. Identification of the prepared hydrophobic cotton fabrics.

Sample ID	**1st Layer (pre-treatment)**		**2nd Layer**	**Dry weight pick-up**
	% Capstone	**% SiO_2 NPs**	**% PDMS**	**%**
CS*	0	0	100	10
CF*	70	30	0	1
Si0	100	0	100	11
Si10	90	10	100	11
Si20	80	20	100	11
Si30	70	30	100	11
Si40	60	40	100	11
Si50	50	50	100	11

CS* indicates single layer control sample with silicone based PDMS coating

CF* indicates single layer control sample with fluorinated polymer and silica NPs (70/30)

2.3.3 Characterization

2.3.3.1 Morphological characterization

For analyzing morphological modification of treated textiles, Scanning Electron Microscopy (SEM) and Atomic Force Microscopy (AFM) were used. The SEM was a JEOL-6490AL (Japan) working in high vacuum mode. Prior to imaging a thin film of gold (10 nm) was deposited on sample surfaces by ion sputtering (Cressington 208HR sputter coater, UK). SEM images were captured at different magnifications and accelerating voltages such as 10 kV and 15 kV. Fabric pore sizes were also measured by a software tool connected to the SEM image analyzer during acquisition of images. Where necessary, high-resolution SEM imaging was carried out using a JEOL JSM 7500FA (Japan) equipped with a cold field emission gun (FEG), operating at 5 kV acceleration voltage and using backscattered electrons to see differences in chemical composition. The samples were carbon coated with a 15 nm thick film using an Emitech K950X high vacuum turbo system (Quorum Technologies Ltd, East Sussex - UK).

For AFM measurements, a Park system (XE-100) in non-contact tapping mode was used mounted on an anti-vibration table (Table Stable TS-150). The AFM was enclosed by an acoustic chamber. Single-beam cantilevers tips (PPP-NCHR-10M) were used for the data acquisition with less than 10 nm nominal radius and 42 N/m elastic force constant for high sensitivity. The scan rate was 0.1 Hz and zoom areas of 2×2 μm^2 were scanned at resonance frequency of around 350 KHz. Acquired images were further processed with WS×M 5.1 processing software [140]. The roughness characteristics of the surfaces were determined by using a built-in grain analysis statistical algorithm. The process involves the watershed algorithm that is usually employed for local minima/maxima determination and image segmentation in image processing. AFM topography images are segmented into many zones identified with a certain average roughness. The mean roughness of the image is calculated by averaging the roughness values obtained from four different areas[141].

2.3.3.2 Attenuated Total Reflection-Fourier Transform Infrared (ATR-FTIR) Spectroscopy

Infrared spectra of samples were obtained with an ATR accessory (MIRacle ATR, PIKE Technologies) coupled to FTIR spectrometer (Equinox 70 FT-IR, Bruker). All spectra were recorded in the range from 3800 to 600 cm^{-1} with 4 cm^{-1} resolution, accumulating 128 scans. To ensure the reproducibility of obtained spectra three samples of each type were measured. ATR mode was preferred since it allows the chemical analysis of the surface, enabling a better characterization of the different coatings employed. In our ATR-FTIR spectrometer the calculated penetration depth of ATR into the sample varies between ~0.55 µm at 3800 cm^{-1} and ~3.30 µm at 600 cm^{-1}.

2.3.3.3 Wetting and water contact angles

Static water contact angle (WCA) and water shedding angle (WSA) or droplet roll-off angle were measured with a contact angle instrument (OCAH-200 DataPhysics, Germany). Gastight 500 µL Hamilton precision syringe with blunt needle of 0.52 mm internal diameter was used for droplet dispersion. The WCA of a 5 µL droplet volume was measured after 30 s of droplet deposition. From each sample a strip of 1×5 cm^2 was cut and attached to contact angle table with double sided adhesive tape to get a wrinkle free surface for WCA measurements. Static WCAs at 10 different positions on each sample were measured and reported as mean values with standard deviations.

For WSA measurements, different droplet volumes corresponding to 5.0, 7.5, 10.0, 12.5, 15.0, 20.0, 25.0 µL were deposited and the substrate holder was tilted with an angular speed of 1.02°/sec. Three measurements of each volume at different points were reported as average values with the corresponding standard deviations. A common test proposed by Zimmermann *et.al.* [142] that is generally used by textile industry was also conducted. This test takes into account measurements of droplet roll-off angles when drops are allowed to impinge from 1 cm height. As such, 5 droplets of 8.0 µL were dropped from 1 cm height at the same spot on the treated fabrics and they were allowed to roll over a 5 cm length when the substrate was tilted at different angles between 10° and 30°. The treated textiles were labeled as sticky if at any one of the tilt angles one or more of the droplets do not completely clear the 5cm length by rolling away. A treatment resulting in such a sticky state based on the Zimmermann method is not considered a proper hydrophobic textile.

2.3.3.4 Hydrostatic head

Waterproof properties (resistance to water penetration) of the treated fabrics were quantified by measuring hydrostatic head pressures due to water column rise over the fabrics. A glass column (1 m long with 80 mm internal diameter) was purchased from TecnoVetro, Italy. It could be filled with 5 L of water and at the bottom it was connected to a glass reservoir with a flange, as shown in Fig. 2.1. Vertical column was graduated and at the bottom was fitted with a flange sealed with rubber and Teflon gaskets having six bolted clamps in order to fix a fabric sample with 10×10 cm^2 dimension. The glass column was fed by a plastic tube with continuous supply of distilled water from a storage vessel. Leakage threshold of the fabric was recorded in terms of column height (cm) when droplet(s) formed on the opposite surface of the fabrics. Five samples of each treatment were tested and average column heights with standard deviations were recorded.

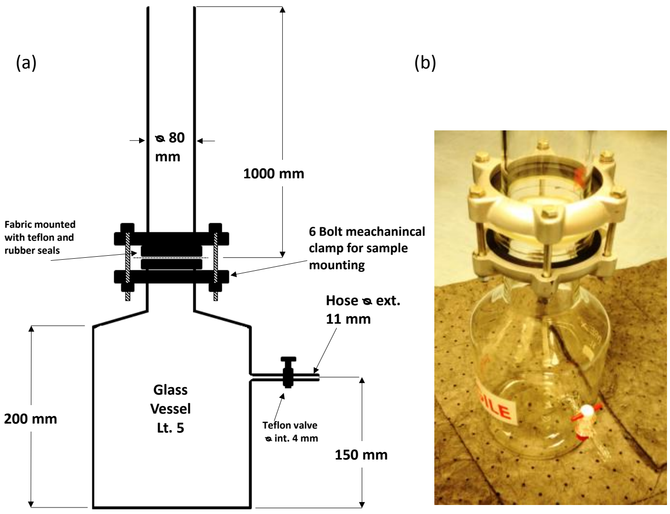

Fig. 2.1. Hydrostatic head glass column with 1 m height and 80 mm internal diameter. (a) schematic design and (b) real image of hydrostatic head column.

2.3.3.5 Mercury Intrusion Porosimetry

A non-wetting liquid technique was used to calculate fabric porosity and average pore sizes. Measurements were made by Mercury Intrusion Porosimeter (Pascal 140 and 240, Thermo Quest/Finnigan Intruments, USA). Fabric samples of 0.03 to 0.20 g weights were cut into strips and rolled up to form a cylinder of 1 cm diameter and inserted in the dilatometer for porosity measurements. External pressure range from 0.006 MPa to 300 MPa was used for mercury intrusion. The maximum effective pressure for mercury intrusion relative to fabric pore sizes were recorded by instrument to auto-calculate fabric porosity in percentage and average pore radii in µm.

2.3.3.6 Wear Abrasion Tests

Linear abrasion experiments were conducted with a Taber Linear Abraser 5750 (USA). The applied weight was 0.35 kg with stroke length of ~ 5 cm and stroke speed of 15 cycles/min. The abradant used was Calibrase Disk (CS-10F) with a base diameter of approximately 1.5 cm. It is a resilient disk composed of a binder and aluminum oxide abrasive particles that offers a mild abrading action, designed to operate under loads of 0.25 to 0.5 kg, corresponding to roughly 13 kPa to 29 kPa abrasion pressures, respectively. The CS-10F abradant is typically used to test safety glazing materials and transparent plastics against abrasion induced transparency losses. In this work, the corresponding abrasion pressure is 17.5 kPa under 0.35 kg of applied weight.

2.3.3.7 Tensile strength

For mechanical characterization (stress-strain curves), an Instron (3365 Instron, USA) instrument was used. Five specimens from each material were measured. A dog bone shaped sample of 25 mm length along the axis of warp threads and 3.98 mm width was cut by a mechanical cutter. Samples were mounted in pneumatic clamps and a constant rate of extension 5 mm/min was used for each measurement at room conditions. Young's modulus (MPa) and elongation percentage at maximum load were also reported as an average of 5 measurements with standard deviations.

2.4 Results and discussion

2.4.1 Microscopic Morphology

Fig. 2.2 shows the SEM images of untreated (prewashed) fabric, control sample CF coated with the fluoropolymer/nanoparticle composite, and samples Si0 and Si30 (see Table 1). As seen in Fig. 2.2a, the untreated fabric is composed of a network of round cellulosic (cotton) fibers with some uneven microfibrilar structure (due to abrasion during manufacturing). On the other hand, in the Si0 sample (Fig. 2.2b), the cotton fibers' surfaces are coated with the fluorinated copolymer and PDMS, respectively, without silica NPs. The treated surface of sample Si0 appears to be more evenly coated with PDMS resin as out layer. On the other hand, the nanocomposite treated control sample CF shows rough hydrophobic textures on the fibres' surfaces as seen in Fig. 2.2c. Regarding sample Si30 the thickness of the final hydrophobic polymer layer (acetoxy-PDMS), that is intended to increase the hydrophobic resilience and robustness of the fibres, should neither smooth out the roughness nor close the pores of the fabrics. In other words, the thickness should be adjusted such that it will be somewhat conformal to the underlying texture in order to combine hydrophobic silicone chemistry with the texture formed by the pretreatment. As seen in Fig. 2.2d, after the acetoxy-PDMS final layer is applied, the cured silicone layer does not totally flatten out the roughness but a much finer roughness scale is still maintained on the fibre surfaces (see inset Fig. 2.2d). As will be shown later, this structure is sufficient to maintain droplet mobility on the textile surface, in other words, droplets can roll off. Note that the sequential treatment does not alter the porosity of the fabrics guaranteeing the breathability of the fabrics.

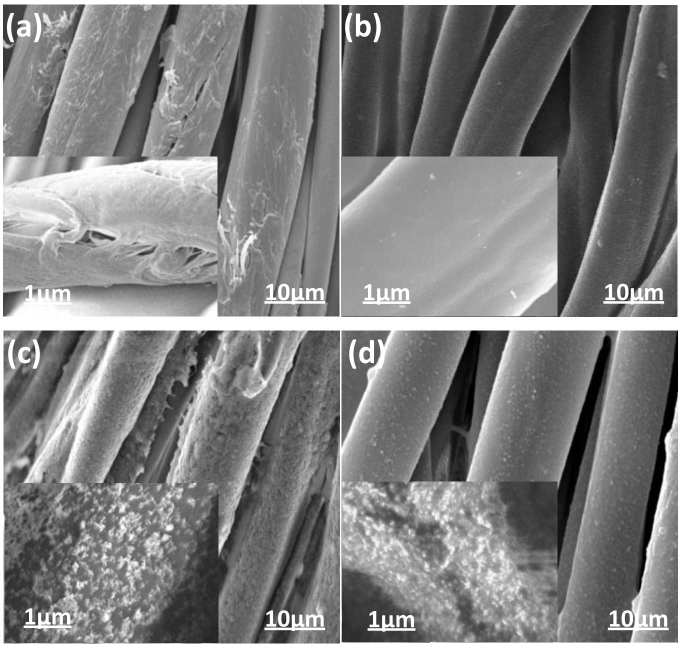

Fig. 2.2. SEM images of fabric A. (a) Untreated fabric. (b) Sample Si0. (c) Control sample CF. (d) Sample Si30. Complete coverage of each individual treated fiber is visible without forming a continuous film. Insets show high resolution SEM images.

Cotton fiber surface morphology of the untreated and treated fabrics was further studied by AFM measurements as shown in Fig. 2.3. AFM measurements were conducted on three different samples, untreated fabric, control CF and Si30 samples. Topography of the untreated fibers (Fig. 2.3a) demonstrates typical wrinkle-like structures[20]. The calculated average roughness of untreated fiber surface was 120 ± 21 nm. Typical AFM surface morphology of nanocomposite treated fibers is seen in Fig. 2.3b corresponding to control sample CF. The texture is due to the assembly of the SiO_2 nanoparticles over the fiber surface. The calculated average roughness of the control sample CF was 52 ± 13 nm. Typical AFM topography of subsequently PDMS coated fabric sample Si30 is shown in Fig. 2.3d. The calculated average roughness of sample Si30 was 10 ± 2 nm.

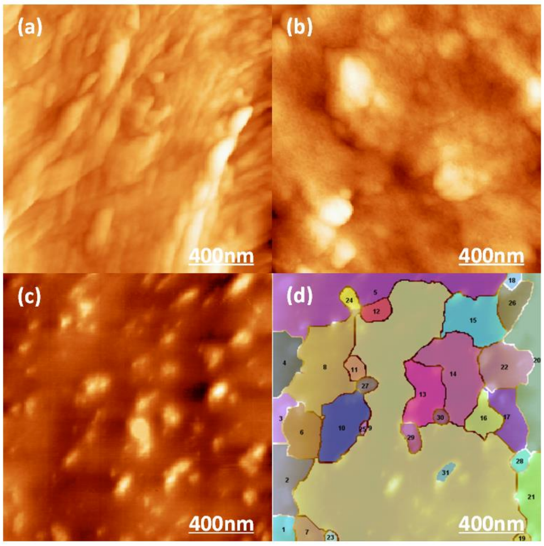

Fig. 2.3. AFM topology images. (a) Untreated cotton fiber having natural textured surface, (b) pretreated cotton fiber with fluorinated copolymer/SiO_2 nanoparticles (control sample CF), (c) silicone polymer (PDMS) finished sample Si30, (d) Roughness segments of sample Si30 generated by watershed grain analysis algorithm. Each segment indicates an individual roughness area and height (roughness volume).

Surface roughness of each sample was calculated by the Watershed grain analysis algorithm[141] an example of which is shown in Fig. 2.3d for sample Si30, with different roughness areas marked as segments with different colors. Each zone is identified with a single roughness parameter. In summary, it was found that the roughness of the original fibers' surfaces was reduced after each treatment step. As a result, the final fabric surface (referring to sample Si30) was on average much smoother than its untreated state. Although the top PDMS coat (unfilled self-levelling polymer solution) smoothed out the roughness features due to the primer coat (corresponding to control fabric CF), the resultant nanoscale individual fibre surface roughness combined with the hydrophobic chemistry of the cross-linked acetoxy silicone and the inherent micro-scale texture of the woven fabric network are sufficient to render the cotton fabric water repellent [143].

2.4.2 Chemical analysis

The chemical characterization of the different treatments was performed by ATR-FTIR spectroscopy, as shown in Fig. 2.4a. IR spectrum of pristine cotton fabric show well-known bands associated with pure cellulose namely, OH stretching at 3364 cm^{-1}, CH stretching at 2891 cm^{-1}, adsorbed water at 1645 cm^{-1}, ring breathing at 1157 cm^{-1} and C-O stretching at 1026 cm^{-1}[144]. For the fibres coated with the perfluoroacrylic copolymer (control sample CF), new peaks appear such as C=O stretching at 1732 cm^{-1} and asymmetric CF_2 stretching at 1236 cm^{-1}[145]. The FTIR contribution of the Si nanoparticles is also present as a shoulder at 1076 cm^{-1} assigned to the Si-O stretching in amorphous silica (Fig. 2.4a)[146]. No chemical interactions are present between the fluoropolymer and the nanoparticles. Finally, after acetoxy-silicone coating, distinct IR peaks associated with PDMS polymer are detected at 2964 cm^{-1}, 1261 cm^{-1} and 799 cm^{-1} for stretching, bending and rocking modes of CH_3 groups, respectively[139]. Stretching bands attributed to carboxyl (C=O) and CF_2 of capstone treatment are also present in the IR spectrum with less intensity due to depth profiling measurements. The extended shoulder associated with silica NPs can also be located in the PDMS finished fabrics (sample Si30).

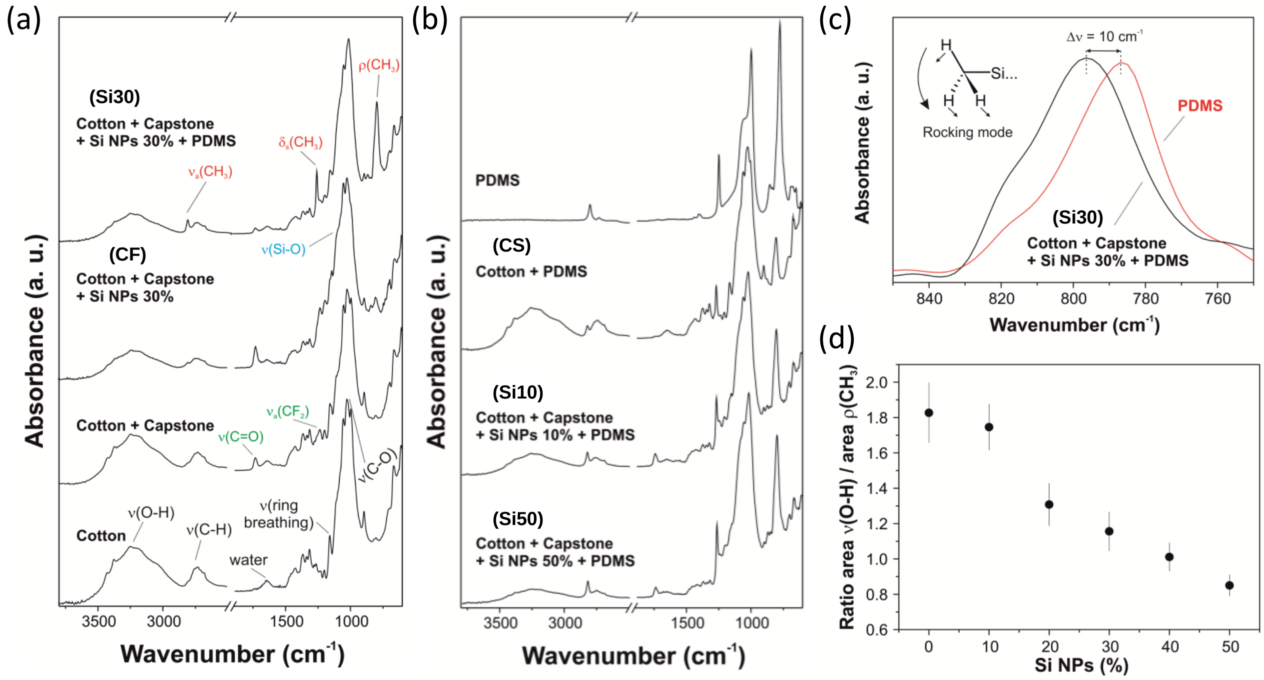

Fig. 2.4. Chemical characterization. (a) ATR-FTIR spectra of cotton substrates with different kinds of coatings. Assignments for cellulose (black), capstone fluoropolymer (green), Si nanoparticles (blue) and PDMS (red) are included. (b) FTIR spectra of pure PDMS film, PDMS coated cotton substrates (CS) and FTIR spectra with different weight ratios of silica nanoparticles (10% and 50% for samples Si10 and Si50, respectively). (c) CH_3 rocking absorption of pure PDMS film and PDMS finished cotton fabric with fluorinated polymer and silica NPs (sample Si30). The rocking mode of PDMS methyl groups is shown. (c) Variation of the ratio of areas of the cotton O-H stretching and PDMS CH_3 rocking modes with the content of Si nanoparticles.

In the case of the fabric sample Si30, during application and curing of PDMS on the fluoropolymer/NPs coated nanocomposite fabric, PDMS can directly interact with the cotton fibers' surfaces where certain pinholes or small uncoated zones are present. To study the interaction of PDMS with the fibers, we also performed FTIR on only acetoxy-PDMS treated cotton fiber (control sample CS) surface (see Fig. 2.4b). After curing directly on cotton fibres, several vibrations ascribed to PDMS were detected easily such as CH_3 rocking at 799 cm^{-1}[139]. The CH_3 rocking mode shifted by 12 cm^{-1} to higher wavenumbers compared to those of a pure PDMS film (data not shown here). A comparable shift of 10 cm^{-1} was also recorded when acetoxy-PDMS was cured on the cotton fabric pre-functionalized with the fluorinated polymer/Si NPs nanocomposite (Fig. 2.4c). This indicates a chemical interaction between PDMS and cellulose similar to the interaction between acetoxy-PDMS and starch system[139]. This interaction is the consequence of change in the distance of Si-O bonds due to the formation of H-bonds between OH groups of the polysaccharide and the ether group of PDMS[139]. Hence, we propose an analogous molecular scenario where the hydroxyl groups of cotton can interact with the oxygen atoms of the silicone.

Finally, as shown in Fig. 2.4d, for fabrics treated with silicone on the top of the nanocomposite treatment, there exists a linear decreasing trend in the ratio obtained by dividing signal area (under the curve) of the O-H stretching peak at 3364 cm^{-1} of cotton by the area of the CH_3 rocking signal at 799 cm^{-1} of PDMS as a function of increased silica nanoparticle concentration from 10% to 50% (see Fig. 2.4b). Note that the silica nanoparticles are part of the C-6 fluoropolymer nanocomposite. The decrease in this ratio can directly be correlated to the increase in hydrophobicity of the treatments and also allows optimizing the required nanoparticle concentration for droplet mobility.

2.4.3 Surface wettability

Cellulosic materials are well known for their super-wettability. Hence, untreated natural cotton fibers can take up water many times of their own dry weight[136]. This extreme wettability comes from high surface area of cotton fibers which are made up of hydrophilic cellulosic polymer[136,147]. Therefore, it was not possible to measure WCA on pristine cotton fabric. However, as Fig. 2.5a displays, once the various treatments were applied to cotton fabrics, they were able to maintain hydrophobic states and water droplets never penetrated into the fabric texture but rather evaporated in time (see inset in Fig. 2.5a).

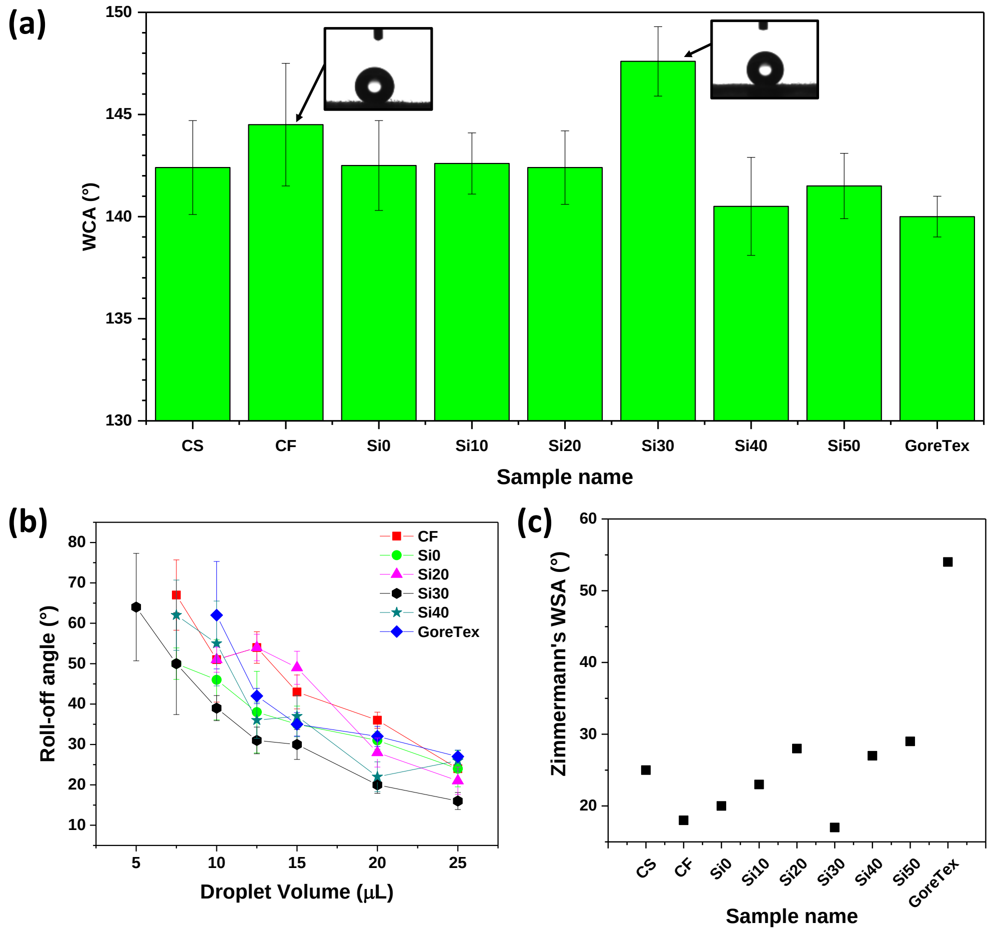

Fig. 2.5. Wetting characterization. (a) Static water contact angles of treated samples. Inset shows water droplets on control samples CF and sample Si30. (b) Water roll-off angles with increasing droplet volumes on selected treated samples. (c) Water shedding angles of all treated fabrics measured by Zimmermann's method (Zimmermann's WSA) with constant droplet volume of 8 μL.

Static water contact angles (WCAs) of all the samples studied are reported in Fig. 2.5a. Highest WCAs were measured on fabric samples CF and Si30 (~ 147°). Samples Si40 and Si50 (both having the PDMS outer layer) demonstrate somewhat lower WCAs compared to all the other samples. The treatment corresponding to sample Si30 was found to be the optimum in terms of hydrophobicity with WCA 147° ± 2°. Although static contact angles are similar between control fabric CF and Si30, the multilayer treatment had better hydrophobic performance compared to single layer control CF, which displayed a sticky hydrophobicity with small water droplets, as shown in Fig. 2.5b. Similarly, single layer PDMS treated control sample CS was sticky to small water droplets while larger volume water drops (200 μL) sank into its texture after some minutes of contact (see appendix-I, Fig. S1). Single layer PDMS-silica nanocomposites treatment also produced similar problems against contact with large water droplets (see appendix-I Fig. S1). Such hydrophobicity performance indicators (i.e., wetting by larger volume water droplets >10 µL) are not common in the literature[148], but are important for the real performance. Based on these observations, the bilayer method (polymer nanocomposite as the base layer and silicone as the outer) was used to ensure that the fabrics are not wet when in contact with larger water droplets rather than small static droplets. Note that the sequential treatment corresponding to C-6 fluoropolymer base layer without silica nanoparticles and the PDMS outer layer (sample Si0) produced very similar contact angles 142° ± 2° to samples CS, Si10 and Si20. Incorporation of silica nanoparticles in the first layer treatment at weight ratios of 10 wt.% (Si10) and 20 wt.% (Si20) was unable to elevate WCAs above 142°, as shown in Fig. 2.5a. At 30 wt. % silica nanoparticle loading with successive PDMS outer layer, the hydrophobicity of the fabric sample Si30 approached near to the superhydrophobicity limit of ~ 150°[149]. Additional loading of nanoparticles (>30 wt.%) was counterproductive and measured WCAs declined to lower than 140° as demonstrated by the samples Si40 and Si50. For the second outer layer, application of more concentrated PDMS solutions such as 20 wt. % and 25 wt. % in heptane did not increase hydrophobicity towards the superhydrophobicity threshold of 150°. This was attributed to the fact that under such concentrations, surface asperities generated by the underlying nanocomposite coating (detrimental for the Cassie-Baxter's non-wetting heterogeneous regime) were smoothed out[150]. Note also that lower PDMS solution concentrations such as 10 wt. % in heptane were found to be improper for the rod coating apparatus used in this study. It is important to note that static WCA of the commercial fabric GoreTex (140°) also remained lower than superhydrophobicity threshold.

As reported many times in the literature, determination of droplet baseline for static WCA measurements on textile surfaces is not as straightforward as in flat films. Short protruding fibers from the fabric surface causes hindrance to detect real baseline (contact line) which could lead to underestimation of the WCA[20,46,131]. Also in this work, it appears that all samples produced WCA measurements (Fig. 2.5a) that are in the range of 140° to 147°. In order to establish the hydrophobicity of the treated fabrics in a more reliable way water shedding angle (WSA or roll off angle) are also reported in Fig. 2.5b. It demonstrates water droplet roll off angles for treated fabrics like control sample CF, Si0, Si20, Si30, Si40 and GoreTex fabric. Shortly, samples CF, Si0, Si20 and Si40 were unable to repel small droplets of 5.0 to 7.5 µL, as shown in Fig. 2.5b. On the other hand, sample Si30 produced complete droplet shedding (tilt angles below 90^{o}) even for the lowest droplet volume used (5 µL), whereas, 5 µL and 7.5 µL droplets were sticky on the commercially available GoreTex fabric regardless of the tilt angle (≥90^{o}). Under such a condition, water droplets can partially wet asperities responsible for containing stable air pockets (trapped within the asperities) giving rise to sticky or stick-slip surfaces. It is clear from Fig. 2.5b that sample Si30 with 30 wt.% of silica NPs in its formulation demonstrates the lowest water roll off angles for all droplet volumes used. As for any water repellent surface, tilt angle for droplet roll off (shedding angle) decreases as the droplet size increases. Most reported hydrophobic textiles demonstrate low droplet roll off angles (≤ 10°) when large droplet volumes of more than 40 μL are used. For instance, Xue *et al.* characterized hydrophobic cotton fabrics by WSA using 50 μL droplet volumes to achieve 3° roll-off angle[20]. Hu *et al.,* used water droplets of 40 μL on hydrophobic cotton fabric surfaces to achieve droplet roll off at 29° tilt angles[151].

Another dynamic wetting test recommended by Zimmermann *et. al.* was also conducted to validate hydrophobicity of the treated fabrics[46,142]. In this approach, impinging water droplet roll-off characteristics are recorded in terms of tilt angles (Fig. 2.5c). It was found that both samples Si30 and control sample CF were repellent against impinging water droplets with 17°and 19° tilt angles, respectively. Note that droplets of 8 μL were used here, since impinging 5 μL droplets could not be created with the present experimental/syringe setup. Hence, the treatment corresponding to sample Si30 was the best in terms of static and dynamic wetting by small drops as well as resisted wetting by larger sized heavier water droplets. Moreover, in terms of both WCA and WSA angles, fabric Si30 displayed higher hydrophobicity than a commercial waterproof, breathable fabric membrane known as Gore-Tex[27] (see Fig. 2.5).

2.4.4 Resistance to water penetration

For theoretical estimation of Laplace pressure needed for penetration of water droplets into waterproof porous structure, effective pore sizes of samples CF and Si30 were acquired by a software analyzer tool connected to the SEM. In order to understand the effect of the porosity of the woven substrate on the Young's Laplace pressure, another cotton fabric (densely woven) designated as fabric-B was used for comparison purposes to fabricate sample Si30-B. Sample Si30-B was treated likewise by multilayer approach following preparation protocol of sample Si30. Using mercury intrusion porosimetry (MIP) measurements, porosities of both fabric-A (original) and B were characterized as 49% and 38% porous, respectively.

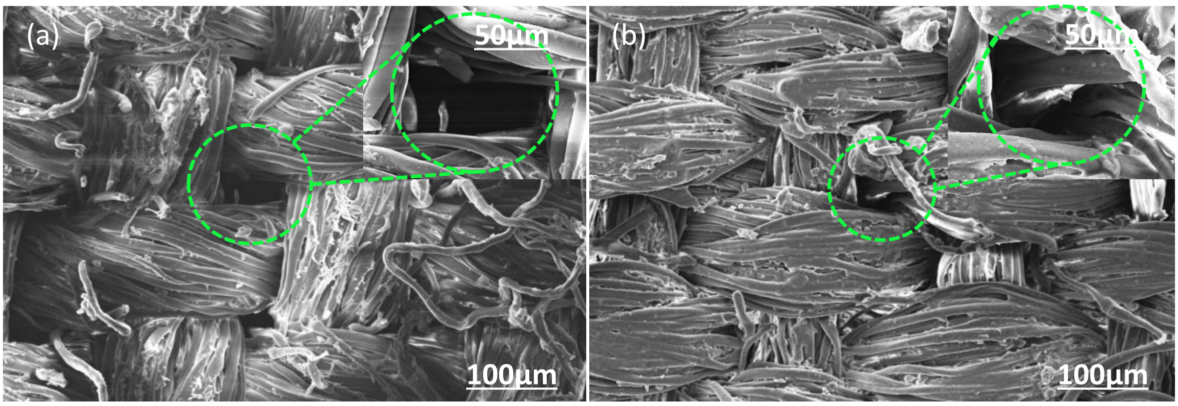

Fig. 2.6. SEM images of (a) fabric A and (b) fabric B after the identical multilayer hydrophobic treatment. Inset visuals show magnified fabrics pores.

Average pore radii of 17 μm and 9 μm were also calculated by the MIP measurements for fabric-A and fabric-B, respectively. Pore size estimation for samples CF, Si30 and Si30-B were made by scanning the samples at 50 different zones under the SEM, as shown in Fig. 2.6. Measurements were made by determining the minimum and maximum pore dimensions, D_{min} and D_{max}. Using these pore size measurements, Laplace pressures were calculated by equation 2.1,

$$\Delta P = 2\sigma \cos\theta_A [\frac{1}{D_{min}} + \frac{1}{D_{max}}] \tag{2.1}$$

where σ denotes the surface tension of water (72 mN/m at 20°C). We approximated $|\cos\theta_A| \approx 0.87$ since static WCA ($\theta \approx 150°$) is very close to a typical superhydrophobicity threshold[152]. Theoretical Laplace pressures were reported in Table 2.2 as a range corresponding to minimum and maximum dimensions of effective pores. Samples control CF and Si30 (fabric A) demonstrate similar estimated values in the range of 3-8 kPa as shown in Table 2.2. However, sample Si30-B (fabric B) has higher Laplace pressure range for penetration owing to its smaller pore dimensions in contrast to fabric A.

Table 2.2. Theoretical Laplace pressures vs experimental hydrostatic head pressures

Fabric	Sample treatment	D_{min} Range (μm)	D_{max} Range (μm)	Estimated Laplace pressure (kPa)	Experimental column height (cm)	Experimental Hydrohead (kPa)
A	CF	26—56	55—115	3—7	27.8±2.8	2.75±0.3
A	Si30	24—59	51—108	3—8	26.8±0.9	2.65±0.1
B	Si30-B	18—41	35—65	5—11	38.3±2.5	3.76±0.2

To verify above theoretical Laplace pressure values, hydrostatic head experiments were performed for all treated samples including Si30-B (Fig. 2.7). Untreated fabric being highly hydrophilic did not accumulate any water column at all allowing continuous water flow. Moreover, a rather poor performance was also measured for PMDS layer alone (control sample CS) in the case of hydrostatic head. As was shown earlier, fabric CS was also wet by large droplets and water blobs under static conditions. The fabric (sample CS) started leaking simultaneously from more than one point at a column height of about 7 cm as seen in Fig. 2.7.

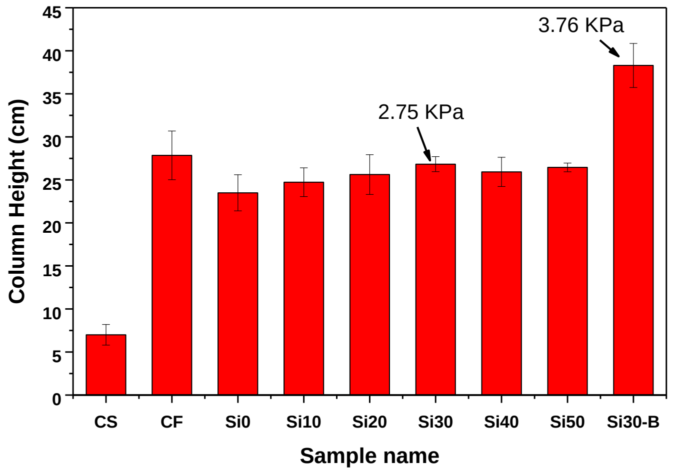

Fig. 2.7. Water penetration tests. Hydrostatic water column buildup height in cm for all treated fabrics (fabric-A). Column height of sample Si30-B with denser fabric structure (fabric-B) is also given for comparison.

It is interesting to note that the fabric treated with fluorinated acrylic copolymer (control fabric CF) displayed much better performance (more resistance to leakage) than silicone alone (sample CS). Equal performance levels are also observed in treatments with nanocomposite (control CF) or nanocomposites having PDMS outer layer (i.e., Si0, Si10, Si20, Si30, Si40 and Si50). As seen in Fig. 2.7, control sample CF and sample Si30 are practically same in terms of capillary pressure resistance with 28 cm and 27 cm column heights, respectively. Their corresponding experimental hydro-head pressures were calculated by equation 2.2,

$$p = \rho g h \tag{2.2}$$

where p is hydro-head pressure acting on the surface (Pa), h is the column height (m), ρ is the density of water (1000 kg/m^3) and g is the acceleration of gravity (9.81 m/s^2). The results of theoretical Laplace pressure and experimental hydro-head pressure are summarized in Table 2.2. The experimental hydro-head pressure acting on the fabric surface of samples CF and Si30 are 2.75 kPa and 2.65 kPa, respectively. Although, resistance to leakage of samples CF and Si30 is lower than the GoreTex fabaric (approx.100 cm), a number of simple techniques can be adopted to enhance this property. Such as, Jeong *et al.* found that this resistance to water column leakage can be enhanced by using multiple fabric layers and linings[15]. Another effective approach to elevate hydro-head resistance is to select appropriate fabric structure with even smaller pore radii. This has been demonstrated by a noticeable increase of column height 38 cm (Fig. 2.7) and the resultant hydro-head pressure of approximately 3.75 kPa with sample Si30-B (Fabric-B with small average pore radius) compared to the original cotton fabric. It can be seen from Table 2.2 that experimental hydro-head measurements are in good agreement with the lower estimated Laplace pressure values. This is generally attributed to the leakage through large pores even if statistically they constitute a minor portion of the porous structure[152,153].

2.4.5 Washing and abrasion resistance

Robustness of the best sample Si30 was tested against control sample CF by soaking them in tap water and agitating the system by a probe sonic processor for 2 minutes (frequency 20 kHz, power 750W and amplitude 40%)[20,148]. Note that this form of washing is much harsher than a normal laundry cycle[154,155]. Most publications on non-wettable fabrics that present washing tests generally apply bath sonication for about half an hour to an hour with an approximate power of ~O (10W) [20,148]. In order to visualize the effect of ultrasonic washing, washed samples were inspected with SEM and energy-dispersive X-ray spectroscopy (EDX). Figure 2.8 compares EDX signals of fabrics control sample CF (Figs. 2.8a and 2.8b) and Si30 (Figs. 2.8c and 2.8d) before and after washing. The data is the average of EDX spectra collected at 10 different locations on each sample. Ultrasonic agitation/washing of fabric sample CF forced a significant portion of the nanoparticles to debond from the fibers' surfaces as shown in Figs. 2.8a and 2.8b. Representative EDX maps are shown as insets.

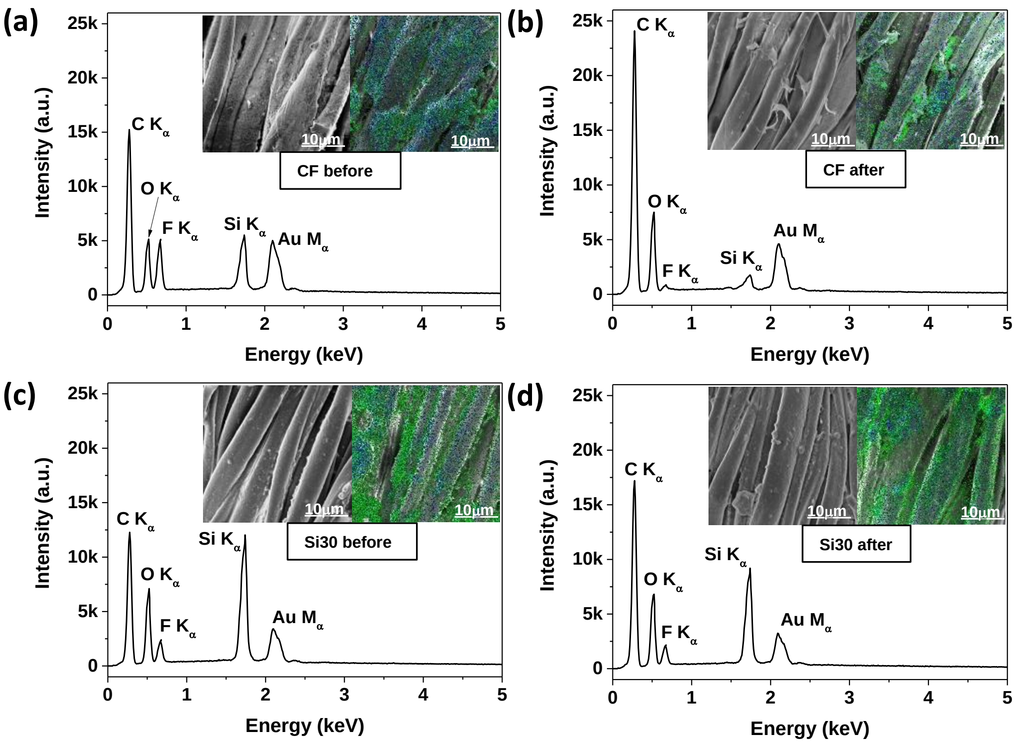

Fig. 2.8. EDX analysis of treated cotton fabrics after washing test. EDX spectra of nanocomposite fabric sample CF before (a) and after (b) ultrasonic washing. EDX spectra of PDMS coated nanocomposite fabric sample Si30 before (c) and after (d) ultrasonic washing. Representative SEM images and EDX mapping are given as insets with indication of silicon (green points) and fluorine (blue points).

Wetting tests after ultrasonic washing of the fabric CF showed that water droplets were immediately absorbed into the fabric just like an untreated fabric (see annex-I Fig. S2a). As seen in Fig. 2.8b, EDX measurements of control sample CF show a significant loss of intensity in fluorine ~80% and silicon ~70% signals due to the C-6 fluoropolymer and silica nanoparticles, respectively. This could be attributed to the physical detachment of both the polymer and nanoparticles from the fibers' surfaces. In contrast, fabric Si30, with the outer PDMS coating, remains virtually unaffected (approximately a 10% reduction in F signal intensity and 24% decline in Si signal intensity) after ultrasonic washing process (inset of Fig. 2.8c and 2.8d). After washing, sample Si30 maintained its original WCA ~150° and moreover small droplets could still roll off its surface upon tilting. Due to severe nature of the ultrasonic treatment used, the samples were not washed more than three times. At the end of the third cycle (drying in between every treatment), the best fabric sample (Si30) was still non-wettable and self-cleaning. Therefore, the acetoxy-PDMS outer coating not only resists droplet penetration in hydrophobicity tests (see appendix-I Fig. S2b) but also prevents ultrasonic washing induced loss of the underlying nanoparticles. This also intrinsically indicates a strong adhesion of the acetoxy-PDMS to the nanocomposite pretreated fabric surfaces. Indeed, this interaction between acetoxy-PDMS and the cellulose from the fabric was previously discussed in the ATR-FTIR spectroscopy section.

Durability of the hydrophobic modified control fabric CF and sample Si30 was further tested by using a standard linear abrasion tester. The applied weight was 0.35 kg (17.5 kPa) with stroke length of ~5 cm and stroke speed of 15 cycles/min. After every abrasion cycle, WCA (5 µL) and WSA (10 µL) of samples CF and Si30 were measured as shown in Fig. 2.9. Control fabric CF, treated only with the fluorinated polymer and silica NPs, demonstrated a noticeable change in hydrophobicity after the abrasion test. As shown in Fig. 2.9a, WCAs on sample CF fabric declined from 144° to 90° after just 17 abrasion cycles. Similarly, a relatively sharp increase in WSA was also measured after the first 9 abrasion cycles and roll-off angle increased form 42° to 90° as shown in Fig. 2.9b. Further abrasion of sample CF surface, makes it sticky and even large water droplets do not roll off at 90° tilt angles. This is attributed to physical abrasion and resultant particle and polymer wear and removal from the fibers' surfaces. Inspection of SEM images before and after abrasion cycles supports this reasoning (see appendix-I, Fig. S3a and S3b, inset). EDX measurements also showed a significant decrease in the intensities of fluorine ~50% and silicon ~30% signals (see appendix-I, Figs. S3a and S3b).

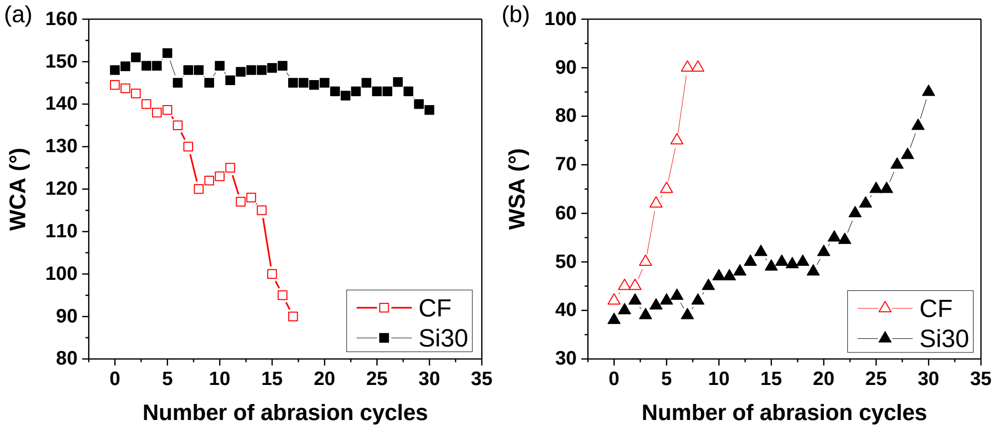

Figure 2.9. Effect of wear abrasion on the wetting characteristics of control fabric CF and sample Si30. (a) Static water contact angle changes as a function of abrasion cycles and (b) water roll-off or sliding angle measurements as a function of abrasion cycles.

Samples Si30, on the other hand, demonstrated better resilience against wear abrasion. As shown in Fig. 2.9a WCAs on sample Si30 changed from 148° to 138° after 30 abrasion cycles. At the same time, as seen in Fig. 2.9b water roll-off angles on the abraded fabric Si30 also increased, however droplet mobility on the abraded surfaces was still maintained at the end of 30 abrasion cycles. The measurements were stopped after 30 abrasion cycles due to fact that almost 90^{o} droplet roll off angle was obtained, indicating highly hysteretic hydrophobicity due to abrasion. SEM images of the fabric Si30 before and after abrasion tests showed no significant alteration of fibers' surface morphology (see appendix-I, Fig. S3c and S3d), however, an increase in the number of fiber beads and floating fibers were noticed. EDX measurements of sample Si30 after 30 abrasion cycles exhibited a negligible change of intensity in silicon signals (< 10%). Interestingly, a significant increase of intensity in fluorine ~40% signals was recorded by EDX measurements (see appendix-I, Fig. S3c and S3d). Note that the EDX silicon signals come from both the polymer and the nanoparticles. The increase in the fluorine signal intensity could be attributed to the wearing of some of the PDMS layer exposing the underlying fluoropolymer-silica nanocomposite.

2.4.6 Mechanical Stress–Strain Characteristics

Mechanical strength and flexibility of textile fabrics are prime parameters for quality and hence it is important to achieve water repellency without altering the fabric's mechanical characteristics to a significant extent[136]. Usually, to predict the mechanical behavior of textile fabrics, tensile stress-strain curves are considered. In general, textile woven fabrics show J-shaped stress-strain curves similar to soft elastomeric polymers or some biological tissues[139,156,157]. This indicates a nonlinear stress-strain zone at initial stages that can be attributed to the basic structure of the fabric such as weave, crimp (wave form of threads in woven structure), fiber (or yarn) slippage and warp-weft interactions[158,159]. Physically, plain woven fabric has high yarn crimps due to large number of warp-weft intersections. Therefore, it exhibits larger tensile strain under small stress at initial stages[160]. During extension of the fabrics, first decrimping and later fiber slippage occurs in the direction of extension resulting in high strain. However, under strain, mechanical behaviour of coated (treated) woven fabrics can differ from the original fabric depending on the treatment (chemical functionalization or polymer coating) and dry weight pick-up due to such coatings. In this study, typical J-shaped stress-strain curves were obtained from all treated fabrics as shown in Fig. 2.10a. However, stress-strain curves were segregated in two distinct groups depending on their treatment type. Fluoropolymer treated fabrics (including nanocomposites) followed the untreated fabric behaviour whereas PDMS coated fabrics (single or multilayer) were stiffer. For comparison, stress-strain measurements obtained from the control fabric CS and multilayer sample Si30 (fabrics containing the PDMS coatings), differ significantly from the control fabric CF that display almost identical behaviour to the untreated fabric. The shape of the stress-strain curves of fabrics CS and Si30 is not as nonlinear as the others, which becomes linear after 15% strain rate. Moreover, these fabrics resist elongation more than the other untreated and just fluorinated polymer coated fabrics, namely 25 % elongation requires around 30 MPa stress compared to ~17 MPa stress.

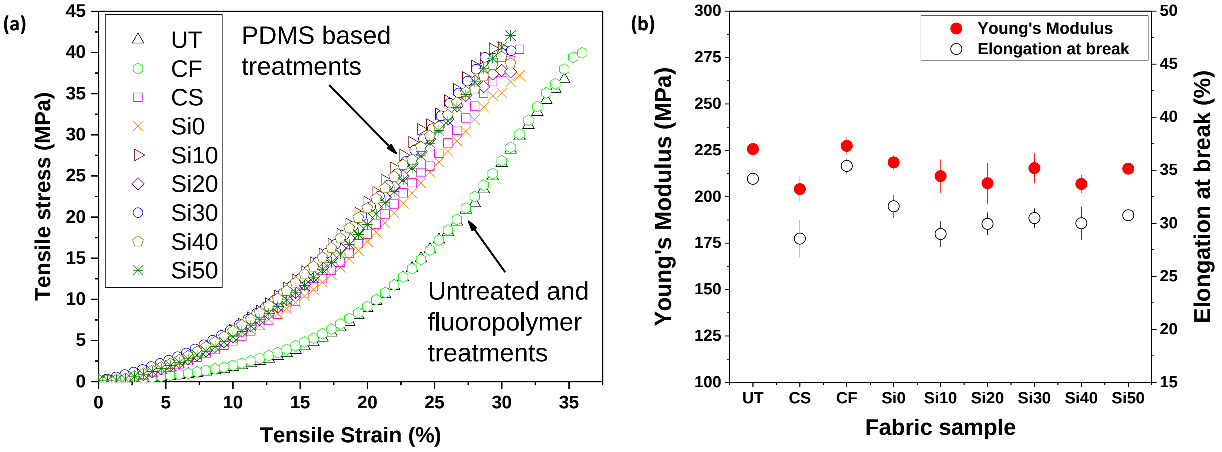

Fig. 2.10. Mechanical characterization. (a) Representative stress-strain curves of untreated (UT), control fabrics and all treated fabrics. (b) Young's Modulu (MPa) and maximum percent elongation at break point of all single and multilayer treated fabrics.

Fabrics CS and Si30 fracture at around 30% strain whereas all the other fabrics fracture around 35% strain. Clearly, the acetoxy-PDMS treatment alters to some extend the mechanical properties of both the untreated and the nanocomposite treated fabrics. As also seen in Fig. 2.10a, fluoropolymer treatments with or without nanoparticles do not induce any mechanical changes compared to untreated fabric. The nonlinear stress-strain section of these fabrics extends up to 25% strain. This could be mainly attributed to the very low dry pick up weight (1%) of the fluoropolymer treatment. As mentioned earlier this was intentional in order to maintain a minimum amount of fluorine chemistry. Whereas, acetoxy-PDMS dry pick up weight was 10% and this somewhat changed the mechanical properties of the woven fabric. Acetoxy-PDMS has strong adhesion and bonding affinity towards cellulosic surfaces[161]. Such strong adhesive interactions between the fibers and the polymer interferes with the thread movement and fiber slippage causing decreased flexibility and in certain cases decreased tensile strength[46,136,162]. Fig. 2.10b summarizes all the mechanical properties extracted from the stress-strain curves where it is clear that PDMS finished fabrics have altered mechanical characteristics but certainly without very significant changes with respect to the original fabrics. Since fabric Si30 displays the best hydrophobic performance, it suffices to argue that as a result of this treatment, no significant deterioration or loss in the mechanical characteristics (Young's modulus and maximum elongation at break) of the original fabric occurs.

2.5 Conclusion

Woven cotton fabrics were rendered water repellent by applying a sequential polymer treatment comprising a polymer-silica nanocomposite and a silicone resin, which preserves the porosity and the breathability of the original fabrics. Both polymers, namely, C-6 perfluorinated acrylic copolymer and acetoxy-cure silicone (PDMS) resin are environmentally friendly and non-toxic. Treated cotton fabrics also demonstrated resistance to water penetration due to hydrostatic pressure build-up. Water repellent characteristics were demonstrated by water droplets (20 µL) that easily rolled-off well below 20^o. Even impinging small droplets (8 µL) could be repelled with corresponding droplet roll-off angle of 17°. Additionally, treated fabrics were also able to hold a hydrostatic head pressure of 2.56 kPa (equal to 26 cm water column height) before leak. Hydrophobic durability of the cotton fabrics was tested by ultrasonic washing and wear abrasion tests. Furthermore, treated fabrics resisted wear abrasion under 17.5 kPa up to 30 abrasion cycles. The ease of application technique, industrial scale availability of the low-cost polymers and the non-toxic ingredients would allow this fabric treatment to be implemented in large scale textile treatment facilities. Moreover, developed fabrics can be further tested in applications such as filtering, oil-water separation and as special bags for organic oil spills cleaning.

Chapter: 3

PEDOT:PSS/Graphene based conductive cotton fabrics

3.1 Introduction

Recently, fiber-based conductive materials have gained a considerable attention of the researchers because of their flexibility, mechanical strength, porosity and conformal properties[59]. Therefore, conductive textiles are being increasingly implemented for thermos-regulated fabrics[52], sensor[68,74,87], static charge dissipation[53], data processing[64,163], power storage[65,164], signals and power transportation [55,61,73] in military gears, medical sensors, sports or leisure wears. For this, intrinsic conducting polymers (ICPs) with highest conformal flexibility are considered as best candidates for such applications. Namely, polyaniline[71,72], polypyrrole[52,62,73,165] and polythiophenes[75,78–80,95,166] have been extensively implement in conductive textile fabrics. Particularly, poly(3,4-ehtylenedioxythiophene) (PEDOT), a derivative of polythiophenes deserves special attention because of it highly conjugated backbone, high environmental stability than polyaniline and polypyrrole, biocompatibility[82] and film forming properties[81]. Moreover, after making a polymer complex with poly(styrene sulfonate) (PSS), PEDOT:PSS polymer complexes can easily be processed into aqueous solution or non-toxic, green solvents like 2-propanol[85,167]. PEDOT:PSS solutions can be applied onto textiles structures using a number of simple fabrication techniques, such as, digital printing[87,94], layer-by-layer assembling[95], solution immersion or dip-dry method[76,79,80,168] and spray coating[52,68].

3.2 Objectives

This study focuses on the fabrication process for a highly conductive, breathable, mechanically strong cotton fabric for strain-sensing and supercapacitor applications. A simple approach of mixing carbon based materials (graphene nanoplatelets, GNPs) with conductive polymer (PEDOT:PSS) have been investigated to achieve high conductivity without altering physical properties (porosity, weight, strength) of the prepared fabric. For this, PEDOT:PSS plays a dual role of binding GNPs to fibre’s surfaces and enhancing conductivity of the prepared fabrics by its conjugated backbone. The prepared conductive cotton fabrics are characterized for their morphology, chemical interactions, mechanical strength, resistance to bending-unbending events and successive washing cycles.

3.3 Materials and methods

3.3.1 Materials

Plain woven 100% cotton fabric with 120 ± 5 g/m^2 density and having 83/cm warp and 36/cm weft threads was purchased from Cotoneficio Albini (Italy). PEDOT:PSS microgel dispersion (CLEVIOS^{TM} P, CPP 105D) conductive polymer complex was purchased from Heraeus (Germany). According to the manufacturer, the dispersion contains ca. 43% by weight PEDOT:PSS polymer and the rest being isopropanol with other dispersants and stabilizers. Particularly, it contains an epoxy functionalized silane component as binding agent. GNPs (Ultra-G$^+$) were provided by Directa Plus Spa (Italy). Detailed characterizations of the GNPs are given elsewhere[169] (also see appendix-I, Fig. S4). NaOH, Polyethylene glycol (PEG), dimethyl sulfoxide (DMSO), d-sorbitol and 2-propanol (all Sigma Aldrich) were used without any further purification. All the materials/solvents used in this work are non-toxic and biocompatible[82].

3.3.2 Sample preparation

Cotton fabrics (5 × 5 cm^2 sample size) were mercerized by dipping in aqueous 5M NaOH solutions for 5 minutes, rinsed twice and dried before applying the conductive coating. For spray coating, PEDOT:PSS solutions were further diluted with isopropanol to 1 wt.%. GNPs were blended with PEDOT:PSS in solution at different mass fractions, such as, PEDOT:PSS/GNPs-100/0 (GNPs-0%), 90/10 (GNPs-10%), 80/20 (GNPs-20%), 70/30 (GNPs-30%), 60/40 (GNPs-40%) and 50/50 (GNPs-50%) keeping total solid content of 1 wt.% in the solutions. Hereafter, the conducting fabrics will be referred as, for instance, GNPs-0% (only PEDOT treated) and GNPs-20%, containing 20% GNPs with respect to total polymer and GNP dry weight.

The conductive solutions were bath sonicated for 8 hours at 59 kHz, 135 W and amplitude of 100% (Savatec, Italy) and then probe sonicated for 2 minutes at 20 kHz, 750 W and amplitude of 40% (vibra cell™ XCV-750, Sonics and Materials Inc. USA). Ten ml solution for each GNPs mass fraction was sprayed onto both sides of the fabric sample using airbrush spray system (VL Siphon feed, 0.73 mm nozzle, Paasche airbrush, US). During spray coating, nozzle to fabric distance and spray pressure were maintained at 15 cm and 2.5 bar, respectively. After 2 spraying cycles with hot air gun drying in between, a dry pick-up of 10% - 12% w.r.t pristine fabric weight or mass loading of 1.25 – 1.50 mg/cm^2 was measured. Dried fabrics were thermally cured in a convection oven for 30 min at 130°C and afterwards, conditioned for 24 hours at 23 ± 1°C and 65 ± 2% relative humidity prior to characterizations.

3.3.3 Characterization

3.3.3.1 Microscopic morphology

For surface analysis of the untreated and treated textiles, scanning electron microscopy (SEM) JEOL-6490AL (Japan) was used. All SEM images were acquired without gold sputter coatings, however, untreated cotton fabrics were sputter coated (~ 10 nm) prior to imaging. SEM images were captured at different magnifications using accelerating voltages of 10 kV and 15 kV. For certain samples energy dispersive X-ray (EDX) analysis were also performed at 10 kV acceleration voltage, 10 mm working distance and 15 sweep counts to see chemical compositions. The morphology of GNPs were analysed by TEM (JOEL JEM 1011 instrument, Japan) with an acceleration voltage of 100 kV. The samples were dispersed in ethanol by bath sonication and 20 μL was dropped on copper TEM grids (200 mesh), which were then dried overnight under vacuum.

3.3.3.2 Attenuated Total Reflection-Fourier Transform Infrared (ATR-FTIR) Spectroscopy

Infrared spectra of different samples were obtained with a FTIR spectrometer (Equinox 70 FT-IR, Bruker) equipped with an ATR accessory (MIRacle ATR, PIKE Technologies). All spectra were recorded in the range from 4000 to 600 cm^{-1} with 4 cm^{-1} resolution, accumulating 128 scans. To ensure the reproducibility of obtained spectra three samples of each type were measured.

3.3.3.3 Raman spectroscopy

Chemical characterization of the conductive cotton fabrics was further studied by μRaman spectroscopy (Renishaw Invia, United Kingdom). A 514 nm laser excitation line through a 100x objective lens (numerical aperture 0.75) was used to excite the specimens, at low power of 0.4 mW. The spectral region scanned was 3500–100 cm^{-1} with a spectral resolution of approximately 1 cm^{-1}. All the spectra were normalized to their maximum. Eight to 10 μRaman measurements were performed to minimize uncertainty in measurements.

3.3.3.4 Mechanical characterization

Stress-strain properties of the conducting fabrics were measured using an Instron (3365 Instron, USA) instrument according to ASTM D3505 test method. A dog-bone shaped sample strip of 25 mm length along the axis of warp threads and 4 mm width was cut by a mechanical cutter and held by pneumatic clamps in the testing instrument. Fabric samples were extended at a constant strain rate of 5 mm/min. Engineering stress-strain curves, Young’s modulus in MPa (slope of the stress-strain curves in elastic region before rupture) and elongation at break (%) of 5 samples for untreated and treated cotton fabrics were automatically recorded by Instron software with standard deviations.

3.3.3.5 Water vapor permeability

Breathability of the conductive cotton fabrics was measured by water vapor permeability (WVP) technique, using metallic permeation cells. The WVP of fabrics was determined at 25 °C and under 100% relative humidity gradient (ΔRH%) according to the ASTM E96 standard method. 450 µL of deionized water (which generates 100% RH inside the permeation cell) was placed in each test permeation cell with a 7 mm inner diameter and a 10 mm inner depth. Fabrics were cut into circles and mounted on the top of the permeation cells. The permeation cells were placed in 0% RH desiccator with anhydrous silica gel used as a desiccant agent. The water transferred through the fabric pores was determined from the weight change of the permeation cell every hour during the first 8 h using an electronic balance (0.0001 g accuracy). The weight loss of the permeation cells was plotted as a function of time. The slope of each line was calculated by linear fitting. Then, the water vapour transfer rate (WVTR) was determined as below[170,171],

$$\mathrm{WVTR}\ (\mathrm{g}(\mathrm{m}^2\mathrm{d})^{-1} = \frac{\mathrm{Slope}}{\text{area of the fabric}} \tag{3.1}$$

WVP measurements were replicated three times for each fabric sample. The WVP of the fabrics were calculated as follows;

$$\mathrm{WVP}\ (\mathrm{g}(\mathrm{md\ Pa})^{-1} = \frac{\mathrm{WTVR} \times l \times 100}{\rho_{\mathrm{S}} \times \Delta\mathrm{RH}} \tag{3.2}$$

where l (m) is the fabric thickness, measured with a micrometer with 0.001 mm accuracy, ΔRH (%) is the percentage relative humidity gradient, and p_s (Pa) is the saturation water vapor pressure at 25 °C (3168 Pa).

3.3.3.6 Washing durability

The washing durability of the selected conductive sample GNPs-20% was conducted in the laboratory under constant stirring. The fabric specimen were washed in a capped bottle containing 200 ml distilled water and 0.37 % w/w of a neutral washing detergent (pH ~7.0)[74]. Sample GNPs-20% was washed simultaneously with another sample (GNPs-0%) in the same bottle to replicate the fabric to fabric wear abrasion. During each cycle, washing solutions were heated at 45 ± 2 °C for 30 min with intense stirring. Afterwards, samples were rinsed, dried and conditioned at a relative humidity of 65 ± 2% and a temperature of 20 ± 1 °C for 1 h before resistance measurements (Ω/cm).

Average of three measurements after each washing cycles is reported as normalized R/R_0 ratio with standard deviations. Silver contacts were used to measure the relative resistance as well.

3.3.3.7 Electrical properties

Electrical properties of the prepared samples were measured by using Signatone 1160 probe station (Microworld, France). A Keithley 2612A sourcemeter (Tektronix, Inc. US) was used to record voltage-current curves during measurements. Square samples of 5 × 5 mm^2 sheet area were prepared and fixed by double stick adhesive tape onto glass slides. Silver paint (RS silver conductive paint, resistivity ≈ 0.001 Ω/cm) electrodes of 5.0 × 2.5 mm^2 size were painted on the conductive surfaces 5 mm apart in order to minimize contact resistances between the probes and the fabrics. A real sample for he sheet resistance measurements have been shown in Fig. 3.1. An electrical voltage of 2.0 V was applied on contacts along the warp direction. The bulk resistance of the samples was calculated by taking the slope of the recorded V-I curves. Three samples for each GNPs mass percentage were measured and average values are reported with standard deviations. An electrical potential of 2.0 V was intentionally used as most of the smart wearable devices operate at 1.0-5.0 V voltage range[172,173]. The fabrics were also tested at higher voltages and all displayed ohmic resistor behaviour up to 7.0 V. The sheet resistance (Ω/□ or Ω/sq.) was calculated by using the formula:

$$R_s = \rho \frac{L}{W \cdot t} \tag{3.3}$$

where, R_s is sheet resistance, ρ is specific resistivity of the bulk, L is length, W is width and t is thickness of the treated fabric (~0.25 mm). Since our measurements were performed at a square fabric area (W=L), and the thickness was kept constant, the value of sheet resistance becomes dependent only on the specific resistivity ($R_s \propto \rho$). The bulk conductivity was calculated by inversing specific resistivity[75].

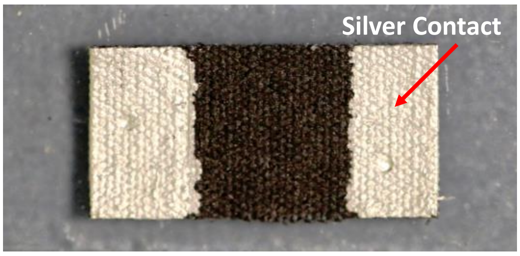

Fig. 3.1. Sample for sheet resistance measurement with 5 × 5 mm^2 surface area. Highly conductive silver paint was used to make contacts of 5 × 2.5 mm^2 size on both ends.

3.3.3.8 Changes in fabric resistance under cyclic strain deformation

Cyclic strain deformation is defined as reversible change in electrical resistance of a material when subjected to a cyclic strain (ε = ratio of change in length to original length, $\Delta L/L$). The resulting strain sensitivity is further characterized by a term known as gauge factor defined by the following equation [74],

$$\mathrm{GF} = \frac{1}{\varepsilon}\frac{\Delta \mathrm{R}}{R_0} \tag{3.4}$$

where, ΔR is the change in resistance at a given strain, R_0 is the initial resistance and ε is the applied strain. The effect of cyclic extension (ε) on the resistance change (ΔR) was evaluated on a micro uniaxial testing stage (Deben, UK, custom design). Strip samples of 15 × 4 mm^2 size along warp direction were prepared for this purpose. Conductive silver paint electrodes were made on the samples with 10 mm spacing. For measurements, a strip-shaped fabric was placed and fixed between clamps separated by 10 mm. Electrodes were connected to the sliver painted ends of the mounted sample. Electrical voltage corresponding to 1.0 V was applied using a Keithley 2612A sourcemeter (Tektronix, Inc. US) and the initial resistance R_0 at zero deformation was recorded. 100 deformation cycles were applied at strain rate of 5 mm/min, both in loading and unloading directions. The mounted samples were displaced by 0.5 mm and 1 mm corresponding to 5 % and 10 % strain, respectively[87,174]. Changes in resistance R were recorded both in extension and relaxation modes during each deformation cycle. For reproducibility, five repetitions on each sample were performed. Up to 1000 deformation cycles were performed to monitor longer term effects of the cyclic strain deformation.

3.3.3.9 Severe folding-unfolding resistance test

Fatigue induced resistance changes due to weight-pressed folding were measured by performing repetitive folding-unfolding cycles[67,175]. The 180° folding line was induced by placing the folded fabric under a 0.5 kg metal weight for 1 min. Subsequently, the fabric was unfolded and allowed to rest for an additional minute before measuring electrical resistance R (Ω/cm) across the fold line. Silver paint contacts were applied at 3 different positons along the fold line 1 cm apart from one another on both sides of the fabric. A digital multimeter was used for electrical resistance measurements. The average values of "R_0" before folding and "R" after each folding cycle were recorded with their standard deviations. Overall, six measurements were collected (three from each side of the fabric) and the average change in the normalized R/R_0 ratio was reported as a function of number of folding cycles.

3.3.3.10 Fabrication of supercapacitor and capacitance measurements

Symmetrical solid-state supercapacitors were fabricated using two conductive textile with similar coatings (dimension 1 cm x 1cm) separated by a dried glass fibers membrane (Whatman GF/D) which was soaked into 200 µL of 1.2 M tetraethylammonium tetrafluoroborate (TEABF4) in Acetonitrile. Cells were made in a coin cell configuration inside a MBraun glovebox, with H_2O and O_2 levels below 0.1 ppm. All cells were electrochemically tested using BioLogic BCS-805 multichannel battery unit controlled by BT Lab V1.30 at ambient conditions. Cyclic voltammetry and Galvano-static measurements were performed in a potential range of 0-1.5 V using different scan and current rates.

3.4 Results and discussion

3.4.1 Surface micro-morphology

The fabrics were coated by spraying diluted PEDOT:PSS solutions containing different quantities of GNPs. Fig. 3.2 shows SEM images of the untreated mercerized cotton fabric, PEDOT:PSS coated fabric (GNPs-0%; on dry basis) and graphene treated fabrics with, GNPs-10%, GNPs-20%, GNPs-30% and GNPs-50%, respectively. Unlike convoluted fibrous structures in the pristine cotton fabric without mercerization, untreated mercerized cotton fabric exhibits a closely packed, intermeshed network of round cellulosic fibres[176], as shown in Fig. 3.2a. Whereas, as shown in Fig 3.2b, the fabric surface treated with GNPs-0% (only PEDOT:PSS treatment) appears to be evenly coated with the conjugated polymer. No PEDOT:PSS polymer aggregation zones or phase separation on the fibers is noticeable.

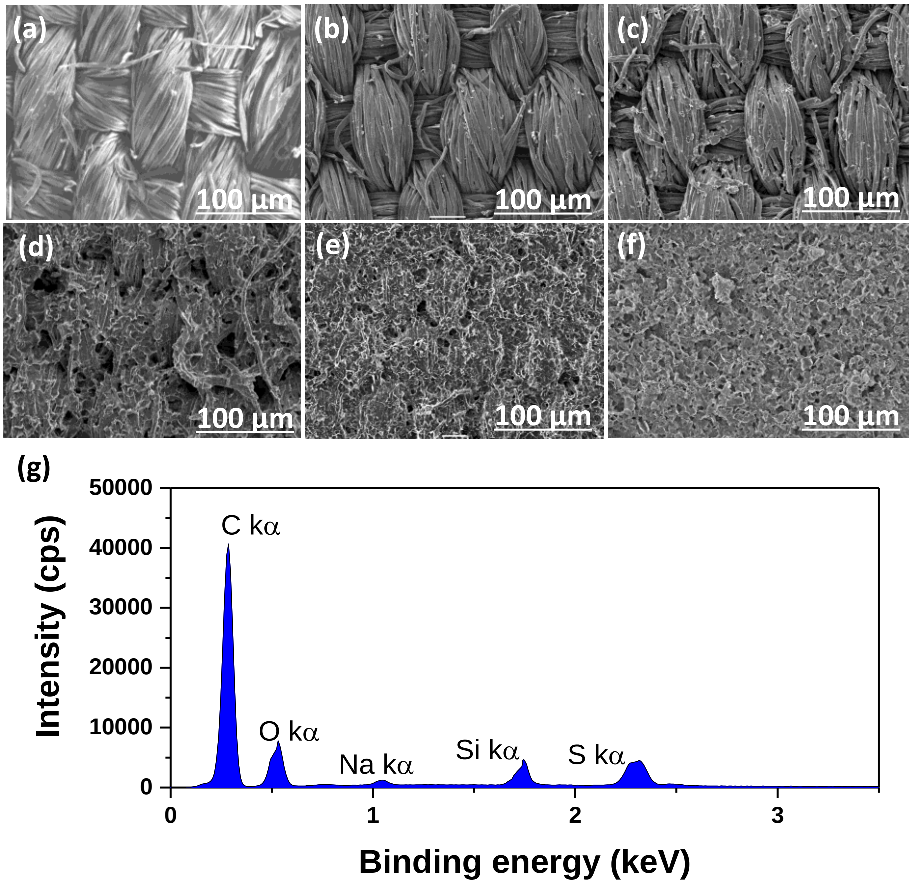

Fig. 3.2. SEM image of (a) untreated mercerized cotton fabric, (b) only PEDOT:PSS coated fabric (GNPs-0%), (c) sample GNPs-10%, (d) sample GNPs-20%, (e) sample GNPs-30% and (f) sample GNPs-50% coated with graphene nanofillers and conductive polymer. (f) EDX spectra of the GNPs-20% conductive cotton fabric for composition analysis.

For coatings containing GNPs, coating uniformity directly influenced final electrical properties of the fabric[68]. For instance, fabrics treated with GNPs-10% displayed isolated fragments/islands of stacked graphene layers on the fiber network as shown in Fig. 3.2c. No continuous well-interconnected network of GNPs was established at this mass ratio. Increasing GNPs concentration in the solution resulted in the formation of a microporous but interconnected coating layer on the fabric surface (Fig. 3.2d, GNPs-20%); even though, some underlying woven fiber bundles were still visible as seen in Fig. 3.2d. This fabric was evaluated to be the best performing among others, as will be demonstrated in next sections of this chapter. The fabric treated with GNPs-30% solutions, for instance, appears to have less porosity (Fig. 3.2e) but it displayed very poor adhesion characteristics and coating failure upon simple rubbing or bending. Further increase in GNPs concentration with respect to PEDOT:PSS (for GNPs-50%, see Fig. 3.2f) worsened this problem, rendering the textile durability very poor against mild wear and folding.

Energy dispersive X-ray spectroscopy (EDX) measurements performed on fabrics treated with GNPs-20% solutions demonstrated existence of a trace Na signal, located at 1.045 keV, due to prior mercerization of the cotton fibers, as shown in Fig. 3.2g. An additional peak at 2.307 keV is attributed to the atomic sulphur in thiophene ring and sulfonic groups of PEDOT:PSS[78,177]. More importantly, as seen in Fig. 3.2g, the silicon peak at 1.74 keV confirms the presence of epoxy-silane binder which was crucial in retaining the GNPs in the coating matrix .

3.4.2 Chemical analysis

Mercerization of cotton fabric causes neutralization of polysulfonic acid groups upon the application of the conductive coatings[90]. It also affects the cellulosic structure of cotton. As shown in Fig. 3.3, FTIR spectra of as-received cotton fabric show well-known distinct bands associated with pure cellulose structure, namely, O-H stretching at 3364 cm^{-1}, C-H stretching at 2891 cm^{-1}, adsorbed water at 1645 cm^{-1}, ring breathing at 1157 cm^{-1} and C-O stretching at 1026 cm^{-1}[144]. However, after mercerization, significant broadening of the peak attributed to O-H stretching at 3100-3400 cm^{-1} appears, indicating transformation of cellulose-I to cellulose-II structures and associated changes in inter and intra-molecular hydrogen bonds, as shown in Fig. 3.3 (enlarged image)[178]. Furthermore, Raman spectroscopy was used to confirm the mercerization effect and to analyse the potential chemical interactions between the conductive polymer and cotton fibres. Thickness or approximate graphene layers constituting GNPs used were also estimated based on Raman analysis. For instance, Raman signals of the mercerization effect on cotton fabric were detected at 1461 cm^{-1}, which is attributed to crystallinity of cellulose and at 896 cm^{-1} which is the bending mode of 6th carbon atom in the Cellulose-I structure[179]. Upon mercerization, the intensity of the band at 1461 cm^{-1} decreases while the intensity of the band at 896 cm^{-1} increases (see appendix-I, inset of Fig. S5), both of which are related to transition from Cellulose-I to Cellulose –II [179].

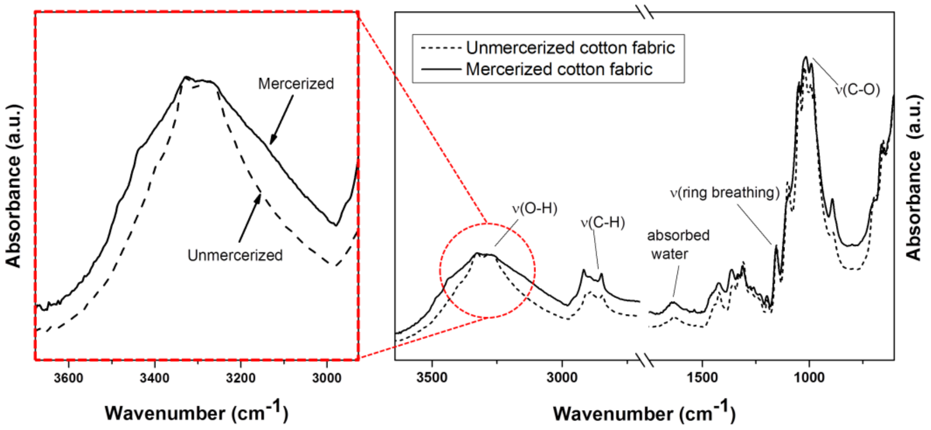

Fig. 3.3. FTIR spectra of unmercerized (dotted line) and mercerized (solid line) untreated cotton fabric. Different vibrations attributed to cellulose structure have been assigned. Effect of mercerization treatment on cellulosic structure is indicated as peak broadening.

When mercerized cotton fabrics were treated with PEDOT:PSS or PEDOT:PSS/GNPs coatings, strong vibrations attributed to thiophene rings and sulfonic acid groups appear between 400 cm^{-1} and 1600 cm^{-1} wavenumbers, confirming coating consistency over cotton fibres. Herein, for brevity, the Raman spectra of most relevant fabrics have been presented. As shown in Fig. 3.4, two conductive cotton fabrics, namely, sample GNPs-0% and sample GNPs-20% exhibit several well-known Raman peaks at 1538 cm^{-1}, 1440 cm^{-1}, 1365 cm^{-1} and 1258 cm^{-1} associated with C_α=C_β asymmetric stretching, C_α=C_β symmetric stretching, C_β-C_β stretching deformation and C_α=C_α inter-ring stretching of the thiophenes (PEDOT), respectively[86,180]. The vibrational contribution of PEDOT quinoidal structure is also visible at 1543 cm^{-1}[181], and two small peaks associated with oxyethylene ring deformation can be located at 989 cm^{-1} and 577 cm^{-1}[182]. The acidic contribution of SO_2 sulfonic group from PSS component is also detected at 440 cm^{-1}.

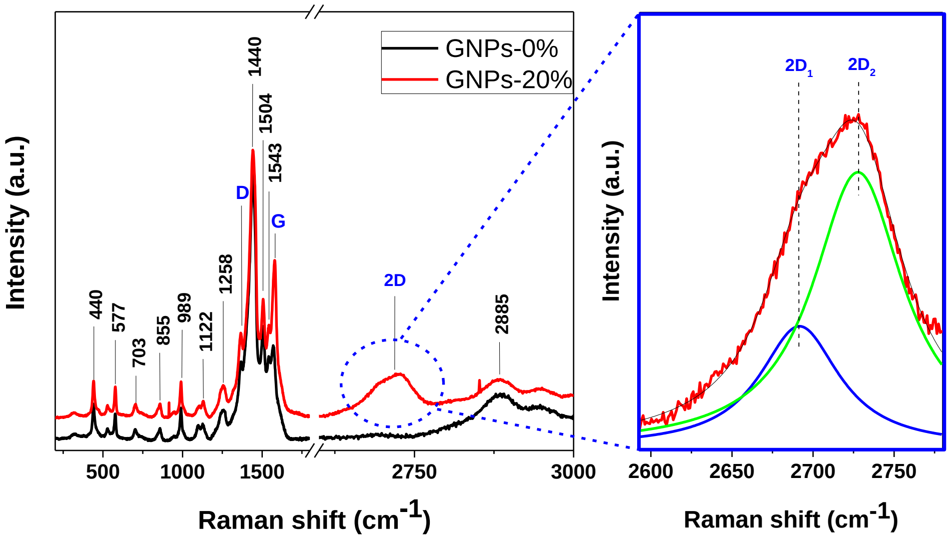

Fig. 3.4. Raman spectra of the conductive cotton fabric with only conductive polymer PEDOT:PSS (sample GNPs-0%) and PEDOT:PSS/GNPs coated nanocomposite (sample GNPs-20%). Different vibrations attributed to PEDOT:PSS and GNPs have been assigned in black and blue colours, respectively. The inset shows the deconvolution of the GNPs 2D peak (second order of zone-boundary phonons), into 2D$_1$ and 2D$_2$ peaks.

On the other hand, the conductive fabric sample GNPs-20% demonstrates bands related to the state of GNPs utilized (Fig. 3.4). Vibration bands at 1365 cm^{-1}, 1585 cm^{-1} and ~2700 cm^{-1} in the Raman spectra are associated with D peak (disordered structure of graphene), G peak (stretching of the C-C bond in sp^2 hybridised carbon atoms) and 2D peak (the second order of zone-boundary phonons), respectively[183]. A typical single layer graphene demonstrates a sharp high intensity 2D peak exceeding the intensity of the G peak. In multilayer GNPs, this peak appears broader and smaller in intensity compared to G. It can be deconvoluted into two peaks, namely $2D_1$ and $2D_2$[184] and if the intensity of $2D_2 > 2D_1$ like it happens in our samples (Fig. 3.4 enlarged part) then the GNPs are considered to be more graphitic material with stacks of more than 8 graphene layers [169,184].

3.4.3 Mechanical properties

As mentioned earlier, the highly acidic nature of PEDOT:PS solution ($pH < 2.0$) hydrolyzes the cellulose backbone of cotton and this effect directly translates into a major loss of mechanical properties. In Fig. 3.5a, changes in the mechanical properties of the fabric due to mercerization and to PEDOT:PSS treatment, applied to both mercerized and as-received fabrics, are shown. As received cotton fabric demonstrated a J-shaped stress-strain behavior somewhat similar to elastomeric polymers and biological tissues [157] but with only 50% strain before break. Direct application of PEDOT:PSS solution on as-received cotton fabric results in a very significant deterioration in stress and strain values before break. Namely, the treated fabric stretches only by 10% before break and the tensile stress before break occurs at 7 MPa instead of 73 MPa (Fig. 3.5a). Moreover, as indicated in Table 3.1, approximately 80% of the original elastic modulus is lost upon PEDOT:PSS treatment.

Mercerization effect on the as-received fabric is reflected as an increase in elongation at break by ca. 60% and as stress at break reduction by about 10 MPa. These changes are well-known in textile industry and are attributed to the structural and bonding changes in cellulose/cotton due to alkaline treatment[176,185]. When this fabric is treated with PEDOT:PSS (GNPs-0% in Fig. 3.5a), even though both the stress and strain at break values decline to 30 MPa and 23%, respectively, the J-shaped characteristic fabric stress-strain behaviour is preserved and the Young's or elastic modulus only reduces by 25%, compared to 80% reduction without mercerization (see Fig. 3.5a and Table 3.1). This improvement is accredited to the neutralization effect of NaOH on sulfonic acid (see inset in Fig. 3.5a), partially preventing acidic hydrolysis of cotton[90].

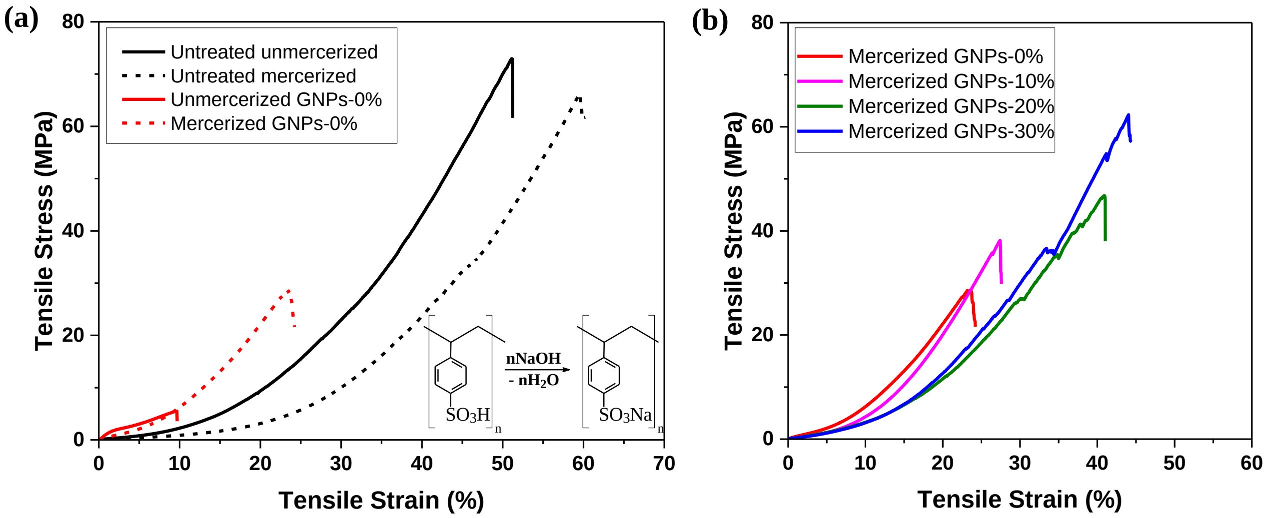

Fig. 3.5. (a) Stress-strain curves of untreated and only PEDOT:PSS coated cotton fabrics (sample GNPs-0%) with and without mercerization treatment. (b) Mechanical recovery after mercerization of different GNPs coated fabrics, such as, 10%, 20% and 30% (the Mercerized GNPs-0% fabric is also shown for direct comparison reasons).

Fig. 3.5b shows stress-strain curves of various mercerized conducting cotton fabrics with different mass fractions of GNPs. As seen in Table 3.1, use of GNPs with PEDOT:PSS definitely enhances elastic modulus that is initially lost due to sulfonic acid effect on the as-received fabric, but with very little effect on elongation at break, particularly for samples GNPs-20% and GNPs-30%. After mercerization, increase in both elastic modulus, and elongation at break values (approx. two fold for all samples GNPs>10%) was measured compared to pure PEDOT:PSS treatment after mercerization (Table 3.1). In conclusion, the fabric designated by GNPs-20% was chosen as the best sample both in terms of stress-strain behaviour as well as final weight and physical appearance.

Table 3.1. Summary of mechanical properties. Uncertainty levels in Young’s modulus and elongation at break are ± 10 MPa and ± 2 %, respectively.

Treatment	Before mercerization		After mercerization	
	Young’s modulus (MPa)	Max. elongation at break (%)	Young’s modulus (MPa)	Max. elongation at break (%)
Untreated	278	51	273	60
GNPs-0%	55	10	205	23

GNPs-10%	63	12	236	27
GNPs-20%	150	14	200	41
GNPs-30%	168	17	257	44
GNPs-40%	175	18	268	44
GNPs-50%	210	21	266	47

3.4.4 Breathability

For breathability of the treated fabrics, two conductive cotton fabrics, GNPs-0% and GNPs-20% were characterized for their water vapour permeability (WVP) and water vapour transfer rate (WVTR). Additionally, pristine (unmercerized) and mercerized untreated cotton fabrics were also characterized as controls. As shown in Fig. 3.6, a 50% increase of WVTR and WVP was noticed in untreated mercerized cotton fabric as compared to unmercerized fabric, as shown in Fig. 3.6. An increased hygroscopic nature of the mercerized cotton fabric demonstrated WVTR and WVP of 7550 g/m^2.d and 5.96 × 10^{-4} g/m.d.Pa, respectively. Whereas, after PEDOT:PSS coatings (sample GNPs-0%) on the mercerized cotton fabrics, WVTR and WVP factors were decreased by 14%. Similarly, a further reduction in moisture transfer rate was observed when GNPs were mixed with the conductive polymer solution. For instance, the WVTR and WVP values of the sample GNPs-20% were reduced to 5830 g/m^2.d and 4.78 × 10^{-4} g/m.d.Pa, respectively, as shown in Fig. 3.6. Nonetheless, the breathability of the conductive cotton fabric (GNPs-20%) was still in the range of pristine cotton fabrics.

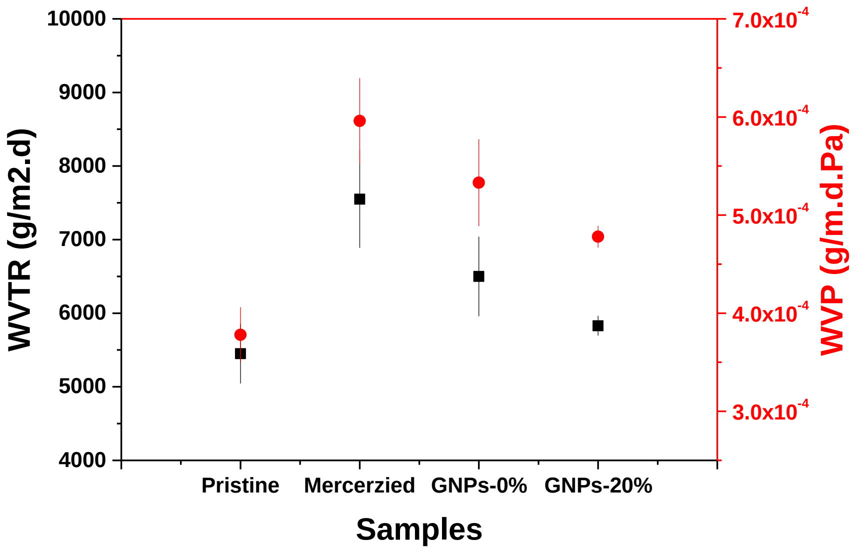

Fig. 3.6. WVTR and WVP of different untreated and conductive cotton fabrics.

3.4.5 Treatment robustness against repeated washing cycles

Change in relative resistance of the best conductive sample GNPs-20% against repeated washing cycles can be seen in Fig. 3.7. After first washing cycle, a large decrease of electrical conductivity is displayed by samples GNPs-20%. Therefore, the R/R_0 ratios was increased from 1.00 to 2.69 corresponding to electrical resistance from 19.4 Ω/cm to 52.3 Ω/cm. After first washing cycle, some micro cracks were appeared on the surface of the conductive fabric (see inset of Fig. 3.7a). Hereafter, once the cracks were formed, the next washing cycles only resulted a small addition to the electrical resistance. For instance, from 2nd to 5th cycle, the electrical resistance of the sample GNPs-20% was increased from 52.3 Ω/cm to 70.2 Ω/cm corresponding to R/R_0 ratio from 2.69 to 3.61, as shown in Fig. 3.7a. The control sample GNPs-0% also exhibited a similar trend of increase in electrical resistance with successive washing cycles (results are not shown here).

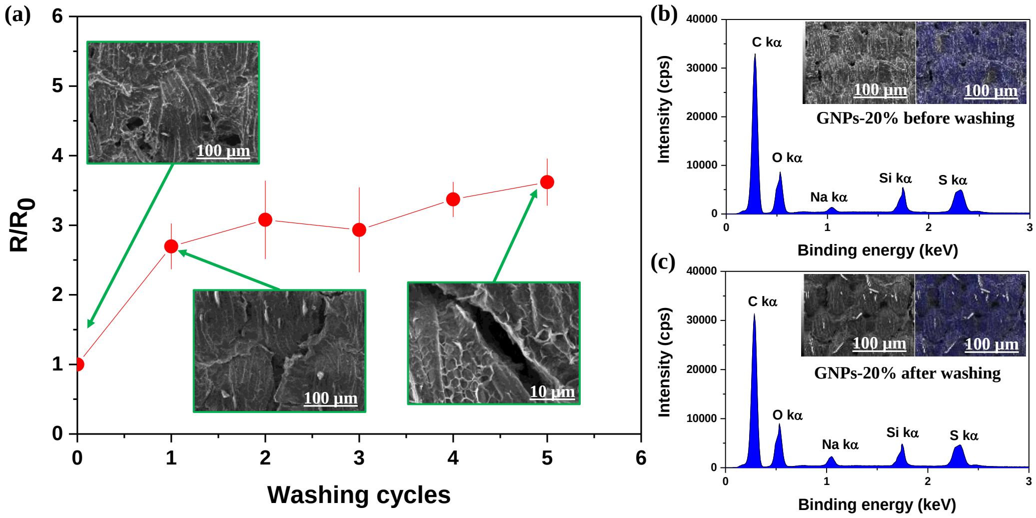

Figure 3.7. (a) Normalized R/R0 electrical resistance of conductive cotton fabric GNPs-20% as a function of number of laundry cycles. Inset images show the crack formation after consecutive laundry cycles. EDX analysis of the sample GNPs-20% (b) before and (c) after 5 laundry cycles. Inset images indicate the mapping (blue dots) of atomic sulphur on conductive fabric surface representing the PEDOT:PSS coating.

After 5 laundry cycles, electrical resistance of the conductive cotton fabric GNPs-20% was increased by more than three folds. However, the magnitude of the sheet resistance was still less than 100 Ω/□. In order to visualize the effect of washing cycles on surface composition, sample GNPs-20% before and after 5 washings was inspected with SEM and EDX. Fig. 3.7b and 3.7c compares EDX signals of the fabrics (sample GNPs-20%) before and after 5 washing cycles, respectively. The data is the average of EDX spectra collected at 10 different locations at the samples. The EDX spectra collected before and after 5th washing cycle didn’t show any remarkable decreased in intensities (~5 %). This negligible alteration of surface composition indicates that GNPs embedded polymer matrix remained intact to the fiber surface during strong agitation and simulated wear abrasion.

3.4.6 Electrical properties

Pure cotton textile is an insulator material with sheet resistance exceeding 10^8-10^9 Ω/sq. Although, pure PEDOT:PSS polymer films exhibit very low sheet resistance of 10-80 Ω/sq. depending on film thickness[84], sheet resistance of conductive fabrics coated with only PEDOT:PSS (GNPs-0%) solutions displayed sheet resistances around 1.5 k Ω/sq., as shown in Fig. 3.8a. This could be attributed to a number of factors, such as absorbing nature of the cotton fibers, porosity within the textile network or substrate dependent preferential orientation of the side chains[180,186]. Substrate induced effects are known to modify and often lower the conductivity of polythiophenes by disrupting the thiophene (in this case PEDOT) side chain orientations attached to the PSS backbone that are responsible for charge transportation[187].

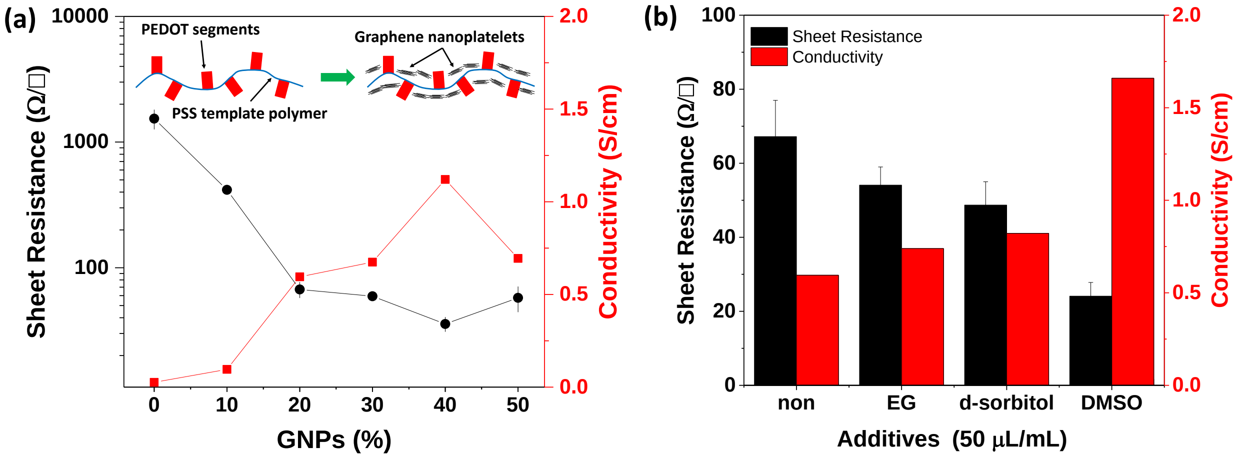

Figure 3.8. (a) Sheet resistance and electrical conductivity of the conductive cotton fabric with increasing mass percentage of GNPs in coating solutions. The inset illustrates "zipping effect " of conductive polymer on incorporated GNPs. (b) Effect of different polar solvents on the sheet resistance and conductivity of the sample GNPs-20%.

Fig. 3.8a shows a nonlinear decline in sheet resistance (corresponding increase in electrical conductivity) of the coated fabrics as a function of incorporated GNPs concentration. For instance, the sheet resistance of the GNP-10% fabric is 332 Ω/sq., a value 4 times lower than the pure PEDOT:PSS treated fabric. Further addition of GNPs in the PEDOT:PSS solution causes a significant improvement in electrical conductivity, as shown in Fig. 3.8a. For instance, at 20 wt.% mass fraction of GNPs (Sample GNPs-20%) the electrical conductivity was increased to 0.6 S/cm at

58 Ω/sq. As discussed above, at this mass fraction, continuous networks of GNPs embedded in PEDOT:PSS polymer matrix were established (see Fig. 3.2d). Hence, the so-called "zipping effect" by PEDOT:PSS polymer chains on dispersed GNPs segments can occur, enhancing the charge transport between adjacent PEDOT sites (see in set of Fig. 3.8a)[188,189]. It is worth noting that mercerization slightly increased the sheet resistance after treatment with GNPs containing solutions compared to a similar treatment applied to the as-received fabrics (see appendix-I, Fig. S6). This could be associated with the alkaline neutralization of sulfonic acid group in PSS segments acting as primary dopants[90]. Nonetheless, compared to the mechanical properties of unmercerized conductive fabrics, an insignificant increase in sheet resistance followed by good final mechanical properties is highly preferred (GNPs-20% is about 58 Ω/sq.). Although higher GNPs concentrations yielded sheet resistance values close to 20 Ω/sq., the resultant fabrics displayed very poor wear and abrasion resistance, as well as laundry cycle durability along with touch and feel perception. Therefore, the GNPs-20% fabric was used for further strain sensing experimentation.

There are, however, potential possibilities to reduce sheet resistance further without using higher GNP concentration. We implemented the well-known secondary dopant concept (developed for pure PEDOT:PSS films) which can be introduced as "co-solvent" in conducting polymer-GNP solutions[187]. A number of organic solvents have been extensively studied for this purpose in pure PEDOT:PSS films, such as EG, d-sorbitol or DMSO[91]. Hence, new GNPs-20% fabrics were made by mixing these co-solvents at 50 µL/mL ratio before spraying. As shown in Fig. 3.8b, the sheet resistance was further reduced to 24 Ω/sq., particularly when DMSO was used, with a very stable Ohmic current-voltage behaviour. The DMSO improved the charge transportation by inducing phase separation in PEDOT and PSS segments[190–192] and it had the same effect in the presence of GNPs. The use of DMSO has not influenced the mechanical properties and the physical appearance of the conductive fabrics.

3.4.7 Cyclic strain sensitivity

Certain textile based conductive materials demonstrate reversible strain sensitivity or response in the form of reversible changes in electrical resistance under cyclic deformation[87]. The GNPs-20% fabric made with the DMSO co-solvent was tested for this purpose. A strip of 10 × 4 mm^2 fabric was elongated to 5% and 10% maximum stretch levels at a constant strain rate of 5 mm/min along the fabric axis. Fig. 3.9a shows the cyclic stretch-release response of the fabric under 5% (blue) and 10% (green) maximum strain in terms of normalized resistance change. In both cases, an initial increase in the normalized resistance takes place within the first five cycles, as shown in Fig. 3.9b. This can be attributed to a partial disentanglement of GNP-GNP contacts also observed on other conducting fabrics[193]. Subsequently, the oscillations in the resistance remain stable and reproducible, as shown in Fig. 3.9c. It is worth noting that the calculated gauge factors 4.45 and 4.80 for 5% (ε=0.05) and 10% (ε=0.1) strains, respectively, are higher than those of metallic foils under similar strains[87]. Wu *et. al.* (2005) also observed a similar behaviour (gauge factor, GF ~5) for polypyrrole coated nylon/lycra fabrics[194].

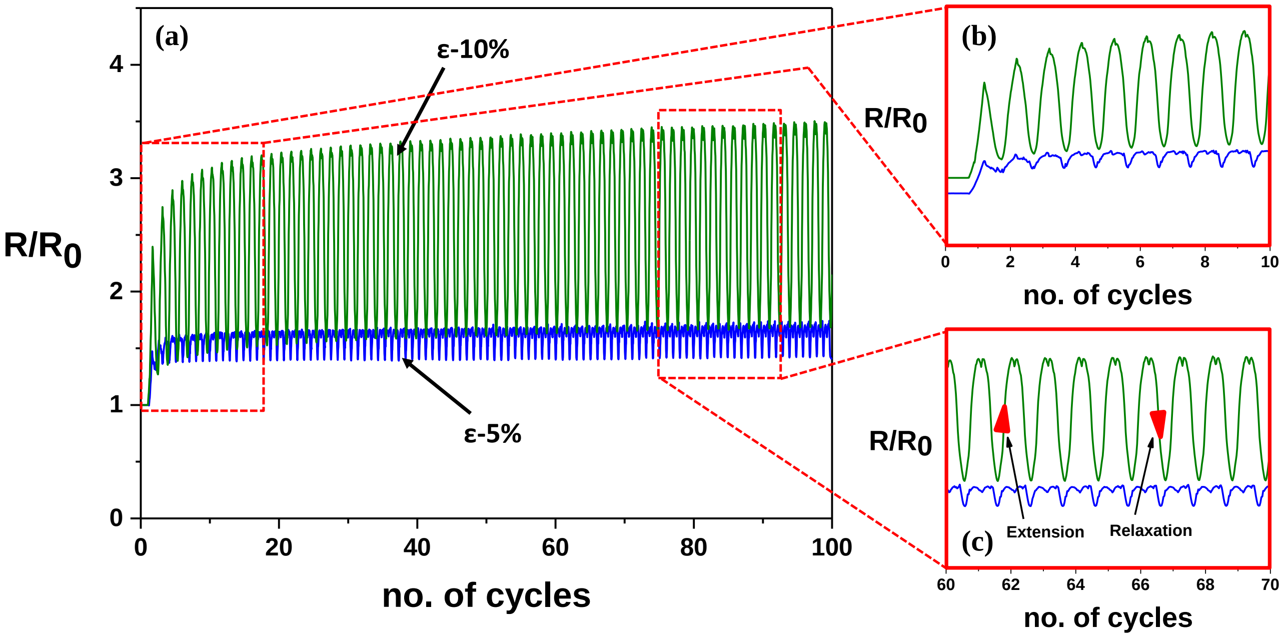

Fig. 3.9. (a) Normalized resistance ratio R/R_0 at 5% (blue line) and 10% (green line) deformations of the sample GNPs-20%. (b) Increase of R/R_0 ratio in initial 5 cycles and (c) continuous strain-sensing behaviour of conductive sample GNPs-20% during extension and relaxation modes. Both modes are indicated with red arrowheads. Overlapped deformation curves are slightly shifted in (b) and (c) for better understanding.

A closer look at the oscillating normalized resistance signals in Fig 3.9c, reveals that at the end of a single stretch event and as the fabric starts to relax, a dent-like R/R_0 response occurs. This behaviour is ascribed to instant re-establishment of certain “interfibrillar contacts” along the woven fibre texture[80,87]. This event is further followed by establishment of full “interfibrillar contacts” upon release or relaxation as well as recovery of electrical contacts along individual fibre surfaces (intra-fibre contacts)[194], resulting in a sharp decline in normalized resistance. The strain response of the GNPs-20% fabric was stable for even more than 1000 cycles (see appendix-I, Fig. S7).

Finally, we investigated the strain recovery behaviour of the GNPs-20% fabric after cessation of the cyclic strain-release tests. In the case of 100 cycles at 5% strain, the conductive fabric normalized resistance decreases to ~1.16 in less than 15 sec. after cessation (see Fig. 3.10a), while it stabilizes at 1.12 after 6-7 minutes. This corresponds to a 90% recovery. However, as shown in Fig. 3.10b, after the cessation of 100 cycles at 10% strain, the immediate recovery within the first 15 seconds does not take place and instead the fabric's viscoelastic recovery stabilizes at a normalized resistance of 1.6, after 40 minutes. This translates into ~60% recovery. This indicates that substantial residual stresses still remain in the fabric one hour after cessation; however a normalized 1.6 resistance value is not substantial and does not correspond to an order of magnitude decrease in conductivity of the fabric. A review of literature indicates that different woven textiles demonstrate diverse viscoelastic recovery behaviour within an hour of termination of strain cycles under 10% deformation, for instance, cotton, nylon and lycra recover by 61%, 91% and 100% of their original dimensions, respectively[87]. Although not shown, within the course of 24 hours, further viscoelastic relaxation occurs and up to 83% of the initial resistance is recovered in this case (10% strain). Similarly, about 95% of the initial resistance is recovered in the case of 5% maximum strain. Note that other conductive fabrics containing more GNPs demonstrated poorer recovery performance and are not reported herein for brevity. Hence, the conductive cotton fabric GNPs-20% appears to be a highly promising smart textile for flexible wearable interconnections or strain sensing applications.

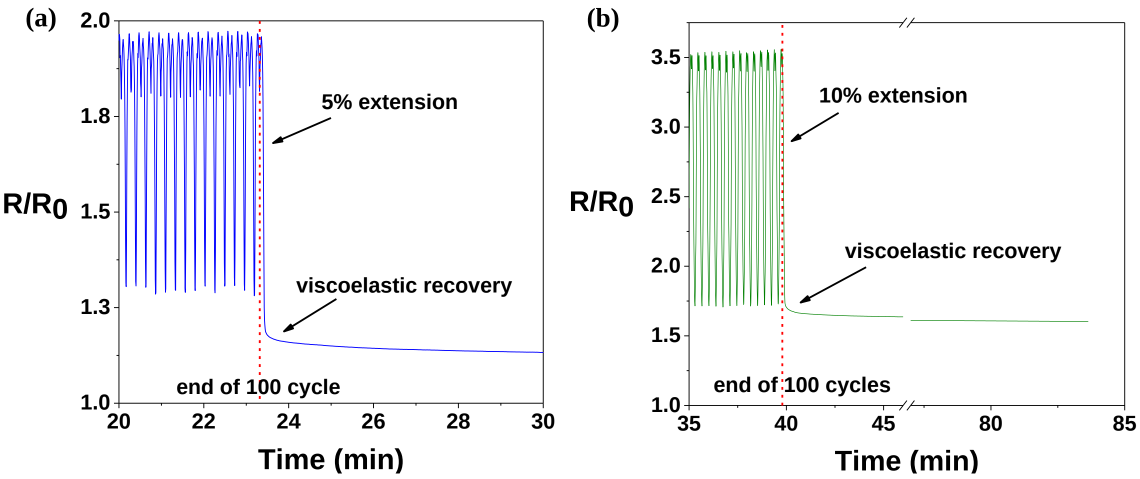

Fig. 3.10. Viscoelastic recovery of initial resistance in (a) 5% deformed and (b) 10% deformed conductive cotton fabric (sample GNPs-20%) after 100 cycles.

3.4.8 Resistance to Severe Repetitive folding-unfolding tests

Although many conductive polymer or conductive polymer composite films function when flexed[195], a realistic performance indicator for foldable conductors is the degree of increase in resistance when they are completely bent or folded over themselves under substantial pressing force[67]. In other words, under conditions such that pressing hard over the fold line causes permanent fold marks similar to paper origami. The process is depicted in the photographs shown in Figs. 3.11a-3.11c. The fabric was folded over itself (180°) and a 0.5 kg weight was placed and kept over the fold line for 1 min. Subsequently, the weight was removed, the fabric was unfolded and the resistance was measured across the fold line (a single fold-unfold cycle). After each folding-unfolding cycle, the average normalized resistance R/R_0 value (R_0 is initial electrical resistance/cm) is recorded as a function of the cycles shown in Fig. 3.11d.

After the first two cycles (Fig. 3.11d), the normalized resistance jumps to about 1.2, followed by an increase to about 1.7 over the course of 20 cycles. This is rather encouraging in terms of folding-unfolding fatigue as the deterioration in resistance does not even double. Note that increasing the folding-unfolding cycles beyond 20 does not cause further worsening of the fabric resistance (not shown in the graph). Although, such fatigue tests are rare in literature, very recently both Cai *et al.* (2017)[67] and Cataldi *et. al.* (2017)[175] have also reported experiments with repeated folding-unfolding cycles on conductive textiles. For comparison purposes, their findings have also been plotted in the Fig. 3.11d. More specifically, Cai *et. al.* observed a small change of electrical resistance with 180° folding-unfolding cycles even though the conductive fabric was not subjected to any pressing weight. However, in the case of Cataldi *et. al.*, due large pressing weight (5 kg), the degradation in resistance was more prominent at the end of 10 cycles. During repetitive folding-unfolding with pressing weight, formation of micro-cracks along the fold line was confirmed by electron microscopy as shown in Figs. 3.11e and 3.11f. However, there existed many other interconnecting sections over the fold line discontinuity sufficient for electrical conductivity as shown in Fig. 3.11f (see upper left corner). As seen above, the prepared conductive fabrics have good resistance to mechanical deformation, washing cycles and bending induced fatigue. This aspect is an important requirement for functional sportswear.

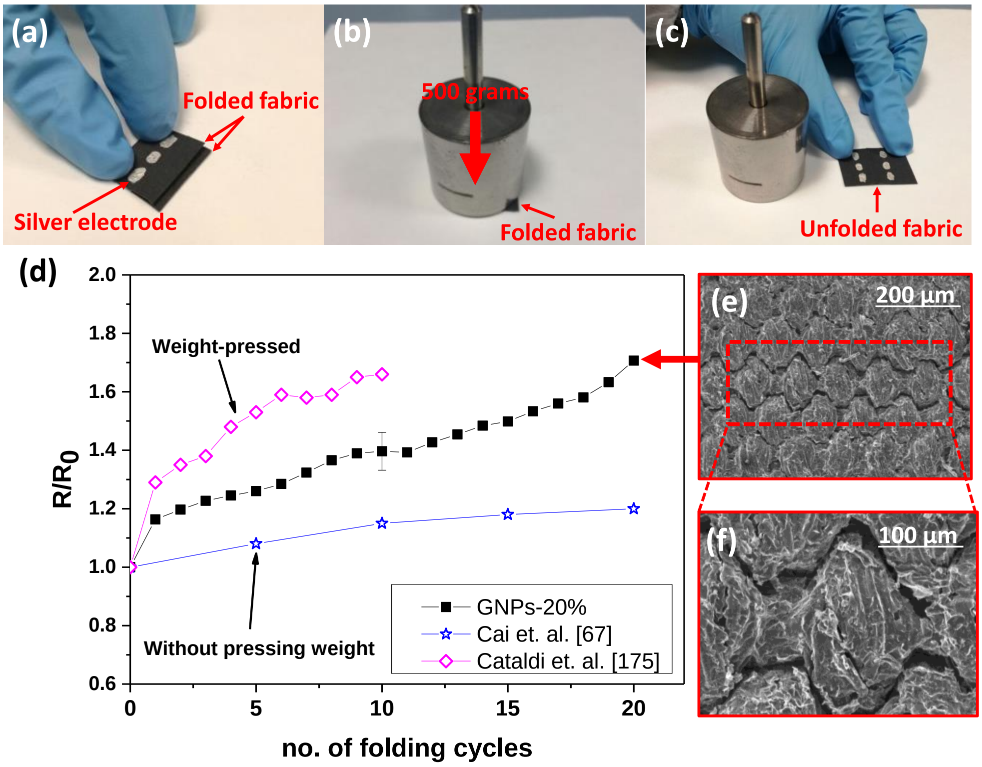

Fig. 3.11. (a-c) 180° folding-unfolding mechanism with pressing weight. (d) normalized R/R_0 measurement of weight pressed 180° folding-unfolding test as a function of number of folding cycles. (e-f) formation of structural crack along the folded line. Representative error bar indicates measurement uncertainty level.

3.4.9 Capacitance measurements

Conductive cotton fabrics with lowest sheet resistance were also tested for their electrochemical performance. For this, parallel plate supercapacitors were prepared in the coin cell configuration using GNPs-30% treated fabric as shown in Fig. 3.12a. A commercially available tetraethylammonium tetrafluoroborate (TEABF4) in acetonitrile was used as solid state electrolyte separator. The porous fabric structure was advantageous here to have more surface area and easy access to active materials such as GNPs and PEDOT:PSS[65]. The prepared coin cells of GNPs-30% conductive fabrics were mounted in the battery unit and tested for 1000 cycles. Fig. 3.12b shows galvanostatic measurements of the prepared supercapacitor at different current densities. At low current density of 0.3 mA/cm^2, the supercapacitor with GNPs-30% treated fabric demonstrates high charging and discharging times corresponding to small slope of the discharging curves. On the other hand, with high current densities, this charging-discharging times are reduced and slope of the discharging curves increase respectively. Capacitance (Farads, F) of the prepared supercapacitors are calculated using following equations,

$$C(F) = \frac{1}{slope\ of\ discharge\ curve} \tag{3.5}$$

$$C_{sp} = 4 \times \left(\frac{C(F)}{mass\ in\ grams}\right) \tag{3.6}$$

Where, C_{sp} is the specific capacitance with units F/g. Using these equations, the resultant specific capacitance measurements are shown in Fig. 3.12c. For instance, the prepared supercapacitor shows 62 F/g and 39 F/g values of C_{sp} correspond to current densities of 0.125 mA/cm^2 and 1.56 mA/cm^2, respectively. An ideal supercapacitor with no redox reaction and zero capacity loss demonstrates a prefect square shaped curves in cyclic voltammetry measurements[196]. However, in reality some faradaic losses occur and the tested supercapacitors show oxidation and reduction peaks during cyclic voltammetry measurement as in the work of Yun *et al.*[197]. In our measurement, the resulted voltammetry curves were not deformed corresponding to no redox reactions and minimum capacity losses. This indicates the characteristics of a supercapacitor[198].

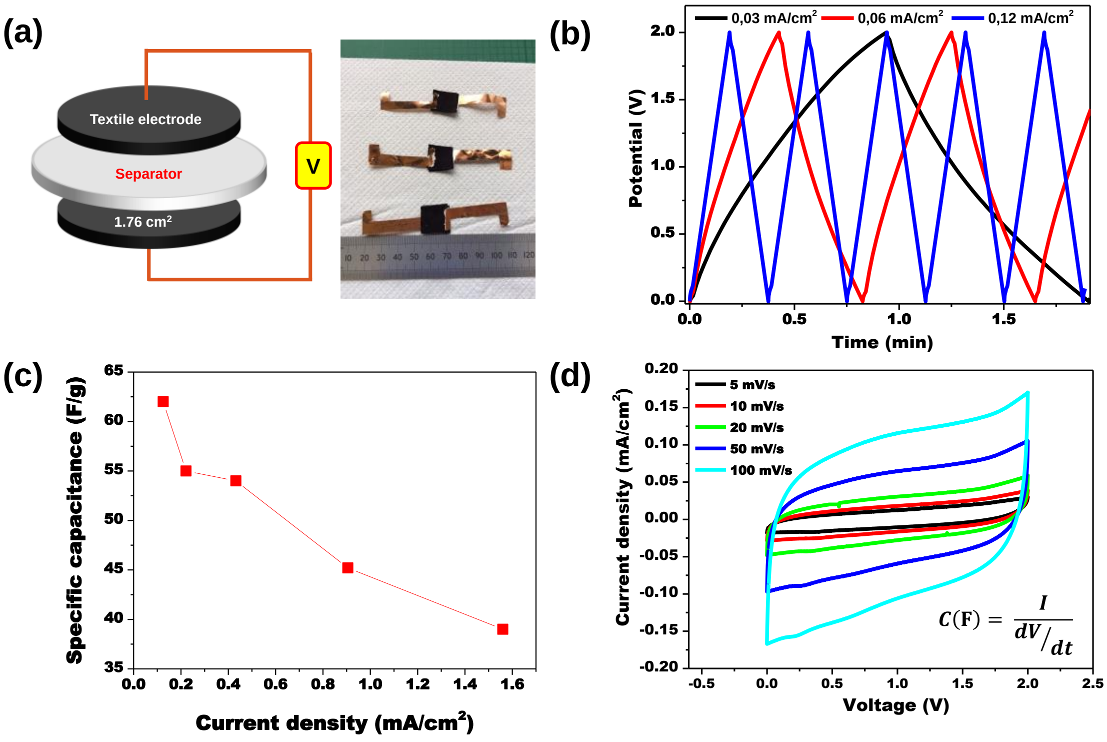

Fig. 3.12. (a) Coin cell configuration. Attachment of the copper electrodes to mount in battery unit also have been shown. (b) charge-discharge test (c) specific capacitance of the supercapacitor as a function of current density. (d) cyclic voltammetry measurements.

3.5 Conclusion

Mercerized woven cotton fabrics were successfully modified by conductive polymer PEDOT:PSS and graphene nanoflake dispersions (20 wt.% GNPs) to impart electrical conductivity. A simple spray coating technique was used for this purpose. Conducting fabrics were breathable, light weight and resistant to laundry cycles. After secondary doping by DMSO co-solvent, a sheet resistance and electrical conductivity of ~25 Ω/□ and 1.6 S/cm were achieved, respectively. Conducting mercerized fabrics were found to respond to cyclic strain deformation at 5% and 10% strain rates for up to 1000 cycles with ~90% viscoelastic recovery levels after cessation of the cycles. Additionally, the fabrics demonstrated strong resistance against fatigue due to repeated folding-unfolding events under pressing weight. These useful features are important for real time strain-sensing devices. Moreover, the conducting fabrics may also be suitable for applications in wearable electronics, energy storage as supercapacitors, data storage and transmission and biomedical monitoring.

Chapter: 4

Mn-Doped TiO_2 Nanoparticles for Antibacterial and Self-Cleaning Fabrics

4.1 Introduction

Recent advances in the nanotechnology and fabrication techniques have made it quite simple to functionalize conventional textile fabrics (cotton, polyester, silk) for their technical applications[1,8]. Particularly, antibacterial and self-cleaning properties of the functionalized fabrics have gained more attention due to rise in health and safety awareness. Nanotechnologies also have footprints in this field of high interest for medical, sports, and uniform applications. For instance, metallic (silver, gold, copper) based nanoparticles are considered as core elements for antibacterial properties. However, as mentioned earlier, their corrosive nature, costs of production, environmental instability and cytotoxicity hamper their usage in functional textiles at industrial scale productions[103,105]. Alternatively, ceramic based nano-materials, such as, zinc oxide (ZnO) and titanium dioxide (TiO_2) nanoparticles are increasingly adopted for photocatalytic antibacterial fabrics[8]. These photocatalytic nanoparticles are attributed to have no toxicity, low production cost, high stability and degradation of several organic compounds in addition to antibacterial properties[103,107]. Another advantage of ZnO and TiO_2 NPs is their photocatalytic performance under both UV and visible irradiations, however, for visible activity a doping elements is required[108]. Therefore, these photocatalytic nanoparticles with low cost and non-toxicity have huge potential for textile applications

4.2 Objectives

The main objective of this chapter is to impart another very important functional aspect to the conventional textiles. In this chapter, multifunctional cotton fabrics have been demonstrated using low cost, non-toxic manganese doped TiO_2 nanoparticles (TiO_2:Mn NPs) blended with polydimethylsiloxane (PDMS) binder. High photocatalytic potential of the TiO_2:Mn NPs has been exploited in cotton fabrics to render them antibacterial and self-cleaning. Further, their applications for water purification also have been studied. Textile fabric properties, such as, tensile strength and breathability are also analysed after TiO_2:Mn NPs and PDMS treatment. Washing resistance of the treated fabrics is tested against 10 washing cycles.

4.3 Materials and methods

4.3.1 Materials

Plain woven, bleached, 100% cotton fabric with 180 ± 5 g/m^2 mass density was purchased from Swissatest Testmaterialien AG (Switzerland). The fabric was uniformly constructed in both directions (warp and weft) having thread size and density of 36 Tex and 24 threads/cm, respectively. Low cost TiO_2:Mn NPs were prepared by sol-gel method using titanium (IV) oxysulfate ($TiOSO_4 x H_2O$) as precursor. Preparation details and TiO_2:Mn NPs characterizations are given elsewhere [patent GR20090100724][199]. Shortly, anatase TiO_2:Mn NPs were characterized to 20-30 nm particle size, 24 m^2/g surface area and band gap of 2.75 eV corresponding to 0.1 wt.% Mn doping. A single component polydimethylsiloxane (PDMS, Elastosil E43) was purchased from Wacker Chemie AG (Germany). As per manufacturer, the moisture cured PDMS forms a quick, transparent skin on the surface when applied and have good mechanical flexibility and self-levelling properties. Ethyl acetate and MB model dye (Sigma Aldrich) were used as received. Milli-Q distilled water was used for the MB solutions.

4.3.2 Textile treatment

Cotton fabrics (10 × 10 cm^2 sample size) were treated by a simple spray coating technique. First, the PDMS solution was prepared in ethyl acetate and then and TiO_2:Mn NPs were blended with PDMS solution at different mass fractions, PDMS/TiO_2:Mn NPs-100/0 (namely NPs0), 90/10 (NPs10), 75/25 (NPs25) and 50/50 (NPs50), keeping the total solid content of 1 wt.% in the solutions.

Subsequently, the prepared solutions were bath sonicated for 8 hours at 59 kHz and 135 W (Savatec, Italy). For each TiO_2:Mn NPs mass fraction, 15 mL of solution was sprayed onto each side of the fabric, using an airbrush spray system (VL Siphon feed, 0.73 mm nozzle, Paasche airbrush, US). During spray coating, the nozzle to fabric distance and spray pressure were maintained at 15 cm and 2.5 bar, respectively. Spraying cycles were followed by drying the fabric using a hot air gun, keeping a dry pick-up of 6 % - 7 % w.r.t. pristine fabric weight, corresponding to mass loading of 1.00 – 1.26 mg/cm^2. Coated fabrics were then allowed to crosslink at room temperature for 24 hours, at 65% humidity prior to characterization.

4.3.3 Characterization

4.3.3.1 Surface morphology

Morphological characterizations were performed by Scanning Electron Microscopy (SEM, JEOL-6490AL,Japan). Where necessary, high-resolution SEM imaging was carried out using a JEOL JSM 7500FA (Japan) equipped with a cold field emission gun (FEG), operating at 5 kV acceleration voltage. Energy dispersive X-ray (EDX) analysis was also performed for certain samples in order to quantify the loss of material in washing tests.

4.3.3.2 Attenuated Total Reflection-Fourier Transform Infrared (ATR-FTIR) Spectroscopy

Infrared spectra of different samples were obtained with a FTIR spectrometer (Equinox 70 FT-IR, Bruker, Germany) equipped with an ATR accessory (MIRacle ATR, PIKE Technologies). All spectra were recorded in the range from 4000 to 600 cm^{-1} with 4 cm^{-1} resolution, accumulating 128 scans. To ensure the reproducibility of obtained spectra, five samples of each type were measured.

4.3.3.3 Raman Spectroscopy

μRaman spectroscopy (Renishaw Invia, United Kingdom) with 514 nm laser excitation line through a 100× objective lens (numerical aperture 0.75) was used to excite the specimens, at low power of 0.4 mW. The spectral region scanned was 3500–100 cm^{-1} with a spectral resolution of approximately 1 cm^{-1}. All the spectra were normalized to their maximum.

4.3.3.4 Mechanical characterization

Mechanical properties were measured with an Instron dual column tabletop universal testing System 3365 (USA) at 5 mm/min^{-1} strain rate. The tensile measurements were conducted on five different specimens for each sample according to ASTM D3505 standard test methods. Young’s moduli (slope of the curves before rupture point) were extracted from engineering stress-strain curves and reported with standard deviations.

4.3.3.5 Moisture permeability or breathability

Breathability of the prepared cotton fabrics was measured by water vapor permeability (WVP) technique, using metallic permeation cells. The WVP of fabrics was determined at 25 °C and under 100% relative humidity gradient (ΔRH%) according to the ASTM E96 standard method. 450 μL of distilled water (which generates 100% RH inside the permeation cell) was placed in each test permeation cell with a 7 mm inner diameter and a 10 mm inner depth. Fabrics were cut into circles and mounted on the top of the permeation cells. The permeation cells were placed in 0% RH desiccator with anhydrous silica gel (Sigma Aldrich) used as a desiccant agent. The water transferred through the fabric pores was determined from the weight change of the permeation cell every hour during the first 8 h using an electronic balance (0.0001 g accuracy). The weight loss of the permeation cells was plotted as a function of time. The slope of each line was calculated by linear fitting. Then, the water vapour transfer rate (WVTR) was determined as below[170,171],

$$WVTR\ (g(m^2d)^{-1} = \frac{Slope}{area\ of\ the\ fabric} \tag{4.1}$$

WVTR measurements were replicated three times for each fabric sample and the average WVP of the fabrics were calculated as follows;

$$WVP\ (g(md\ Pa)^{-1} = \frac{WTVR \times l \times 100}{\rho_S \times \Delta RH} \tag{4.2}$$

where l (m) is the fabric thickness, measured with a micrometer with 0.001 mm accuracy, ΔRH (%) is the percentage relative humidity gradient, and p_s (Pa) is the saturation water vapor pressure at 25 °C (3168 Pa).

4.3.3.6 Washing fastness assessment

In order to assess washing durability, the fabric specimens were washed in a capped bottle containing 500 mL distilled water and 0.37 % w/w of a neutral washing detergent (pH ~7.0), under constant stirring. Two samples with same TiO_2:Mn NPs mass fractions were washed simultaneously in the same bottle in order to replicate the fabric to fabric wear abrasion. Total 10 washing cycles were used and during each cycle, washing solutions were heated at 50 ± 2 °C for 30 min. Afterwards, the samples were rinsed, dried and conditioned at relative humidity of 65 ± 2% and temperature of 23 ± 1 °C for 24 h.

4.3.3.7 Antibacterial test

The quantitative antibacterial efficiency of the treated fabrics was determined against *Klebsiella pneumoniae* as a gram-negative bacterium according to the AATCC 100-2004 test method. For this, fabric samples (d = 5 cm) were impregnated with 1 mL of *k. pneumoniae* serum (10^5 CFU/mL concentration) and incubated at 37 °C for 18 h before sunlight irradiations. The percentage reduction (R %) of bacterium population was calculated by following equation,

$$R\ \% = \frac{n_f - n_i}{n_i} \times 100 \tag{4.3}$$

Where n_i and n_f are initial and final bacteria populations. Herein, the reduction percentage less than 50 % represents almost zero, between 50% and 90 % a significant and above 90 % as a strong antibacterial efficacy[200]. Bacterial inactivation kinetic were also assessed using Chick-Watson models[201].

Although PDMS/NPs coated fabrics are generally hydrophobic, water droplets after prolonged contact can spread out on the surface and impregnate the PDMS/NPs coated fabrics with time [202], as demonstrated chapter 2 (see also appendix-I, Fig. S1). Test samples were also impregnated by similar method using *k. pneumoniae* serum. For antibacterial performance, only *k. pneumoniae* bacteria was used intentionally because it is the most versatile human pathogen responsible for nosocomial infections[203]. They are more fatal to persons with weakened immune system and alcohol addiction.

4.3.3.8 Photocatalytic degradation of MB under UV and visible irradiations

Degradation of MB treated fabrics was assessed using two different methods under both UV and visible irradiations; 1) degradation of MB dye on dry stained fabrics and 2) degradation of MB dye in solutions with treated fabrics immersed into them.

In the first method, treated cotton fabrics (3 × 3 cm^2 sample size) were immersed into 50 mL MB solution at concentration of 20 mg/L[204,205] and were left overnight in the dark to achieve adsorption-desorption equilibrium. Then, the samples were dried and conditioned at 23°C and 65% relative humidity for 24 h in a dark chamber. The estimated amount of adsorbed MB dye was ca. 5.0 mg/g on the fabric surface. Subsequently, the MB stained fabrics were irradiated with visible light (LUXEON Rebel ES 7LEDs with coolbase, operated at 18 V and 0.25 A) at 10 cm fabric to lamp distance. The irradiation chamber was isolated from the external environment. The concentration of residual MB dye (C) on the fabric's surface was determined by UV-vis spectrophotometry (Varian Carry 6000i, US) in the range of 500-800 nm, using an integrated sphere, since MB has an absorption peak at λ_{max} = 664 nm[99,206], the intensity of which decreases with the degradation of MB. The discolouration of the irradiated samples, then, was calculated by removing the fabric sample from the irradiation chamber at regular intervals of 1 h and measure the residual concentration of the MB dye at 664 nm until the absorption was close to zero. The photocatalytic degradation kinetics were determined by the relative concentration C/C_0, where C_0 is the initial concentration of MB dye and C is the residual amount of MB dye at different experimental times. For comparison, a similar procedure was also repeated under UV irradiation (Bromograph LUX UV lamp, Leonex, Italy) with 354 nm main wavelength.

For the second method, treated cotton fabrics (3×3 cm^2) were immersed into 50 mL solutions overnight under dark conditions to achieve adsorption-desorption equilibrium. Subsequently, the MB dye solutions containing the fabric samples were irradiated with visible light and the residual concentration of the MB dye (C) in each solution was determined by UV-vis absorption intensity at λ=664 nm. To observe the residual concentration of MB dye, 3 mL solution was taken out at regular intervals of 1 h.

4.4 Result and discussion

4.4.1 Surface morphology

Fig. 4.1 shows SEM images of pristine and coated cotton fabrics with different mass fractions of TiO_2:Mn NPs. As seen in Fig. 4.1a, the pristine fabric is composed of a network of round cellulosic (cotton) fibres with some uneven microfibrillar structures (due to wear abrasion during manufacturing). In contrast, the sample NPs0 demonstrates very smooth and conformal coating of polymer on its surface, as shown in Fig. 4.1b, with PDMS encapsulating each fibre. In the case of embedded NPs, TiO_2:Mn NPs start to appear on the surfaces. As seen in Fig. 4.1c, the surface of the sample NPs25 has an even distribution of NPs on individual fibers. However, at this NP loading, some fibres still do not reach optimum coverage and fibre fragments remain uncovered (as indicated by arrows in Fig. 4.1c).

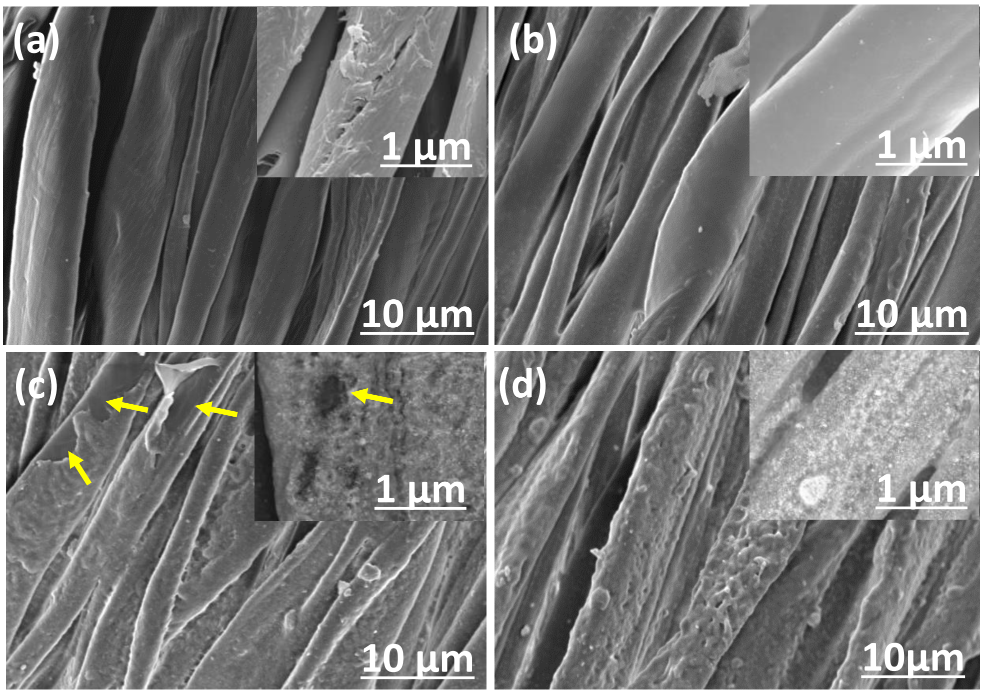

Figure 4.1. SEM images of (a) untreated cotton fabric, (b) sample NPs0, (c) sample NPs25 (uncovered zones are indicated) and (d) sample NPs50. Higher resolution SEM images (insets) are also provided with corresponding NPs mass fractions for better understating.

Complete fibre coverage is attained at a mass loading of approximately 50 wt.%, as seen in Figure 4.1d. Some agglomeration of the nanoparticles are formed on the treated surface without, however, changing the physical properties of the treated textiles (inset of Fig. 4.1d). It is important to note that polymer dispersions do not alter the overall porosity of the treated fabrics, as shown by breathability tests in section 4.4.3.

4.4.2 Chemical characterization

FTIR was performed in order to chemically characterize the functional textiles, as shown in Fig. 4.2a. Pristine cotton fabric shows well-known bands associated with pure cellulose, namely, OH stretching at 3364 cm^{-1}, CH stretching at 2891 cm^{-1}, adsorbed water at 1645 cm^{-1}, ring breathing at 1157 cm^{-1} and C-O stretching at 1026 cm^{-1}[144]. Sample NPs0 with PDMS coating shows distinct IR peaks associated with PDMS polymer at 2964 cm^{-1}, 1261 cm^{-1} and 799 cm^{-1} for stretching, bending and rocking modes of CH_3 groups, respectively[139]. Stretching band attributed to Ti-O-Ti vibrations is also present at 846 cm^{-1} in sample NPs50[207].

In the case of sample NPs50, a shift of approximately 12 wavenumbers is seen in the CH_3 rocking band at 799 cm^{-1} after curing, as shown in Fig. 4.2b. This shift is due to the change in the distance of Si-O bonds due to the formation of hydrogen-bonds between OH groups of the cellulose and the ether group of PDMS, as depicted in inset of Fig. 4.2b. A comparable shift of 10-12 cm^{-1} was also recorded in PDMS and starch system or when PDMS was cured on the cotton fabric[139,202]. This strong binding of PDMS to cotton fibres is essential to keep intact the polymer coating with the embedded NPs on the fibre’s surface, during washing and wear abrasions.

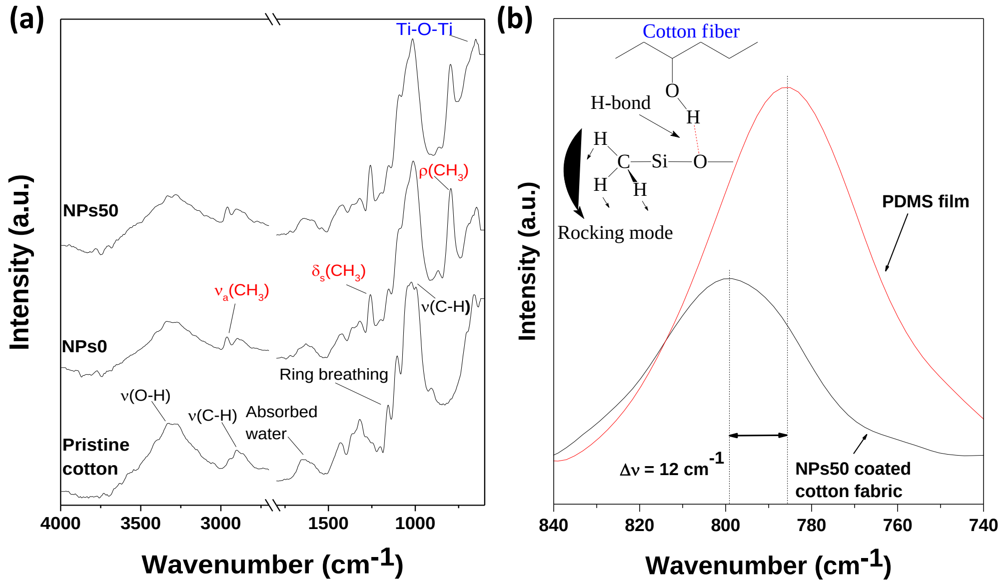

Figure 4.2. Chemical characterization. (a) ATR-FTIR spectra of cotton substrates with different coating formulations. Assignments for cellulose (black), PMDS (red) and TiO_2 nanoparticles (blue) are included. (b) CH_3 rocking absorption of pure PDMS film and PDMS finished cotton fabric (sample NPs50). The rocking mode of PDMS methyl groups is shown in in-set.

Fig. 4.3 shows the Raman spectra of untreated and treated sample. Pristine cotton fabric shows an intense peak at 2897 cm^{-1} attributed to CH and CH_2 stretching in cellulose macromolecules (Fig. S5, see in appendix-I) and several other peaks between 300 cm^{-1} and 1500 cm^{-1}. CH_2 and C–C vibrations associated to cellulose ring breathing are visible at 1370, 1152 and 1095 cm^{-1}. In addition, the vibrational contributions of glycosidic bond symmetric stretching and ring deformation are detected at 1120, 969, 519 cm^{-1} and 435, 379 343 cm^{-1}, respectively. Finally, the vibrations at 1480 and 1460 cm^{-1} are assigned to the crystalline and amorphous structure of the cellulose, respectively[208].

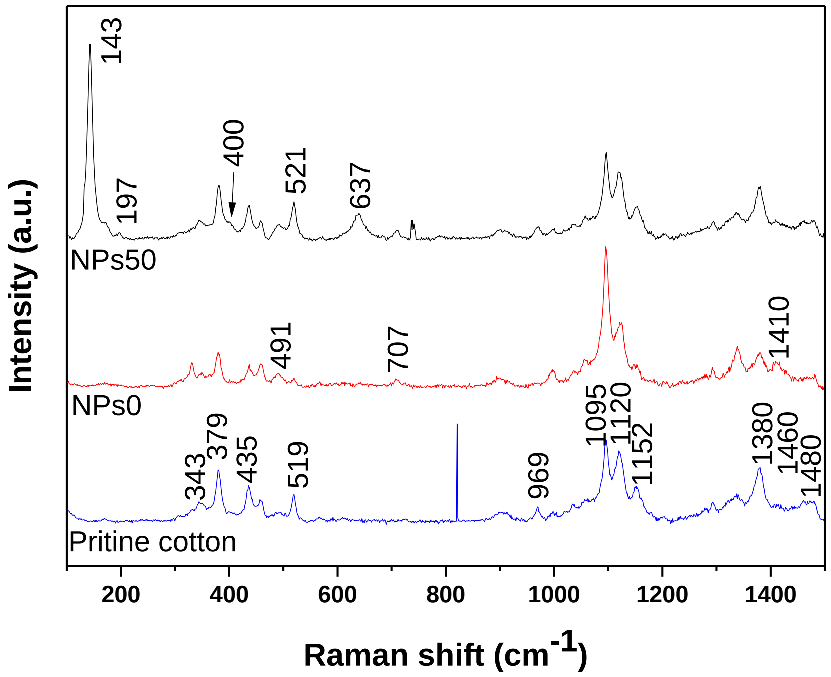

Figure 4.3. Raman spectra of pristine cotton fabric, sample NPs0 and sample NPs50. Corresponding peak are identified for each sample type.

Sample NPs0 shows additional characteristics peaks associated to PDMS in the collected Raman spectra, as shown in Fig. 4.3. Symmetric stretching vibrations of Si-O-Si, Si-C and bending mode of CH_3 group were detected at 491 cm^{-1}, 707 cm^{-1} and 1410 cm^{-1}, respectively[209]. In sample NPs50, TiO_2 NPs show peaks at 143, 406, 517 and 639 cm^{-1}, associated with anatase TiO_2 phase[121].

4.4.3 Breathability

For breathability, WVTR and WVP of untreated and Mn:TiO_2 NPs treated fabrics were compared. As shown in Fig. 4.4, a comparison of WVTR (black) and WVP (red) is given for the respective samples. Highly hygroscopic cotton fabric demonstrates WVTR and WVP of 5160 g/m^2.d and 3.58 $\times 10^{-4}$ g/m.d.Pa, respectively. After functional coatings, a minor descending trend in moisture transfer rate and permeability are noticed in PDMS coated fabrics with increasing NPs mass fractions, as shown in Fig. 4.4. For instance, WVTR and WVP of sample NPs50 are reduced to 4840 g/m^2.d and 3.36 g/m^2.d, respectively. Nonetheless, the change in WVTR and WVP is not more than 6% for all NPs mass fractions as compared to untreated cotton fabric, as shown in Fig. 4.4.

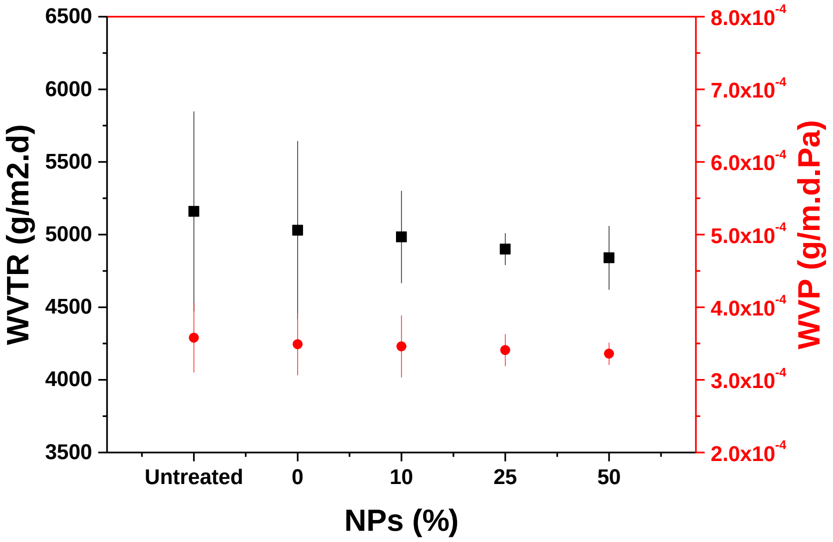

Figure 4.4. WVTR and WVP of untreated and different treated fabrics.

4.4.4 Stress-strain properties

Fig. 4.5a demonstrates typical J-shaped stress-strain curves for pristine and treated cotton fabrics[202]. The treated fabrics follow the similar mechanical behaviour as that of untreated fabric, however, increasing mass fraction of NPs in the coating solutions resulted a small increase in fabric elongation of ca. 4%, as seen in Figure 4.5a. In particular, sample NPs50 displays highest value of elongation at break of 31%, as shown in Fig. 4.5b. Fig. 4.5b summarizes Young's modulus for all treated fabrics. Unlike elongation at break, Young's modulus of the all treated fabrics are decreased by 10%-18%, depending on the mass fractions of TiO_2:Mn NPs. For instance, Young's modulus of the sample NPs50 with 50 wt.% nanoparticle is reduced to 302 MPa from 337 MPa as that of pristine fabric. This minor reduction of 10% is acceptable in functional textiles[46] and can be attributed to the presence of a very fine coating of highly elastic PDMS on the surface. Here, it is worth noting that the mechanical characteristics of PDMS/TiO_2:Mn NPs finished cotton fabrics have not altered significantly with respect to the original untreated fabric.

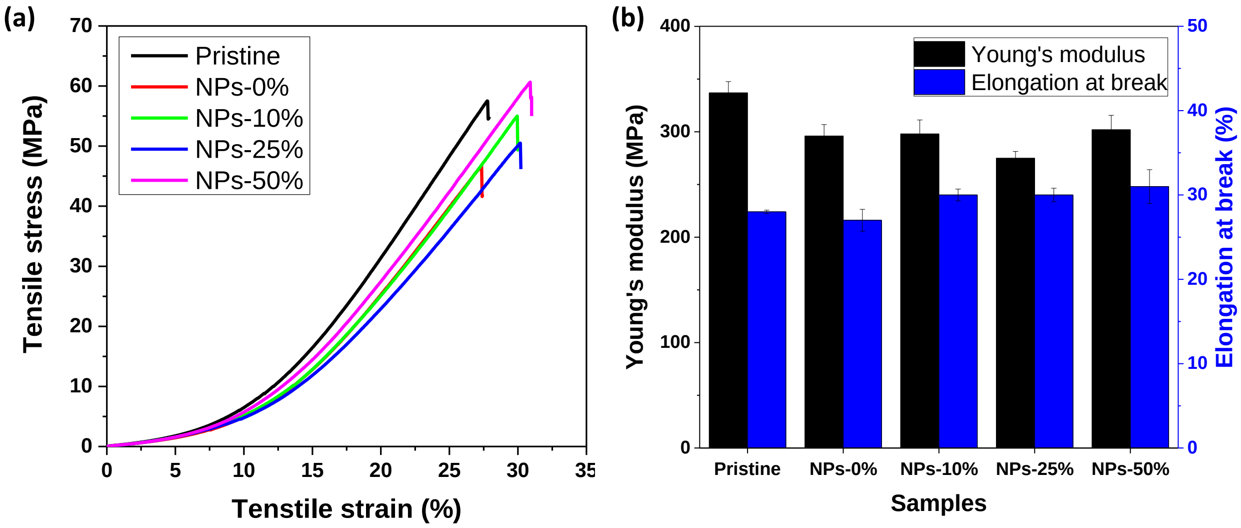

Figure 4.5. (a) Stress-strain curves of pristine and different treated cotton fabrics (NPs0, NPs10, NPs25 and NPs50). (b) Young's modulus (MPa) and maximum elongation at break (%) of respective fabrics.

4.4.5 Washing fastness

Antibacterial and self-cleaning textiles treated with functional materials don't undergo washing processes frequently, however when subjected to such processes should retain their functional features. Here, the selected sample NPs50 was subjected to a normal washing process repeated 10 times and then characterized for its surface compositions by EDX spectroscopy before and after the process. As shown in Fig. 4.6a, sample NPs50 before washing demonstrates a peak at 1.74 keV for silicon signals from PDMS[202]. An additional peak at 4.48 keV comes from the Ti element from TiO_2 nanoparticles. The inset of Fig. 4.6a shows equal distribution of Si (green) and Ti (red) signals on the surface of treated cotton fabric. After 10 successive washing cycles, EDX spectra of sample NPs50 (hereafter referred as NPs50W) exhibited similar pattern and distribution of Si and Ti signals as shown in Fig. 4.6b. However, an insignificant decrease of 7.50 % in Si signals and 15.85 % increase of Ti signals was recorded as compared to unwashed fabric. This minor change in surface composition can be attributed to wear abrasion of the fabric's surface during the washing process. As the sample NPs50 was washed with another similar fabric simultaneously, this could have removed some of the protective PDMS coating, exposing more NPs on the surface. Nevertheless, the TiO_2:Mn NPs embedded in PDMS conformal coatings remained intact and demonstrated equal self-cleaning and antibacterial properties, as will be discussed next.

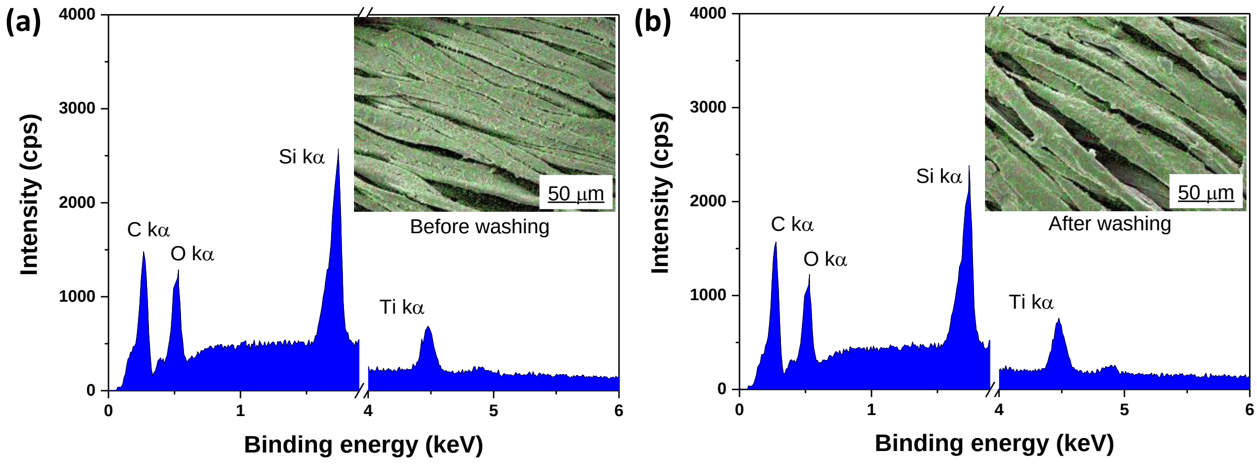

Figure 4.6. EDX analysis of antibacterial cotton fabric (a) before and (b) after 10 washing cycles. In-set images shows surface composition of the applied antibacterial coatings indicating presence of Silicon (green) and Titanium (red) elements. (Au signals are not shown here).

4.4.6 Antibacterial properties

Antibacterial properties of TiO_2:Mn NPs coated cotton fabrics were evaluated through bacterial reduction test against *k. pneumoniae* and results are shown in Fig. 4.7. All treated fabrics did not show any antibacterial activity under dark as no photocatalytic reaction occurs in the absence of light, however, when challenged under sunlight exhibit significant reduction in bacterial populations. Only sample NPs0 without incorporated nanoparticles shows a negligible antibacterial activity, as shown in Fig. 4.7. Sample NPs0 reaches 50% and 75.4% bacterial reductions after 60 m and 120 m of sunlight exposure, respectively. This small reduction in bacterial count can be attributed to sunlight which, depending on the intensity, can inactivate a very small percentage of the bacterial population. In contrast, the other samples with incorporated TiO_2:Mn NPs have a substantial reduction in the bacterial populations. As shown in Fig. 4.7, sample NPs10 with 10 wt.% of TiO_2:Mn NPs demonstrates relatively less reduction percentage within first 60 m as compared to samples NPs25 and NPs50. As such, sample NPs10 reduces 46.4% bacteria count, whereas, sample NPs25 and NPs50 demonstrate 79.2 % reductions after 60 m. After 120 m of sunlight exposure, all treated samples with TiO_2:Mn NPs reach up to 0 CFU/mL indicating a 100 % bacterial reduction, as shown in Fig. 4.7. Herein, the incorporated TiO_2:Mn NPs upon exposure to sunlight leads to the production of oxidative radicals ($OH^\bullet$), which in turn cause oxidative stress in bacteria, perforation of the cell membrane, elimination of intracellular components and ultimately cell death[210,211]. It is important to note that sample NPs50W (after 10 washing cycles) also demonstrates similar antibacterial kinetics and reaches 96.8% bacterial reduction after 120 m. Antibacterial test results of sample NPs50W endures our explanation about cellulose-PDMS interaction and washing robustness.

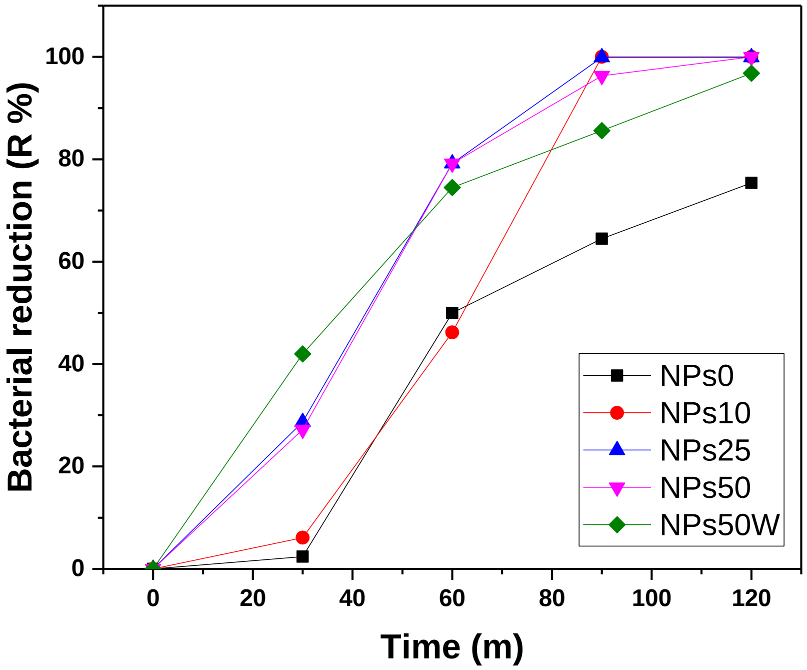

Figure 4.7. Bacterial reduction (%) of different treated sample under natural sunlight.

The inactivation kinetics of *k. pneumoniae* were also performed under sunlight with aforementioned experimental conditions. After 120 m, decrease in *k. pneumoniae* counts have been plotted against exposure time, as shown in Fig. S8 (see in appendix-I). The bacterial inactivation kinetic (K) are measured according to Chick-Watson equation as follow[201],

$$\frac{dN}{dt} = KC \tag{4.4}$$

$$ln\frac{N}{N_0} = -KCt \tag{4.5}$$

where N is the number of CFU per milliliter of solution at the time t, N_0 is the initial number of CFU per milliliter of solution at the beginning of the test, C is the concentration of applied TiO_2:Mn NPs. A linear regression fitting was used to estimate the correlation between experimental data and the models used here. The results of inactivation kinetic K (min^{-1}) and goodness of regression fitting (R^2) are shown in table 4.1. From the kinetic table 4.1, sample NPs25 shows slightly fast antibacterial reaction with 0.06 min^{-1} value of K as compared to sample NPs50 with inactivation kinetics of 0.05 min^{-1}. Practically, both samples show first order of reaction kinetics and can be regarded as efficient antibacterial materials. However, sample NPs50 have higher value of regression coefficient (R^2 = 0.80) as compared to sample NPs25 (R^2 = 0.71), see table 4.1. This higher value of regression coefficient for sample NPs50 indicates a good correlation between the Chick-Watson model and the experimental data indicating highly reproducible experimental results.

Table 4.1. Rate constants (K) and linear regression fit (R^2) of *k. pneumoniae* inactivation kinetics.

Sample	K (min^{-1})	R^2
NPs0 (no Mn:TiO_2 NPs)	0.01	0.93
NPs10	0.02	0.79
NPs25	0.06	0.71
NPs50	0.05	0.80
NPs50W (washed)	0.03	0.95

4.4.7 Photocatalytic degradation of MB

Fig. 4.8 shows self-cleaning and water purification properties of the samples NPs25, NPs50 and NPs50W under visible irradiations. The control sample NPs0 is also studied for comparison. Fig. 4.8a shows rate of degradation of MB adsorbed on textile surface under visible light. Herein, sample NPs0 in the absence of photocatalytic NPs does not show any reduction in the concentration of MB, whereas, sample NPs25 with 25 wt.% TiO_2:Mn NPs demonstrate a noticeable change in concentration of the adsorbed MB. As such, after 4 h of visible irradiations relative concentration is changed from 1.00 to 0.63 indicating 37% reduction and reaches to 75% at the end of 10 h. On the other hand, samples NPs50 and NPs50W demonstrate significant reductions (almost 100%) within the equal time. Fig. 4.8a and 4.8b show that relative concentrations and MB absorptions (at 664 nm) of the samples NPs50 and NPs50W decrease with irradiation time and reach 53% and 48% after first 4 h, respectively. After 6 more h of visible light exposure, sample NPs50 exhibit 100% reduction in the absorption of MB on its surface, whereas, sample NPs50W could only reduce 96% MB, see Fig. 4.8a and 4.8b.h. In both cases, the adsorbed MB dye on the surface of the samples was completely decomposed to CO_2 and H_2O by photocatalytic action of TiO_2:Mn NPs[111], and the fabric samples become as white as they were before, for example see sample NPs50 in Fig. 4.8c.

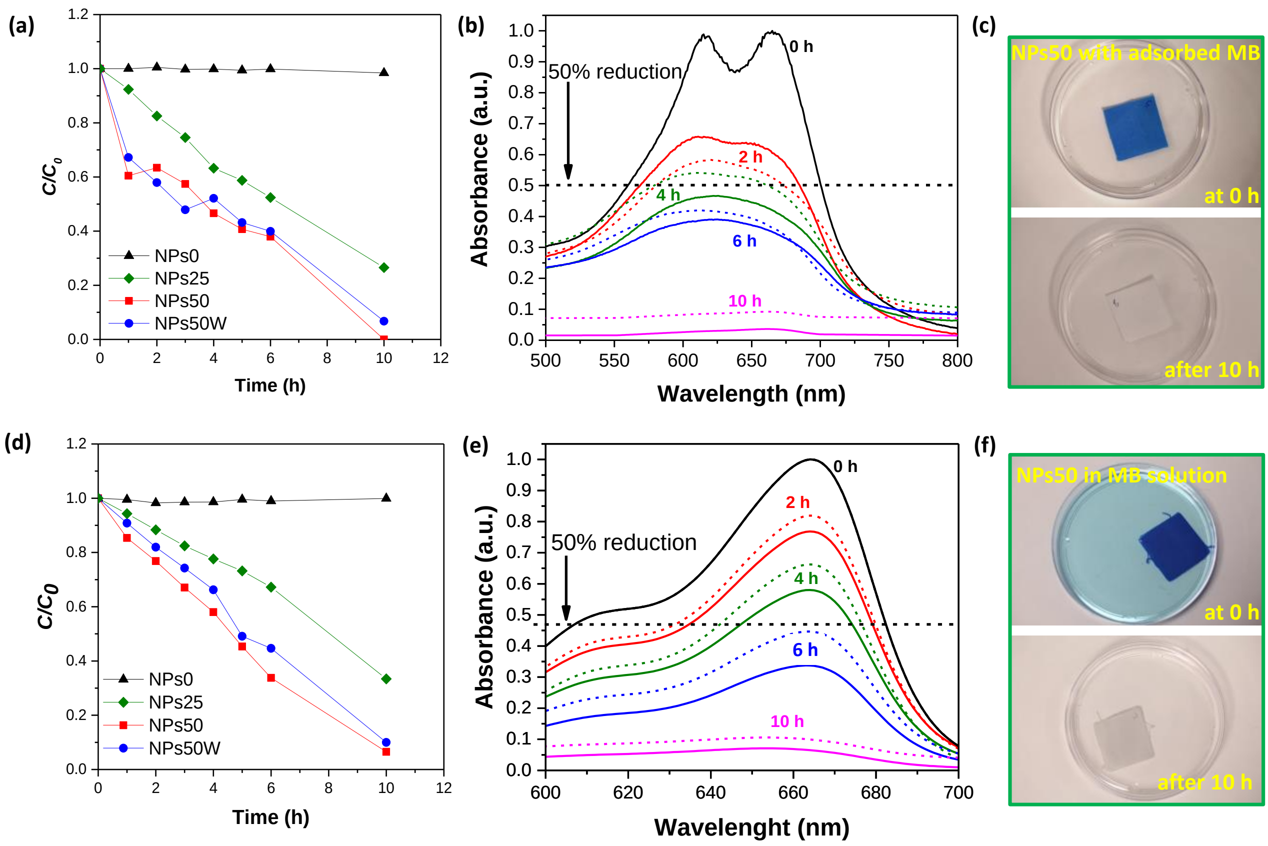

Figure 4.8. Rate of degradation or change in relative concentrations (*C/C_0*) of MB dye (a) adsorbed on dry samples and (d) dissolved in solutions with treated samples immersed into them, as a function of irradiation time. (b) Normalized UV-Vis absorption spectra of MB dye from sample NPs50 (solid lines) and sample NPs50W (dotted lines) at different irradiation times (b) on dry fabrics and (e) in solution forms. An indication of 50 % reduction in MB absorption have been provided. (c) Self-cleaning and (f) water purification with sample NPs50 after 10 h of visible irradiation.

Likewise degradation of MB stains, test samples NPs0, NPs25, NPs50 and NPs50W also exhibit similar degradation kinetics of MB dye in solution forms replicating a water purification effect. For this, the test samples were immersed into 50 mL MB dye solutions separately and irradiated with visible light. Fig. 4.8d show degradation kinetics of MB into solutions with samples NPs0, NPs25, NPs50 and NPs50W, respectively. As in the self-cleaning test, sample NPs0 did not show any degradation of MB dye in solution under visible light, whereas, samples NPs25, NPs50 and NPs50W demonstrates similar degradation patterns, see Fig. 4.8d. Sample NPs25 exhibits 67% reduction of MB in the solution after 10 h. Meanwhile, sample NPs50 and NPs50W are able to reduce more than 90% of MB dye in aqueous solutions, as shown in Fig. 4.8d and 4.8e. Interestingly, besides complete discolouring of the MB solution, the sample NPs50 and NPs50W also degrade the adsorbed MB dye on their surfaces replicating a self-cleaning effect, as can be seen in Fig. 4.8d (sample NPs50). Samples NPs25, NPs50 and NPs50W also displayed equivalent self-cleaning and water purification effect under UV irradiations as shown in Fig. S9 and Fig. S10 (see in appendix-I). The rate of degradation under UV irradiation was slightly higher than under visible irradiation. This enhanced photocatalytic activity of the TiO_2:Mn NPs is attributed to higher photo energy of UV light and is in accordance with previous studies of doped TiO2 NPs, either on textiles[121,206], or water purification[99,212].

The repeatability of the self-cleaning and water purification process was also tested and sample NPs50 was subjected to 3 complete MB degradation cycles. As shown in Fig. 4.9, the TiO_2:Mn NPs functionalized cotton fabric (sample NPs50) exhibited highly maintainable photocatalytic activity for 3 cycles under visible light. It is worth noting that, in subsequent cycles, the process of MB degradation is slightly faster. In other words, it takes less time to degrade 50% MB dye in 2nd cycles as compared to degradation time in the first cycle. This effect is ascribed to removal of possible external impurities present on the surface of tested sample in the first cleaning cycle[99,121].

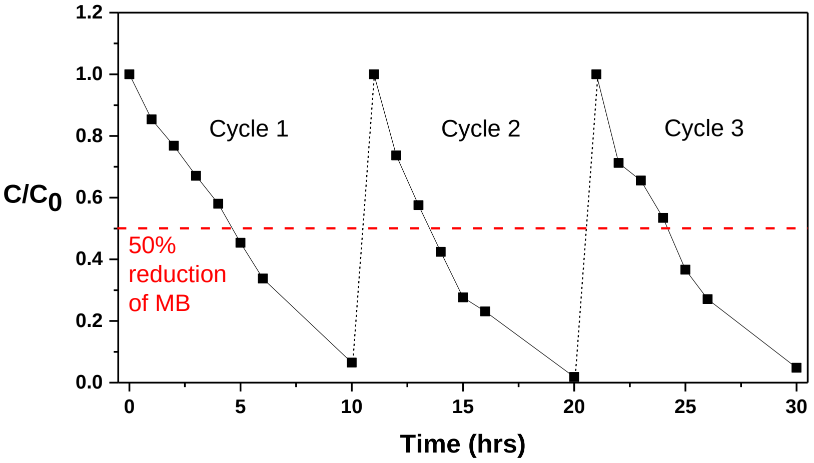

Figure 4.9. Repeatability of sample TiO_2:Mn NPs (sample NPs50) for water purification under visible light. Each sign indicates one hour of irradiation.

4.5 Conclusion

Cotton fabrics were successfully modified using TiO_2:Mn NPs nanoparticles immobilized into PDMS matrix for water de-coloring, self-cleaning and antibacterial properties. Anatase TiO_2:Mn NPs were exploited for their extended feature, such as, visible spectrum photo-activation, low cost (as titanium oxysulfate is used as precursor), environmental stability and non-toxicity. TiO_2:Mn NPs functionalized cotton fabrics demonstrated antibacterial properties and decomposition of MB model dye in aqueous solutions under visible irradiation. Furthermore, the prepared cotton fabrics were also able to self-clean from MB stains under similar conditions. Nevertheless, the applied functional coatings could hardly alter the physical properties of the fabrics, like, mechanical strength, breathability, color and aesthetic. The prepared cotton fabrics also maintained their multifunctional characteristics after several laundry cycles. Convincingly, TiO_2:Mn NPs deposited cotton fabrics have potential for applications in hospital apparel, military uniforms, sports wears and purification of industrial effluents.

Chapter: 5

Thermal interface materials (TIMs) for regenerated cellulose

5.1 Introduction

Thermal interface materials (TIMs) are placed between two contacting surfaces to increase their thermal conductivity (*k*) at the interface. TIMs absorb thermal energy from a hot surface and transfer it to the cold surface, resulting a significant decrease in temperature of the hot surface[213,214]. They are widely implemented in almost every electronic device, such as, mobiles, monitors, LEDs, computers, communication and entertainment equipment, vehicle and aircraft powered components[215,216]. As per Moore's law[217], increase in energy densities drives the requirement of highly efficient TIMs for thermal management. Therefore, a large number of TIMs are commercially available in the form of thermal greases, gels, pads, solders[218,219]. Unlike other materials, thermal pads have excellent physical features, like, reusability, good replaceability, thermal stability, structural integrity and mechanical strength[214,219]. Although, thermal pads are more useful than thermal greases or gels, normally their thermal conductivities remain in the range of ~3 W/mK[214]. This happens because thermal pads are normally particle loaded polymer composites[220], in which thermally conductive nanomaterials (ceramics, carbon, metallic and hybrid fillers) are imbedded into insulating polymer matrices (epoxy, silicon resins, polyurethanes, acrylics). This affects the thermal conductivity of the prepared TIMs and a high mass loading of conductive filler is always required to reach above 5.0 W/mK level. In turn, at high mass loading, mechanical properties are increasingly effected[221].

In the past, different combinations of polymer matrices and nanofillers have been successfully adopted to achieve highly conductive thermal pads. For instance, Ishida et la. reported a ceramic based boron-nitride filled polybenzoxazine thermal pads[222]. The prepared nanocomposites achieved highest thermal conductivity of 32.5 W/mK at 88% filler's mass fraction. A large particle size distribution of boron-nitride particles is attributed to achieve this high thermal conductivity. Whereas, in other studies, this value of *k* remained well below 4 W/mK at 60% mass fractions[221,223,224]. Unlike ceramic counter parts, metallic nanoparticles/wires filled polymer matrices can achieve thermal conductivities of 2 order of magnitudes at very low mass loading. As such, Xu et al. have reported thermal conductivities of 38.5 W/mK and 86 W/mK at 10% and 20% volume fraction of silver nanowires (AgNWs) into polycarbonate films, repectively[225]. Herein, high aspect ratio of metallic nanowires and their intrinsic thermal conductivity displays improved transportation of the thermal energy. Similarly, Wang et al. prepared AgNWs/polyacrylate nanocomposites with 1.10 W/mK thermal conductivity at just 0.9 % volume fraction of AgNWs[226]. Whereas, copper nanowires (CuNWs) produced 2.46 W/mK thermal conductivity at equal volume fractions. Likewise, nickel and gold nanowires also have been demonstrated for thermal pads with high k values at low volume fractions[227,228]. Despite their highly conductive nature, metallic fillers add significant weight, cost, stiffness and wear abrasiveness to the prepared thermal pads. Alternatively, carbon based nanofillers (graphite, graphene, nanotubes) have garnered a considerable attention of the researchers for TIMs applications. They are light weight, non-toxic, thermally stable and have very high intrinsic k values, such as, 1000 W/mK to 3000 W/mK for graphene and multiwall carbon nanotubes (MWCNTs), respectively[229]. Nevertheless, in the composite forms, thermal conductivities largely depends on their mass loadings and type of carbon fillers. Such as, Hong and co-authors have studies the effect of single wall carbon nanotubes (SWCNTs) and MWCNTs on thermal conductivities in polymethyl methacrylate (PMMA) matrix[230]. They observed that, at 4 wt.% mass fraction, values of k were 0.78 W/mK and 3.44 W/mK for SWCNTs and MWCNTs, respectively. On contrary, the nanocomposites prepared with SWCNTs displayed thermal conductivity of 2.43 W/mK at 1 wt.% mass fraction. This negative effect was regarded as poor dispersion of SWCNTs in the polymer matrix at elevated mass fractions. In another work, Jakubenik *et al.* have used SWCNTs to enhance the thermal conductivity of polystyrene films[231]. The prepared composites were reported to have thermal conductivity of 0.25 W/mK at 1 wt.% mass fractions. As mentioned above, depending on their intrinsic value of k, epoxy resins loaded with graphene were characterized to have 5.0 W/mK at 30 wt.% mass fractions[232,233]. Likewise metallic nanowires, high aspect ratio graphene nanoplateslets (GNPs) and carbon nanofibers (CNFs) demonstrate high values of k, for instance, thermal conductivities of 6.44 W/mK for GNPs and 21 W/mK for CNFs have been report previously[234–236]. It is important to note that in thermal pads, synthetic polymer are commonly used as supporting matrices that thermally degrade on elevated temperatures[237]. The thermally degraded polymers leave huge carbon footprints behind. Therefore, it is increasingly emphasized to replace fossil-fuel based plastics with natural bioplastics. In contrast, recently developed regenerated bioplastics with good mechanical and thermal properties[170,237–240] have huge potential to replace synthetic metrics in TIMs applications and have not been reported previously.

5.2 Objectives

In this chapter, a simple and easily scalable process for sustainable TIMs from waste cotton fabrics will be demonstrated. Cellulose based regenerated films are prepared by dissolving cotton fabrics into trifluoroacetic acid (TFA) solutions, mixed with GNPs and then solvent casting. After complete evaporation of TFA, cellulose/GNPs based nanocomposite films have been characterized for their electrical and thermal conductivities. The prepared films also have been investigated for their surface topology, chemical structures and mechanical properties.

5.3 Experimental

5.3.1 Materials

Plain woven, bleached, 100% cotton fabric with 120 ± 5 g/m^2 mass density (Cotoneficio Albini, Italy) was used as model cotton fabric for regenerated cellulose composites. GPNs were donated form DirectaPlus (Italy). Shortly, GNPs are characterized to 21 nm thickness, 340 nm lateral size and more than 8 graphene layers[241]. TFA (Sigma Aldrich) were used as common solvent for dissolving cotton without further purifications. A commercially available thermal pad (ARCTIC) and nanoclay (Sigma Aldrich) were used as a reference materials with thermal conductivities of 6.0 W/mK and 1.0 W/mK[242], respectively .

5.3.2 Sample preparation

Before dissolution, cotton fabrics were washed with normal laundry cycle to remove any possible contaminations. After that, washed and oven dried cotton fabrics were dissolved into TFA solution at concentration of 1 wt.%. It takes 4 to 5 days for complete digestion of cotton fabrics into TFA at room temperature. Hereafter, GNPs were mixed with the solution at mass fractions of 5% to 50% w.r.t. total weight of the prepared nanocomposites on dry basis. The prepared solutions (cellulose/GNPs) were bath sonicated (Savatec, Italy) for 10 h at room temperature.

Subsequently, the prepared solutions were casted and left under aspiration hood for complete evaporation the TFA. A graphical demonstration of the fabrication process have been shown in Fig. 5.1. After complete evaporation, regenerated cellulose/GNPs nanocomposite films were produced with ≈0.500 mm thickness. All nanocomposite films were conditioned at 23 °C and 65 % relative humidity for 24 h before further characterizations.

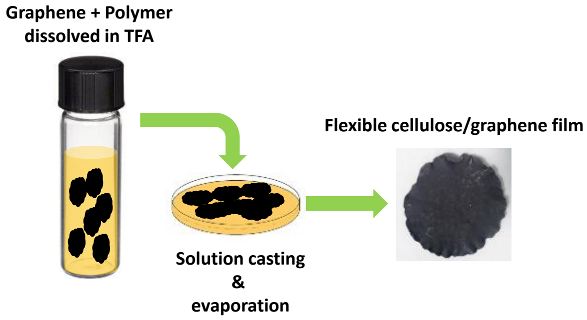

Fig. 5.1. A solution casting route for regenerated cellulose/PPC films

Hereafter, the prepared films are named according to their GNPs mass fractions, for instance, GNPs0% (only regenerated cellulose films) and GNPs25% (containing 25 wt.% GNPs fraction w.r.t total dry weight).

5.3.3 Characterization

5.3.3.1 Electron microscopy

Morphological characterizations were performed by Scanning Electron Microscopy (SEM, JEOL-6490AL,Japan). The sample were frozen dry before SEM analysis to preserve the composite structures. Energy dispersive X-ray (EDX) analysis was also performed for certain samples in order to analyses the TFA residues.

5.3.3.2 Chemical and structural characterization

Infrared spectra of different samples were obtained with a FTIR spectrometer (Equinox 70 FT-IR, Bruker, Germany) equipped with an ATR accessory (MIRacle ATR, PIKE Technologies). All spectra were recorded in the range from 4000 to 600 cm^{-1} with 4 cm^{-1} resolution, accumulating 128 scans. To ensure the reproducibility of obtained spectra, five samples of each type were measured.

The prepared cellulose/GNPs nanocomposites were further characterized using μRaman spectroscopy (Renishaw Invia, United Kingdom). 514 nm laser excitation line through a 100x objective lens (numerical aperture 0.75) was used to excite the specimens, at low power of 0.4 mW. The spectral region scanned was 3500–400 cm^{-1} with a spectral resolution of approximately 1 cm^{-1}. All the spectra were normalized to their maximum.

The crystallinity of the nanocomposites was analyzed by X-ray diffraction (XRD) using a diffractometer Rigaku SmartLab X-Ray Diffractometer equipped with a copper rotating anode. The X-ray source was operated at 40 kV and 150 mA. A Gobel mirror was used to obtain a parallel beam and to suppress Cu K radiation (1.392 Å). The measurements were performed using a 2θ scan.

5.3.3.3 Mechanical strength

Mechanical characteristics of the cellulose/GNPs nanocomposites were measured with an Instron dual column table top universal testing System 3365 (USA) at 5 mm/min^{-1} strain rate. The tensile measurements were conducted on five different specimens for each sample according to ASTM

D3505 standard test methods. Young's moduli (slope of the curves before yield point) were extracted from engineering stress-strain curves and reported with standard deviations.

5.3.3.4 Electrical conductivity

Electrical properties of the prepared samples were measured by using Signatone 1160 probe station (Microworld, France). A Keithley 2612A sourcemeter (Tektronix, Inc. US) was used to record voltage-current curves during measurements. Square samples of 5 × 5 mm^2 sheet area were prepared and fixed by double stick adhesive tape onto glass slides. Silver paint (RS silver conductive paint, resistivity ≈ 0.001 Ω/cm) electrodes of 5.0 × 2.5 mm^2 size were painted on the conductive surfaces 5 mm apart (see supporting information Fig. S2) in order to minimize contact resistances between the probes and the fabrics. An electrical voltage of 2.0 V was applied on contacts. The bulk resistance of the samples was calculated by taking the slope of the recorded V-I curves. Three samples for each GNPs mass percentage were measured and average values are reported with standard deviations.. The sheet resistance (Ω/□ or Ω/sq.) was calculated by using the formula:

$$\mathrm{R}_s = \rho \, \frac{\mathrm{L}}{\mathrm{W} \cdot t} \tag{5.1}$$

where, R_s is sheet resistance, ρ is specific resistivity of the bulk, L is length, W is width and t is thickness of the prepared films. Since our measurements were performed at a square fabric area (W=L), and the thickness was kept constant, the value of sheet resistance becomes dependent only on the specific resistivity ($R_s \propto \rho$). The bulk conductivity was calculated by inversing specific resistivity.

5.3.3.5 Thermal properties

Thermal properties of the cellulose/GNPs nanocomposites and two reference materials (commercial and clay film) are characterized by placing them between two carbon steel plates (size 4 cm × 4 cm × 1 cm). The bottom plate was directly in contact with a hot plate at temperature 90 °C, whereas, top plate was at room temperature replicating a real time application in electronics, as shown in Fig. 5.2. A pressing force of 3.5 kg corresponding to 2.15 kPa pressure was used during all measurements.

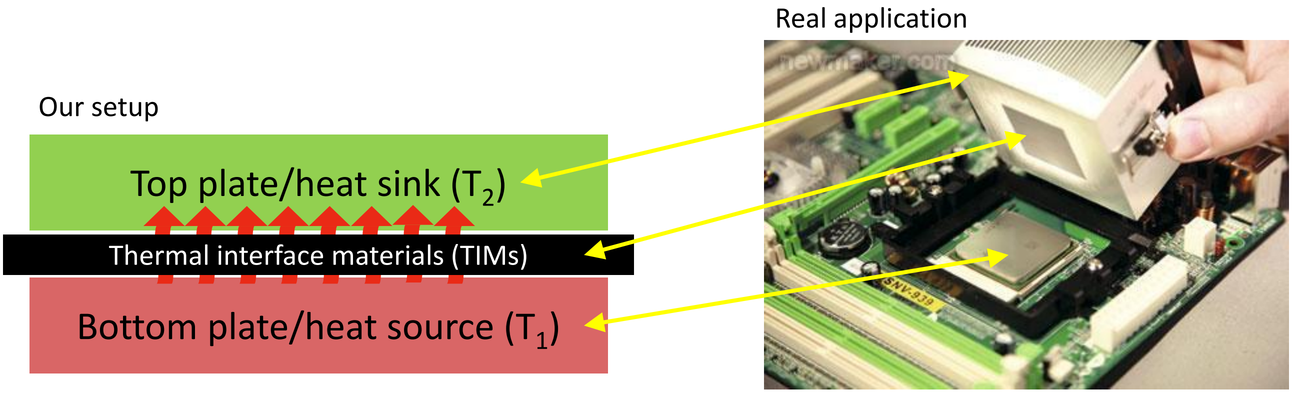

Fig. 5.2. A schematic diagram of thermal conductivity setup, replicating a real application in electronics.

After placing the prepared TIM in between the two plates, as shown above, decrease in temperature of the bottom (hot) plate and increase in temperature of the top (cold) plate were recoded as a function of contact time using an infrared (IR) camera (315 FLIR, UK). The relative changes in temperature of the two plates were also recorded by Thermocouple (ThorLabs, US) and were in agreements with IR camera measurements. Temperature difference (ΔT) has been calculated using following equation,

$$\Delta \mathrm{T} = \mathrm{T}_1 - \mathrm{T}_2 \qquad (5.2)$$

Where T_1 and T_2 are average temperatures of the bottom and top plates near interface, respectively. This change of temperature (ΔT) with time (t) will be used to estimated thermal conductivity of the prepared nanocomposites according to the reference materials.

5.4 Result and discussion

5.4.1 Surface morphology

Fig. 5.3 shows SEM images of the prepared samples, namely, GNPs0%, GNPs10%, GNPs20% and GNPs25%. The pristine film without GNPs (sample GNPs0%) demonstrates a flat surface, as such, no large pores and cracks are appeared in the top and cross-sectional views as shown in Figs. 5.3a and 5.3b. In contrast, when GNPs are mixed with the polymer matrix, GNPs equally disperse throughout the nanocomposite structure. However at low mass fractions, as in sample GNPs10%, GNPs clusters are present at distance from each other and are not well interconnected as seen in Fig. 5.3c and 5.3d. These interconnected GNP-GNP junctions are very crucial for in-plane and out of plane electrical and thermal conductivities. Finally, these GNP-GNP networks are achieved at 20 wt.% mass loading of nanofillers. Fig. 5.3e and 5.3f show surface and sectional views of sample GNPs20% with 3D networking of the incorporated fillers, respectively. Similarly, at 25 wt.%

addition of GNPs (sample GNPs25%) the surface appears to be more enriched with GNPs networks (see Fig. 5.3g), whereas, cross section is not changed significantly. Further additions of the nanofillers above 25 wt.% did not show any noticeable change in morphology and other properties, as will be discussed next.

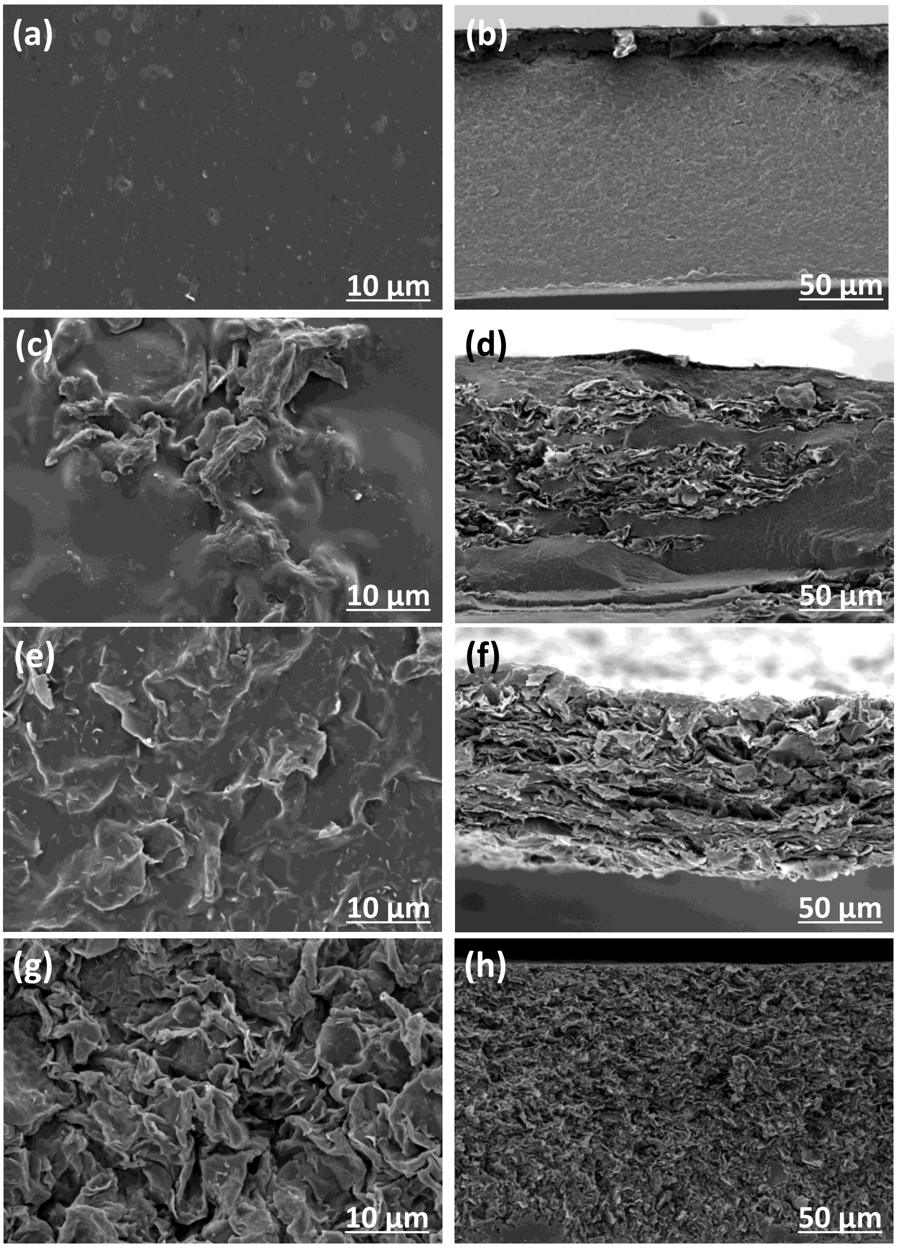

Fig. 5.3. Surface and cross sectional SEM images of samples GNPs0% with pure regenearated cellulose film (a-b), GNPs10% (c-d), GNPs20% (e-f) and GNPs25% (g-h).

Elemental analysis of the prepared sample GNPs0% (see Fig. 5.4) exhibits two distinct peaks at 0.277 keV and 0.530 keV representing oxygen and carbon atoms, respectively[243]. The colour mapping in Fig. 5.4 demonstrates equal distributions of carbon (red dots) and oxygen (blue dots) throughout the surface and cross section. An additional peak at 2.12 keV in EDX spectra is attributed to the gold sputtering. It is worth noting that the EDX analysis did not show any peak at 0.677 keV corresponding to fluorine, indicating a TFA free nanocomposite films.

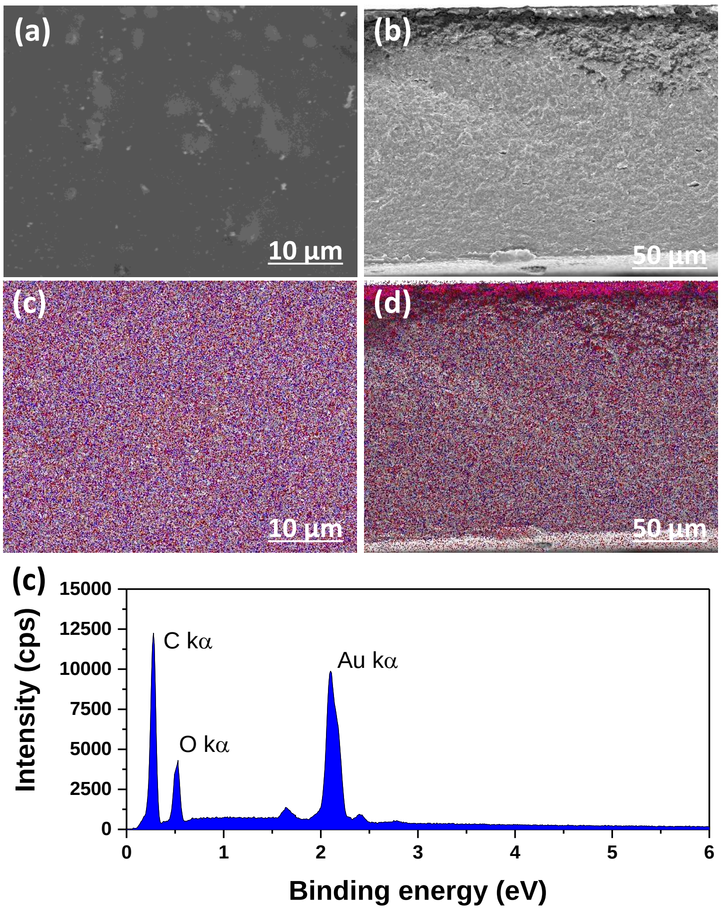

Fig. 5.4. EDX mapping and spectra of sample GNPs0% (with only polymer matrix). Elemental identifications for carbon and oxygen are given as red and green colours, respectively.

5.4.2 Chemical and structural characterization

In IR analysis, pure cotton fabric and the regenerated cellulose film show similar characteristic peaks attributed to cellulose structure. As shown in Fig. 5.5a, IR spectra of cotton fabric shows well-known distinct bands associated with cellulose-I structure, namely, O-H stretching at 3364 cm^{-1}, C-H stretching at 2891 cm^{-1}, adsorbed water at 1645 cm^{-1}, ring breathing at 1157 cm^{-1} and C-O stretching at 1026 cm^{-1} [144,208]. However, after TFA digestion and regeneration, significant broadening of the peak attributed to O-H stretching at 3100-3400 cm^{-1} appears (sample GNPs0%), indicating transformation of cellulose-I (crystalline) to cellulose-II (amorphous) structures and associated changes in inter and intra-molecular hydrogen bonds[185,244].

Raman spectra was also collected for sample GNPs25% (see Fig. 5.5b) and shows characteristic bands associated to GNPs utilized. As discussed in the previous chapter, here again, GNPs are characterized as more like graphitic materials with intensity of $2D_2 > 2D_1$ (Fig. 5.5b inset) indicating more than 8 graphene layers [169,184]. Three additional peaks around 900 cm^{-1}, 1100 cm^{-1} and 2895 cm^{-1} also appear in the collected spectra and attributed to cellulose structure[245].

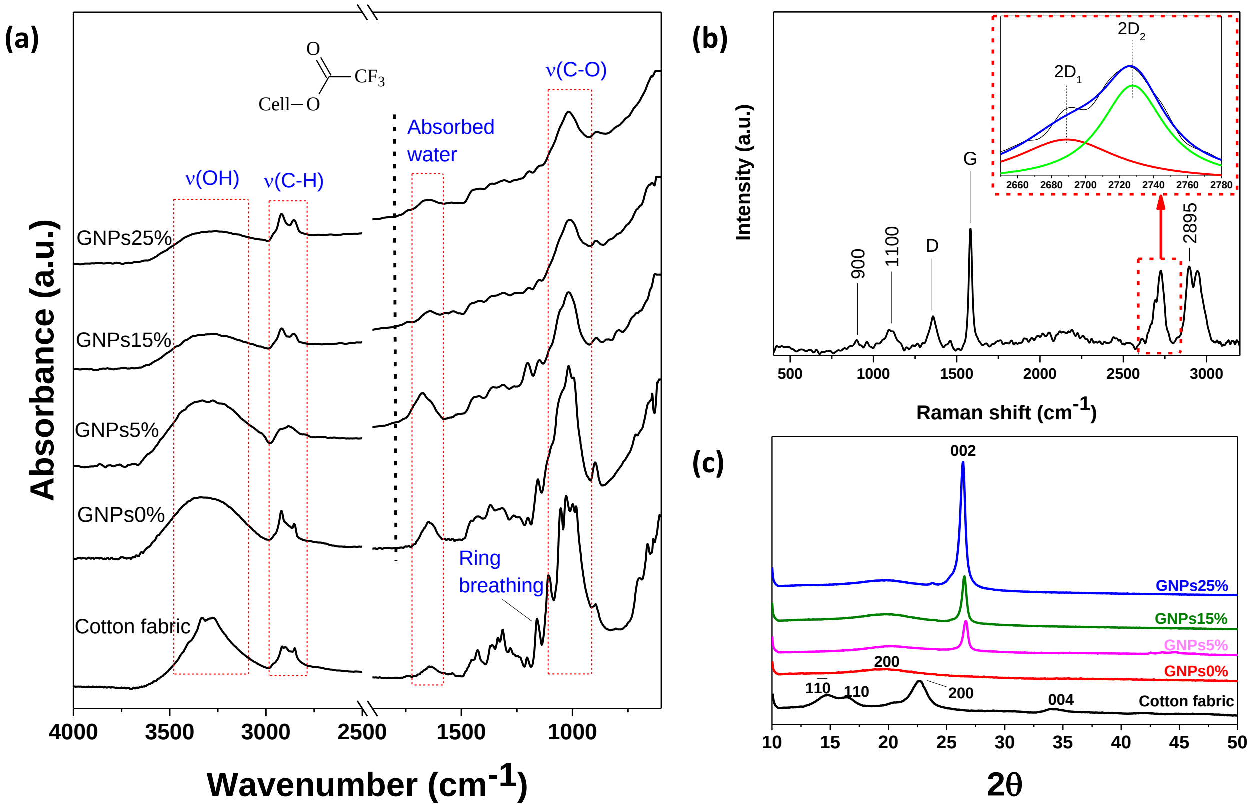

Fig. 5.5. Chemical characterization. (a) ATR-FTIR spectra of cotton, regenerated cellulose and cellulose/GNPs nanocomposites. Assignments for cellulose vibrations (blue) have been indicated. b) Raman spectra of GNPs25%. Inset shows deconvolution of 2D peak around 2700 cm^{-1}. (c) X-ray diffraction pattern of cotton fibres, regenerated cellulose films and cellulose/GNPs nanocomposites.

Fig. 5.5c shows XRD profiles of the cotton fabric and regenerated cellulose films with different GNPs mass fractions, such as, sample GNPs0%, GNPs5%, GNPs15% and GNPs25%. Cotton fabric shows a sharp peak at $2\theta = 22.6°$ and two relatively weak diffraction peaks at $2\theta = 14.8°$ with a shoulder at 16.4°, and at 34.0° associated to cellulose-I structure[208,246]. In contrast, regenerated cellulose film (sample GNPs0%) shows a typical diffraction pattern of cellulose-II including a broad peak at $2\theta = 20.0°$[247]. This alteration in the crystalline structure is attributed to the change in inter- and intra-molecular hydrogen bonding networks by TFA dissolution and resulting a relatively less ordered cellulose-II structure. In addition to cellulose-II peak, the XRD patterns of cellulose/GNPs nanocomposites also demonstrate very intense peaks at $2\theta = 26.5°$ related to the GNPs basal plane[174,248].

5.4.3 Stress-strain properties

To investigate mechanical behaviour of the cellulose/GNPs nanocomposites, stress–strain curves and Young's modulus of different samples with increasing GNPs mass fraction are shown in Fig. 5.6. A pristine cellulose film with no GNPs (sample GNPs0%) and a commercial TIM sample have also been included for comparison purpose. Fig. 5.6a shows a typical stress-strain curve for regenerated cellulose film. As seen in Fig. 5.6a, in pristine cellulose film yield point occurs at 4.48% elongation with 56 MPa applied stress. Further extension beyond the yield point results in a plastic deformation and finally, the film breaks at 28% maximum elongation. In the elastic region, Young's modulus of 1935 MPa is recoded for this pristine cellulose film, as shown in Fig. 5.6b. On the other hand, when GNPs mixed are mixed with the cellulose matrix, mechanical properties are increasingly affected by their incorporated mass fractions. It is observed that samples GNPs5% and GNPs10% exhibit a noticeable increase of 16% and 27% in Young's modulus reaching 2254 MPa and 2466 MPa, respectively, see Fig. 5.6b. However, as the GNPs content increases, the maximum strain dramatically decreases from 28% to 14% and 5.5% for 5 wt.% and 10 wt.% mass fractions, respectively. Further increasing the GNPs content in nanocomposites negatively affects both Young's modulus and maximum elongation at break. Namely, Young's modulus of samples GNPs15% and GNPs20% are again reduced to ca. 1950 MPa with maximum elongation at break of 5.2% and 3%, respectively. This can be attributed to the large proportions of GNPs in the nanocomposites.

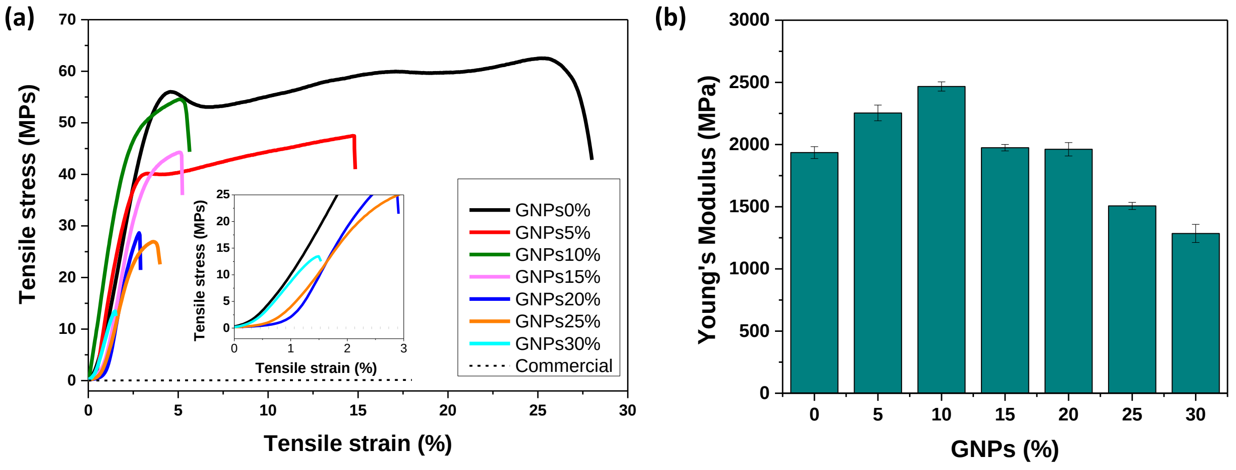

Fig. 5.6. (a) Stress-strain curves of different GNPs mass fractions (GNPs0% to GNPs30%). A commercial sample also have been included for comparison purpose. Inset figure shows initial stress-strain zone with fewer samples. (b) Young's modulus of the corresponding samples.

Similar to sample GNPs20%, sample GNPs25% breaks at 4% maximum elongation and Young's modulus is further reduced to 1506 MPa. Beyond this 25 wt.% addition, the prepared nanocomposites lost their 90% elongation and 50% Young's modulus. It is worth noting that the compared commercial sample show no mechanical strength and ultimately breaks at 17% elongation, see Fig. 5.6a. Whereas our best sample with 25 wt.% GNPs content maintained a high Young's modulus of 1500 MPa and 4% elongation at break, as shown in Fig. 5.6a and 5.6b.

5.4.4 Electrical conductivity

Pure cellulose sheet are highly insulating materials with sheet resistance ca. 10^8-10^9 Ω/sq and practically zero conductivity. When GNPs are mixed with polymer matrix above a certain proportions, due to high intrinsic electrical conductivity of GNPs[221], the prepared cellulose/GNPs nanocomposites exhibit transportation of electrical charges. As shown in Fig. 5.7, at very low mass fractions of GNPs ≤ 10 wt.%, the prepared nanocomposites demonstrate sheet resistance around 4 order of magnitude and less than 0.003 S/cm electrical conductivity. At this mass fraction, as seen SEM images, GNP-GNP network were not established throughout the polymer matrix. Further increase in mass fractions of GNPs could only produce surface resistance in the range of 1.5 kΩ/sq. corresponding to 0.03 S/cm, as shown in Fig. 5.7.

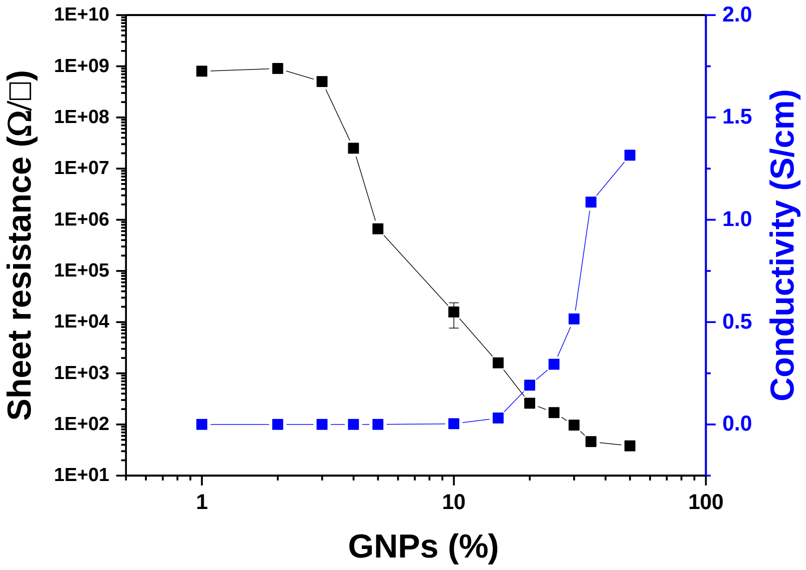

Fig. 5.7. Electrical sheet resistances and conductivities at different mass fractions of the GNPs.

Fig. 5.7 shows a significant improvement in electrical conductivity from 0.031 S/cm (corresponding to 1.5 kΩ/sq.) to 0.294 S/cm (170 Ω/sq.) at 25 wt.% mass fraction of GNPs (GNPs-25%). As discussed above, at this mass fraction, continuous networks of GNPs embedded in the polymer matrix were established (see Fig. 5.3g-h). It is worth noting that by adding GNPs ≥ 30 wt.% into the nanocomposites, electrical conductivity reaches to more than 0.50 S/cm, however, the prepared nanocomposites loss their mechanical properties significantly. Therefore, the sample GNPs25% with optimal electrical and mechanical properties is elected as best nanocomposite.

5.4.5 Thermal properties

Thermal properties of the prepared samples were measured by replicating a real electronic application. We have prepaid a setup where bottom plate is at high temperature T_1 (like processor) and top plate is acting as a heat sinker having room temperature T_2, as shown in Fig. 5.1. When the two plates bottom and top come in contact with TIMs in between them, an efficient exchange of thermal energy happens between the two plates. Consequently, bottom plate with high temperature T_1 cools down and the other plate at T_2 take up the heat and dissipate it.

Fig. 5.8 shows thermal kinetics of the top and bottom plates for the prepared nanocomposite used as TIMs. Namely, samples GNPs0%, GNPs10%, GNPs15% and GNPs25% have been characterized for their thermal kinetics. Two other samples with known value of k also have been used for correlation purpose, such as, a commercial sample with k = 6.0 W/mK and another sample of pure clay with k = 1.0 W/mK. As seen in Fig. 5.8, when commercial sample is used between the two plates, temperature of top and bottom plates changes very quickly. As such, within first 60 s of contact, the bottom/cooling plate reaches from 90 °C to 69 °C and the top/heating plate reaches at 52 °C form 24 °C. After 120 s, bottom and top plates reach at 67 °C and 59 °C, respectively. This difference is further minimized after 300 s and both plates are in equilibrium at 67 °C and 62°C, however, after 600 s both plates are reached to 70 °C and 64 °C, respectively, keeping a constant temperature difference of 5 °C to 6 °C. On the other hand, the clay sample with relatively low thermal conductivity (1 W/mK) demonstrate very slow thermal kinetic. As seen in Fig. 5.8, the bottom and top plates with clay sample reach at 78 °C and 37 °C after first 60 s, 73 °C and 44 °C after 120 s, 70 °C and 53 °C after 300 s and, 73 °C and 58 °C after 600 s, respectively. In contrast to commercial sample, clay sample produces a temperature difference of 12 °C at the end of 600 s, as obvious from its low thermal conductivity (k = 1.0 W/mK).

Our prepared cellulose/GNPs nanocomposites with 10 wt.% (sample GNPs10%) and 15 wt.% (sample GNPs15%) of GNPs also produced somewhat similar thermal kinetics for both top and bottom plates, whereas, pristine cellulose film (sample GNPs0%) is much slower than its counter parts, as shown in Fig. 5.8. Interestingly, sample GNPs25% with 25 wt.% mass fraction demonstrates an improved thermal kinetics and exchange of temperature between top and bottom plates. In this case, the bottom and top plates are reached at 71 °C and 43 °C after 60 s, 67 °C and 51 °C after 120 s, 66 °C and 57 °C after 300 s and, 69 °C and 60 °C after 600 s, respectively. Likewise commercial material, sample GNPs25% stabilizes after 600 s with a temperature difference of 9 °C, as shown in Fig. 5.8. Thermal camera images of the corresponding materials are shown in Fig. 5.9, where each pixel represents a certain temperature value given in the scale on the right side. As can be seen in Fig. 5.9, at start of the contact time, that is 0 s, temperature of the bottom plate is at 85 °C with top plate at 25 °C, corresponding to the pixel colours. During the 600 s of contact, the TIM samples transfer thermal energy from bottom plate to top plate, resulting decrease in the temperature of the bottom plate and relative increase in temperature of top plate, as seen in Fig. 5.9.

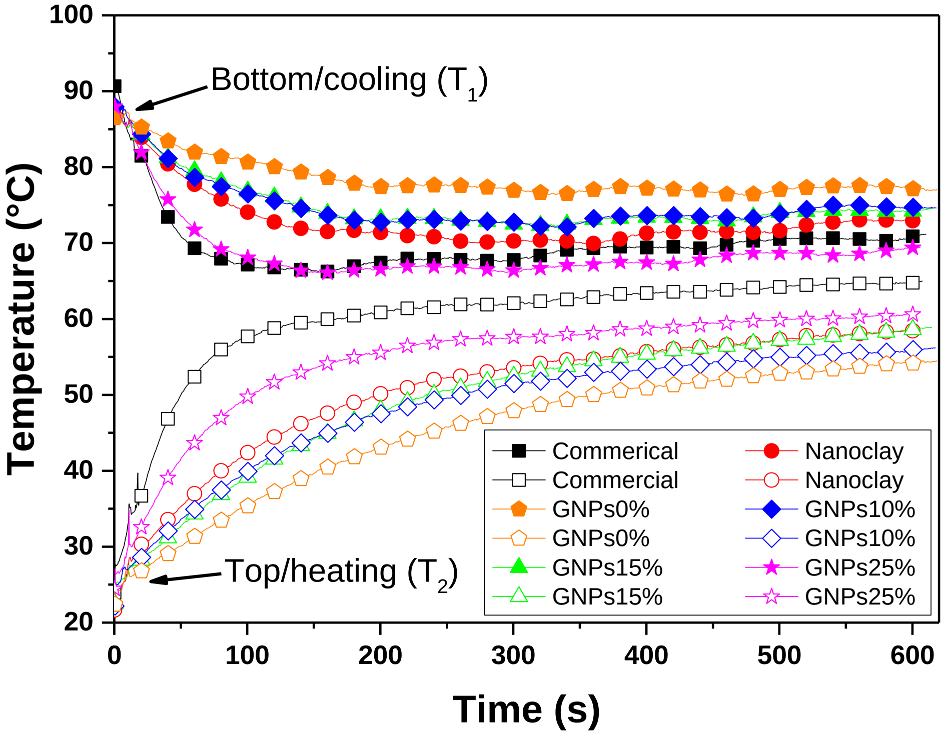

Fig. 5.8. Thermal kinetics of two sample with known thermal conductivity and the cellulose/GNPs based TIMs. Change in temperatures of bottom/heat source (T_1) and top/heat sink (T_2) are indicated by solid and hollow bullets, respectively.

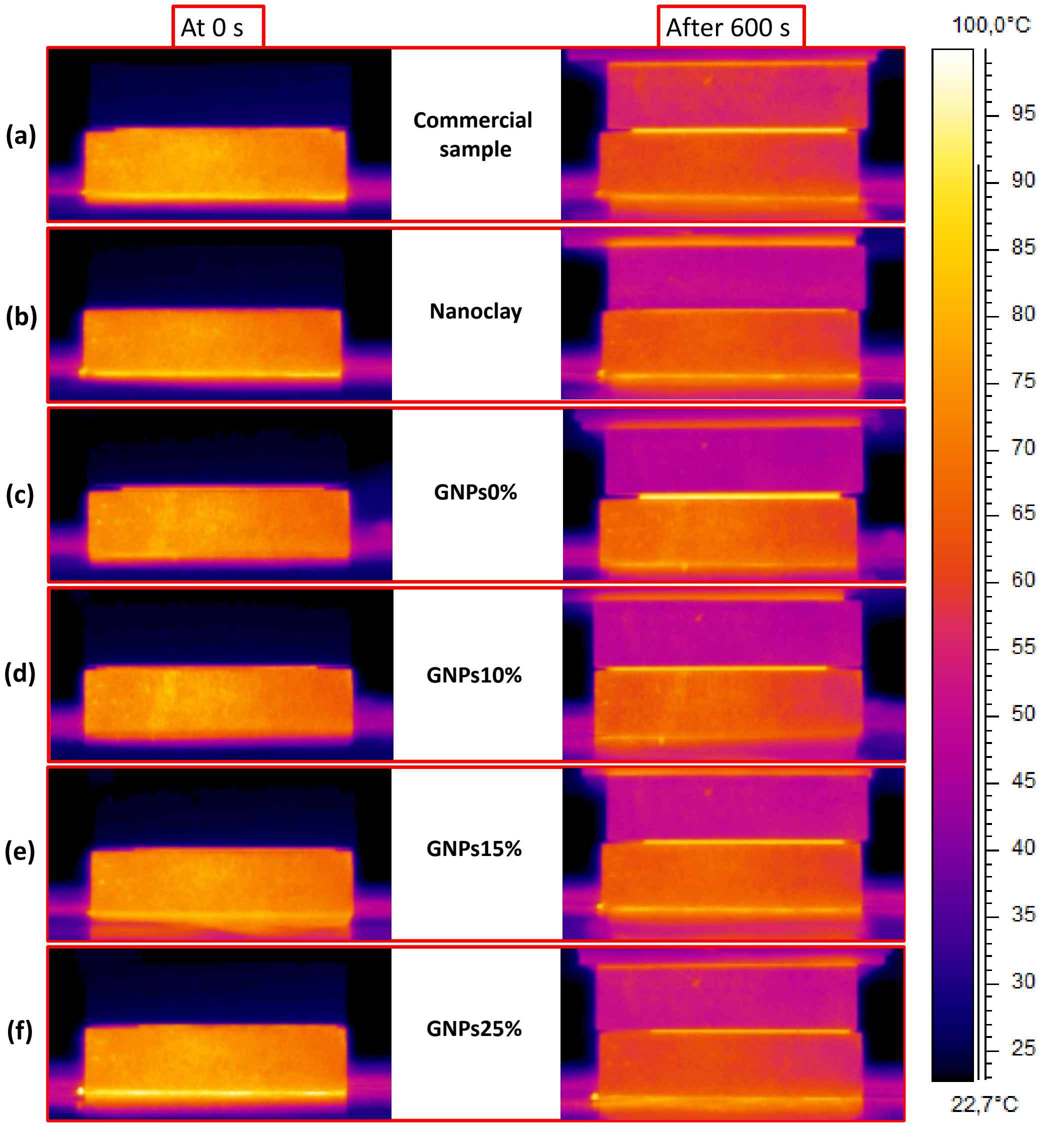

Fig. 5.9. IR camera images of the prepared nanocomposites samples and samples with known values of *k*.

To estimate the thermal conductivities of the prepared samples, ΔT for each sample have been plotted against contact time of the bottom and top plates, as shown in Fig. 5.10. For instance, after 100 s, commercial sample with thermal conductivity of 6.0 W/mK and pure clay with thermal conductivity of 1.0 W/mK reach a ΔT of 9.44 °C and 31.67 °C, respectively. On the other hand, sample GNPs25% reaches to 18.50 °C in the same time as shown in Fig. 5.10. similarly, samples GNPs0%, GNPs10% and GNPs15% reach to ΔT = 45.39 °C, 36.67 °C and 37.76 °C, respectively. For these observations, it can be concluded that sample GNPs0%, GNPs10% and GNPs15% have thermal conductivity of less than 1.0 W/mK. On the other hand, thermal conductivity of sample GNPs25% with value of ΔT between commercial and clay samples can be characterized to $k \approx 4.0$ W/mK.

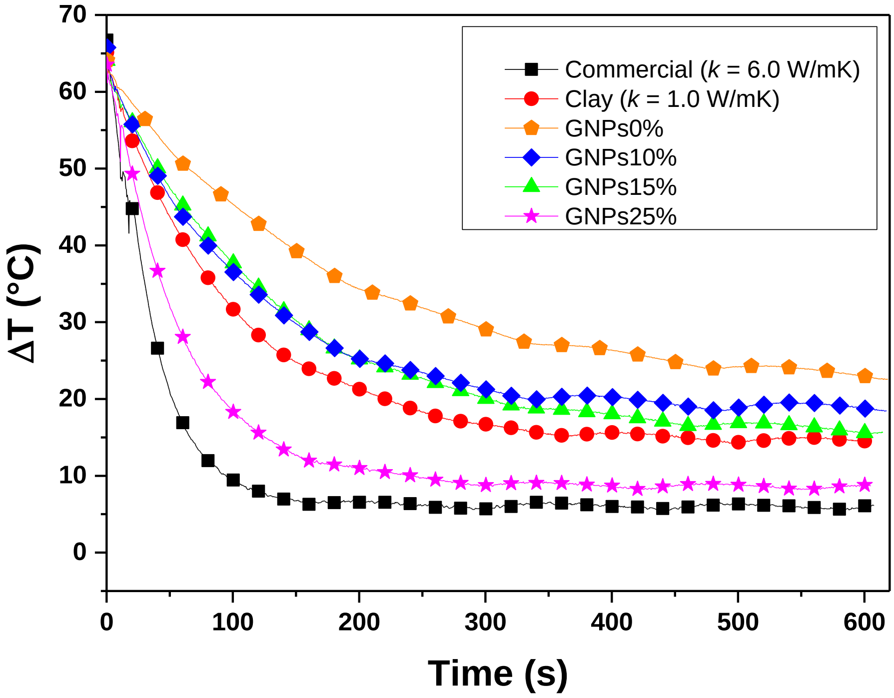

Fig. 5.10. Temperature difference (ΔT) of corresponding TIMs as a function of contact time.

5.5 Conclusion

This preliminary part of the study is focusing on fabrication of regenerated cellulose/GNPs nanocomposites based sustainable TIMs. The prepared nanocomposites display good electrical conductivity (0.515 S/cm) and estimated thermal conductivity (≈4.0 W/mK) at 25 wt.% mass fraction of GNPs. At this mass fraction, good mechanical strength (Young’s modulus 1500 MPa) ensures reusability, easy replicability and zero pumping out features. As the prepared nanocomposite TIMs are very stiff and non-conformal to the applied surfaces, an issue of contact resistance is still under study and will be resolved soon. We are also working to develop a mathematical model to indirectly calculate thermal conductivities from ΔT vs. time graphs.

Remarks and future works

This thesis aimed at the development of multifunctional cotton fabrics based on sustainable materials. This study gives information on surface modification of conventional cotton fabrics through alternative treatments involving eco-friendly and non-toxic materials. The fabrication of superhydrophobic cotton fabrics using C-6 fluorinated chemistry combined with a silicone protective layer (chapter 2) have special attraction. As such, the modified cotton fabrics by sequential polymer treatment demonstrate good water repelling and physical properties. These superhydrophobic cotton fabrics can be implemented for sports, uniforms, packaging and leisure activities. Similarly, electro-conductive cotton fabrics (chapter 3) successfully prepared by conductive polymer and graphene inks have several applications including power and signal transmission, strain-sensing and textile based supercapacitors. The conductive polymer and graphene based cotton fabrics exhibit high conductivity and wearability aspects. A special attention have been devoted towards the mechanical strength and porosity of the prepared conductive fabrics. Additionally, the conductive fabrics display good resistance against washing and folding-unfolding cycles.

Multifunctional textiles with antibacterial and self-cleaning properties (chapter 4) have also been realized in this research thesis. For this purpose, Mn-doped TiO_2 photocatalytic nanoparticles are immobilized on the surface of cotton fabrics using silicone binder. The prepared multifunctional nanocomposite fabrics display good killing kinetics against a gram-negative bacterium under sunlight. Likewise, the functionalized cotton fabrics are able to discolour an organic dye stains on their surface under UV as well as visible light. Here again, the prepared multifunctional cotton fabrics maintain their physical features. In the last part of this thesis, an overwhelming issue of plastic waste around the globe have been addressed by preparing a regenerated bioplastic form waste fabrics. A simple and scalable route for cellulose based regenerated bioplastic have been demonstrated using cotton fabrics dissolved into an acidic solvent and solvent casting techniques. The prepared cellulose films demonstrate good electrical and thermal properties when mixed with conductive nanofillers, here graphene. Although this work is currently under study, some important milestones have been already achieved and discussed in this part.

Functional textiles discussed in this work exhibit several properties that make them attractive in many applications. They represent an environmentally friendly alternative to conventional synthetic materials. In future, the efforts will be devoted to develop materials with many other properties, such as, impact resistance, flame retardancy and last but not least shielding effects. Furthermore, combining the bio-based cellulose (cotton fabrics) with ecological production methods, by utilising biocompatible media, for example, will be the top most priority.

Appendix-I

Supporting information

i. Preliminary study by large water droplets

In this study two single layer samples namely PDMS and PDMS/SiO_2 treated cotton fabrics were prepared. The amount of nanoparticles used for second sample was same as that of sample SiNPs30 (Chapter : 2) by weight. Third sample was prepared with multilayer approach where pretreated nanocomposite fabric (with fluorinated acrylic copolymer and silica nanoparticles) was treated with acetoxy-PDMS as a secondary layer (Sample SiNPs30). Prepared fabrics were subjected to a static water blob of 200 µL for prolonged time (Fig. S1). Samples were covered with a large glass petri dish to minimize water evaporation and fixed with double adhesive tape to get straight surfaces. Cotton fabric treated with acetoxy-PDMS alone was infiltrated by water volume before an hour of contact (Fig. S1a). However, nanoparticles addition to PDMS solution was helpful to double the resistance time for water infiltration. Because of nanoparticles, the entrapped air packets present a barrier to water infiltration. As the air packets are depleted, the result is same as that of PDMS treated fabric (Fig. S1b). In contrast, the multilayer PDMS treated nanocomposite fabric (SiNPs30) exhibited higher resistance to water infiltration than PDMS alone or with silica nanoparticles. In Fig. S1c, water blob is still present after more than 2 hours of contact. Interestingly, there is no stain of water infiltration (Fig. S1d) when droplet was removed after 2 hours as compared to first two treatments.

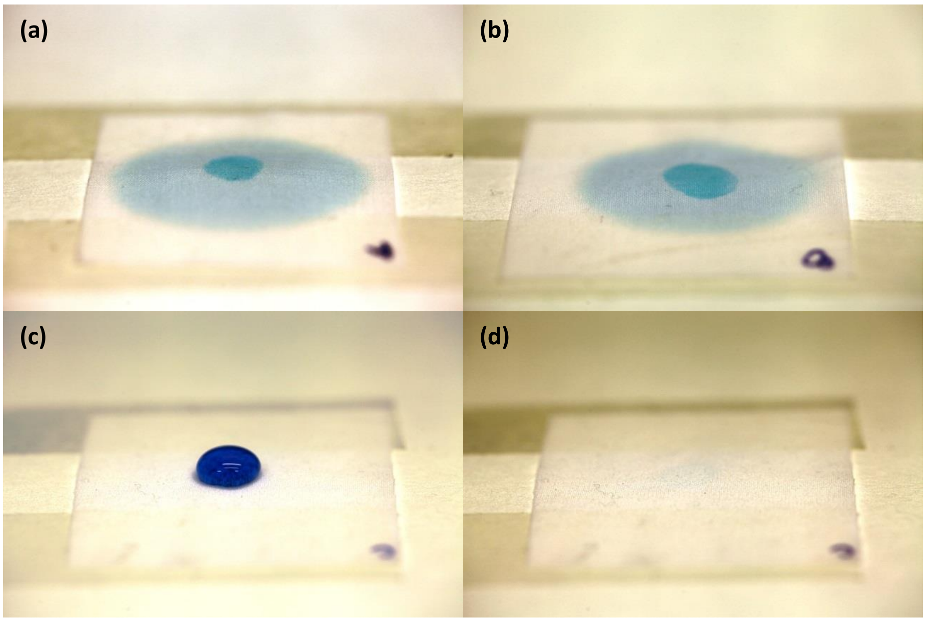

Fig. S1. Photographs of preliminary study for water infiltration with water blob of 200 µL volume in static position. (a) acetoxy-PDMS treated cotton fabric after an hour of contact. (b) Silica nanoparticles blended acetoxy-silicone polymer treated fabric after 2 hours of water blob contact. (c) Multilayer treated cotton fabric (SiNPs30) is more resistant to water blob. Water blob is unable to submerge. (d) PDMS treated nanocomposite fabric (SiNPs30) when water blob is removed after 2 hours.

ii. Surface wettability after ultrasonic washing test

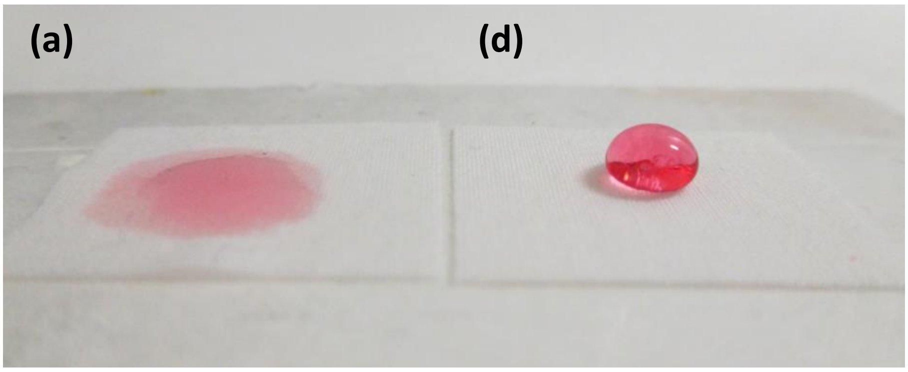

Fig. S2. Surface wetting of Sample (a) control-F (b) SiNPs30 after ultrasonic washing process. Images were taken after 1 minute of water blob (200 µL) deposition.

iii. EDX measurements of abrasion test

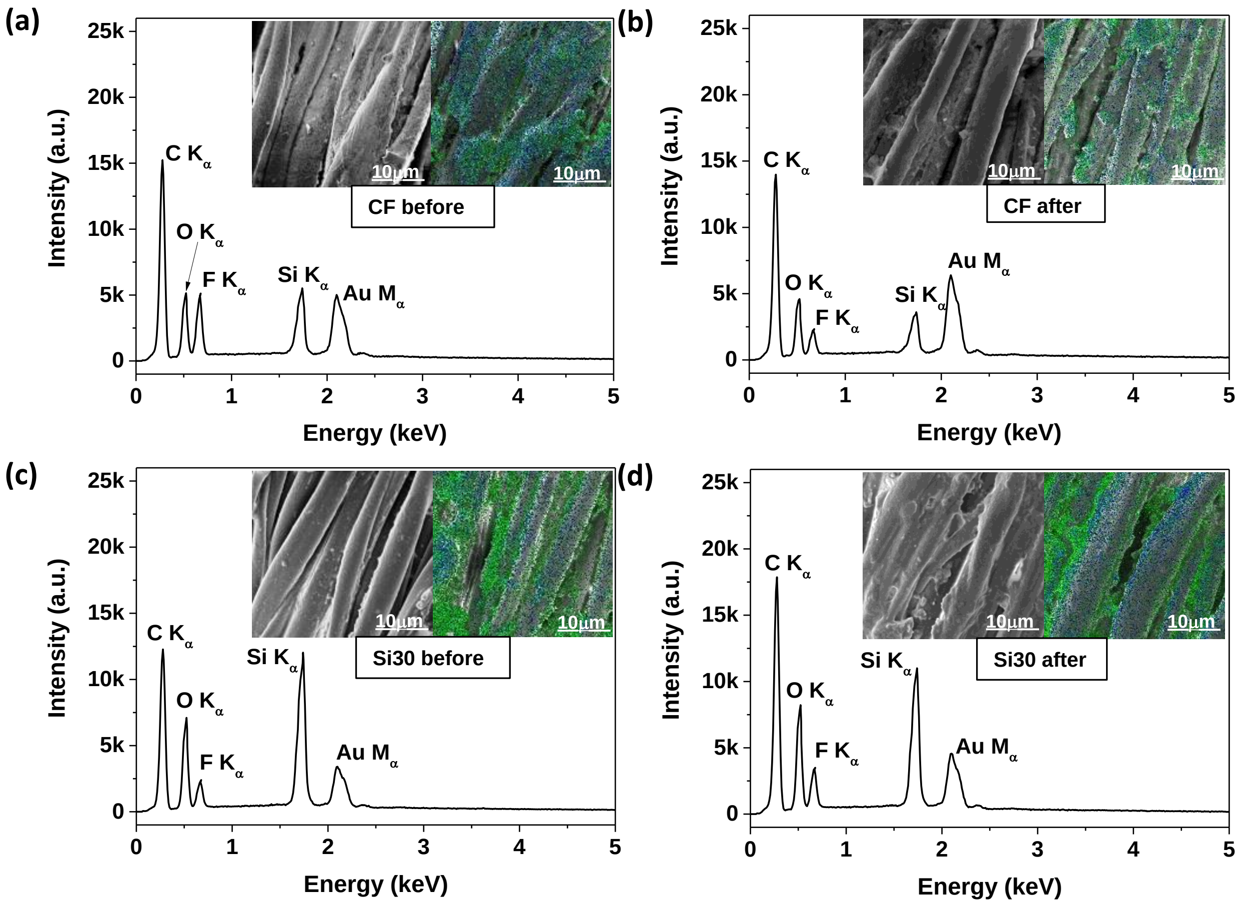

Fig. S3. EDX analysis of treated cotton fabrics after abrasion test. EDX spectra of control fabric CF (a) before and (b) after 17 abrasion cycles. EDX spectra of PDMS treated sample Si30 (c) before and (d) after

30 abrasion cycles. Inset visual of SEM images and EDX overlaid images of corresponding samples are also given with signal indication of silicon (green points) and fluorine (blue points).

iv. Transmission electron microscopy (TEM)

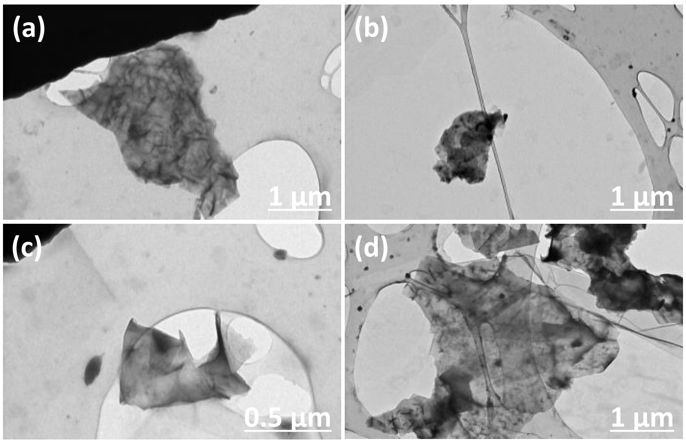

Fig. S4. TEM images of the graphene nanoplatelets (Ultra G$^+$).

v. Raman spectra of unmercerized and mercerized cotton fabrics

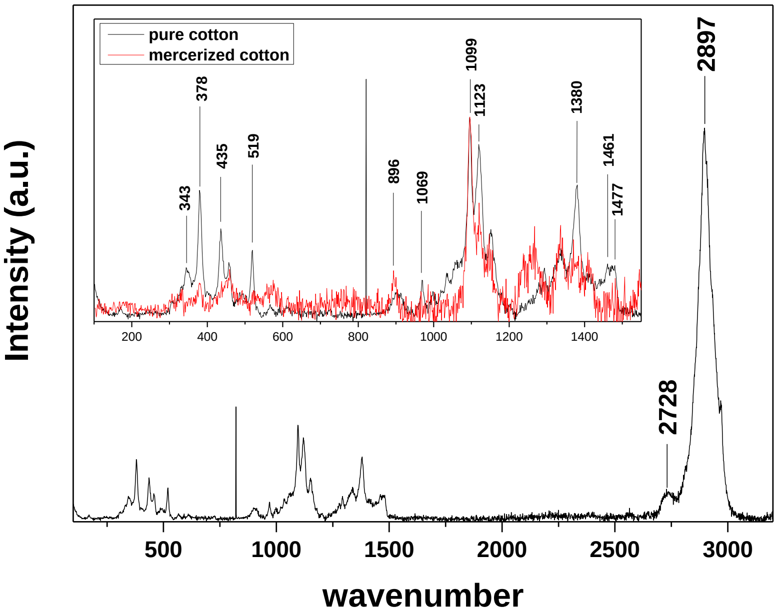

Figure S5. Raman spectra of unmercerized (black) and mercerized (red) cotton fabrics. Inset image confirms the vibrational changes occurred during transition from Cellulose-I to Cellulose-II structure by mercerization treatment.

vi. Mercerization effect on sheet resistance of PEDOT:PSS and GNPs coated cotton fabrics

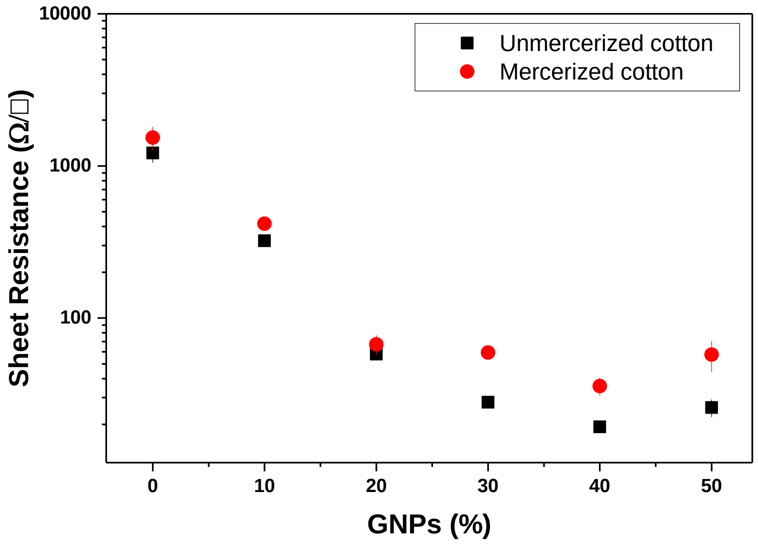

Fig. S6. Sheet resistance of PEDOT:PSS and GNPs coated cotton fabrics. Sheet resistance of cotton fabrics before mercerization (black square) and after mercerization (red circle) have been given as a function of GNPs mass fractions (0-50 wt.%).

vii. Cyclic deformation of PEDOT:PSS and GNPs coated cotton fabric

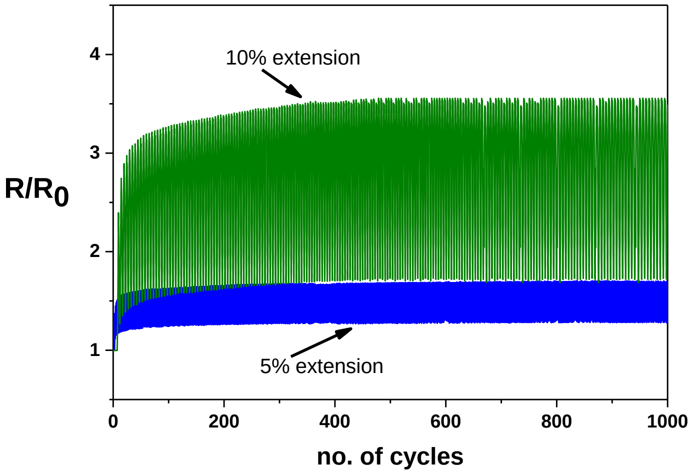

Fig. S7. Deformation stability of the conductive cotton fabrics (sample GNPs-20%) under 5% and 10% strains for 1000 cycles.

viii. Bacterial inactivation test

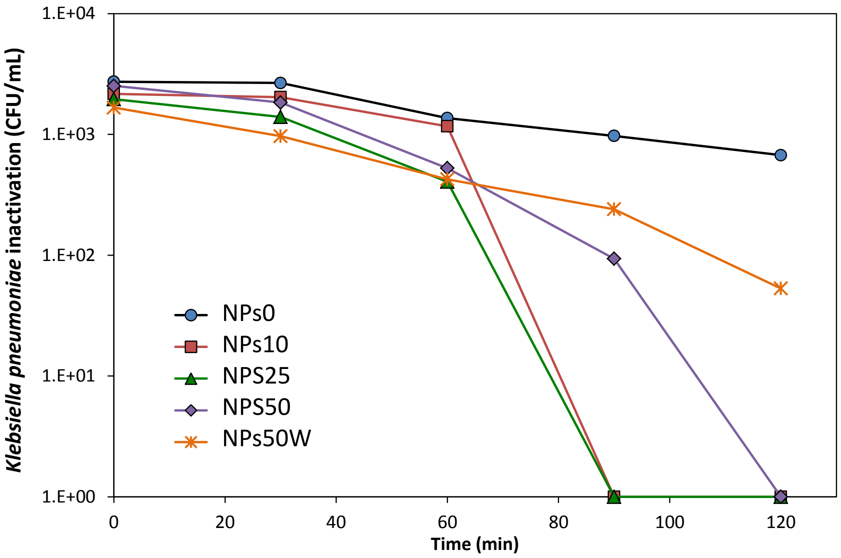

Figure S8. Inactivation of *Klebsiella pneumoniae* under sunlight.

ix. Degradation of MB dye under UV irradiation (self-cleaning)

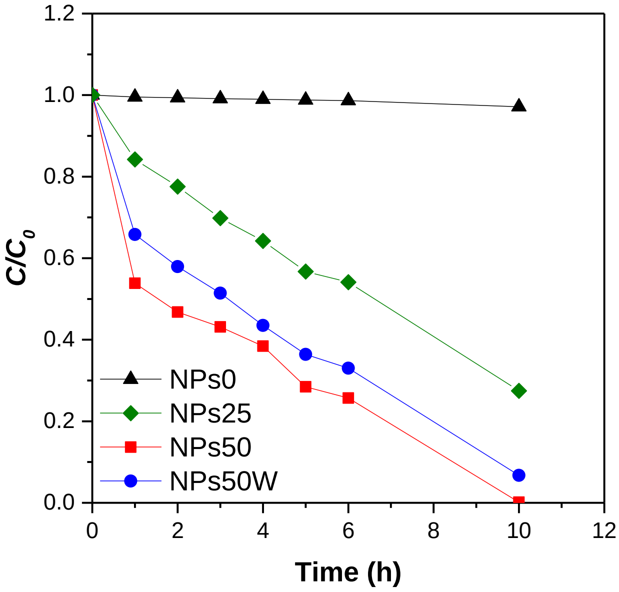

Figure S9. Degradation of MB dye stains by TiO_2:Mn NPs coated cotton fabric under UV light irradiation. Reduction in relative concentration (*C/C_0*) of MB model dye adsorbed on different samples is given as a function of UV irradiation time.

x. Degradation of MB dye in aqueous solution under UV irradiation (water purification)

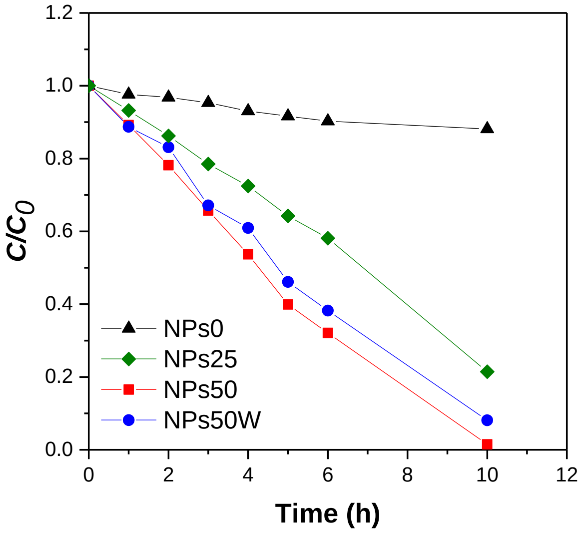

Figure S10. Degradation of MB in water (50 mL) by TiO_2:Mn NPs coated cotton fabric under UV light irradiation. Reduction in relative concentration (C/C_0) of MB model dye in aqueous solution by different coated samples is given as a function of UV irradiation time.

Appendix-II

List of publications

M. Zahid, E. L. Papadapoulou, A. Athanassiou, I. S. Bayer (2017). Strain-responsive mercerized conductive cotton fabrics based on PEDOT:PSS/Graphene. *Materials and Design*, vol. 135, pp. 213-222.

M. Zahid, J. A. Heredia-Guerrero, A. Athanassiou, I. S. Bayer (2017). Robust water repellent treatment for woven cotton fabrics with ecofriendly polymers. *Chemical Engineering Journal*, vol. 319, pp. 321 - 332.

M. Zahid, E. L. Papadapoulou, V. D. Binas, G. Kiriakidis, I. S. Bayer, A. Athanassioua (2017). Fabrication of Antibacterial and Self-Cleaning Cotton Fabrics Using Manganese Doped TiO2 Nanoparticles. (Submitted)

G. Mazzon, I. Zanocco, **M. Zahid**, I. S. Bayer, A. Athanassiou, L. Falchi, E. Balliana, E. Zendri (2017). Nanostructured coatings for the protection of textiles and paper. *Ge conservación [S.l.]*, vol. 1, pp. 180-188.

Conference presentations

World Academy of Science, Engineering and Technology (WASET)
18th International Conference on Material Science and Polymer Engineering (ICMSPE 2016), Istanbul Turkey
19-20 December, 2016
**Best speakers' award

Association of Universities for Textiles (AUTEX)
17th World Textile Conference (AUTEX 2017), Corfu Greece
29-31 May, 2017

Bibliography

1. Tarafder N. Functional textiles - A review. *Man-Made Text India*. 2010;38(11):13-19. doi:10.1177/0040517509357652.
2. Harifi T, Montazer M. Application of nanotechnology in sports clothing and flooring for enhanced sport activities, performance, efficiency and comfort: a review. *J Ind Text*. 2015:1-23. doi:10.1177/1528083715601512.
3. A Timeline of Textile Machinery Inventions. https://www.thoughtco.com/textile-machinery-industrial-revolution-4076291. Accessed December 4, 2017.
4. Phillips AW. The establishment of. 1975;109:65-76. doi:10.1080/0141192750010102.
5. Gulzar U, Goriparti S, Miele E, et al. Next-generation textiles: from embedded supercapacitors to lithium ion batteries. *J Mater Chem A*. 2016;4(43):16771-16800. doi:10.1039/C6TA06437J.
6. Global fiber market | LENZING Corporation. http://www.lenzing.com/en/investors/equity-story/global-fiber-market.html. Accessed December 4, 2017.
7. Singh AA, Palsule S. Coconut fiber reinforced chemically functionalized high-density polyethylene (CNF/CF-HDPE) composites by Palsule process. *J Compos Mater*. 2013;48(29):3673-3684. doi:10.1177/0021998313513045.
8. Wong YWH, Yuen CWM, Leung MYS, Ku SKA, Lam HLI. Selected applications of nanotechnology in textiles. *Autex Res J*. 2006;6(1):1-8.
9. Yetisen AK, Qu H, Manbachi A, et al. Nanotechnology in Textiles. *ACS Nano*. 2016;10(3):3042-3068. doi:10.1021/acsnano.5b08176.
10. Li S, Huang J, Chen Z, Chen G, Lai Y. A review on special wettability textiles: theoretical models, fabrication technologies and multifunctional applications. *J Mater Chem A*. 2017;5(1):31-55. doi:10.1039/C6TA07984A.
11. Feng BL, Li SH, Li YS, et al. Super-hydrophobic surfaces: From natural to artificial. *Adv Mater*. 2002;14(24):1857-1860. doi:DOI 10.1002/adma.200290020.
12. Koch K, Bhushan B, Barthlott W. Multifunctional surface structures of plants: An inspiration for biomimetics. *Prog Mater Sci*. 2009;54(2):137-178. doi:10.1016/j.pmatsci.2008.07.003.
13. Song J, Rojas OJ. Approaching super-hydrophobicity from cellulosic materials : A Review. *Pap Chem*. 2013;28(2):216-238. doi:10.3183/NPPRJ-2013-28-02-p216-238.
14. Ma M, Hill RM. Superhydrophobic surfaces. *Curr Opin Colloid Interface Sci*. 2006;11(4):193-202. doi:10.1016/j.cocis.2006.06.002.
15. Jeong WY, An SK. The transport properties of polymer membrane-fabric composites. *J Mater Sci*. 2001;36(19):4797-4803. doi:10.1023/A:1017995509102.
16. Xiong D, Liu G, Duncan EJS. Diblock-Copolymer-Coated Water- and Oil-Repellent Cotton Fabrics. 2012.
17. Yu M, Gu G, Meng WD, Qing FL. Superhydrophobic cotton fabric coating based on a complex layer of silica nanoparticles and perfluorooctylated quaternary ammonium silane coupling agent. *Appl Surf Sci*. 2007;253(7):3669-3673. doi:10.1016/j.apsusc.2006.07.086.
18. Zhang M, Wang C. Fabrication of cotton fabric with superhydrophobicity and flame retardancy. *Carbohydr Polym*. 2013;96(2):396-402. doi:10.1016/j.carbpol.2013.04.025.
19. Bahners T, Mölter-Siemens W, Haep S, Gutmann JS. Control of oil-wetting on technical textiles by means of photo-chemical surface modification and its relevance to the performance of compressed air filters. *Appl Surf*

Sci. 2014;313:93-101. doi:10.1016/j.apsusc.2014.05.146.

20. Xue CH, Jia ST, Zhang J, Tian LQ. Superhydrophobic surfaces on cotton textiles by complex coating of silica nanoparticles and hydrophobization. *Thin Solid Films*. 2009;517(16):4593-4598. doi:10.1016/j.tsf.2009.03.185.
21. Zhang M, Wang S, Wang C, Li J. A facile method to fabricate superhydrophobic cotton fabrics. *Appl Surf Sci*. 2012;261:561-566. doi:10.1016/j.apsusc.2012.08.055.
22. Zhu X, Zhang Z, Yang J, Xu X, Men X, Zhou X. Facile fabrication of a superhydrophobic fabric with mechanical stability and easy-repairability. *J Colloid Interface Sci*. 2012;380(1):182-186. doi:10.1016/j.jcis.2012.04.063.
23. Pereira C, Alves C, Monteiro A, et al. Designing novel hybrid materials by one-pot co-condensation: From hydrophobic mesoporous silica nanoparticles to superamphiphobic cotton textiles. *ACS Appl Mater Interfaces*. 2011;3(7):2289-2299. doi:10.1021/am200220x.
24. Ma W, Higaki Y, Takahara A. Superamphiphobic Coatings from Combination of a Biomimetic Catechol-Bearing Fluoropolymer and Halloysite Nanotubes. *Adv Mater Interfaces*. 2017;1700907:1700907. doi:10.1002/admi.201700907.
25. Qiang S, Chen K, Yin Y, Wang C. Robust UV-cured superhydrophobic cotton fabric surfaces with self-healing ability. *Mater Des*. 2017;116:395-402. doi:10.1016/j.matdes.2016.11.099.
26. Liu H, Huang J, Li F, et al. Multifunctional superamphiphobic fabrics with asymmetric wettability for one-way fluid transport and templated patterning. *Cellulose*. 2017;24(2):1129-1141. doi:10.1007/s10570-016-1177-6.
27. Chuang MC, Windmiller JR, Santhosh P, et al. Textile-based Electrochemical Sensing: Effect of Fabric Substrate and Detection of Nitroaromatic Explosives. *Electroanalysis*. 2010;22(21):2511-2518. doi:10.1002/elan.201000434.
28. Jones B. Fluoropolymers for Coating applications. *JCT coatingstech*. 2008;5(9):44-48. http://cat.inist.fr/?aModele=afficheN&cpsidt=20968975.
29. Martin JW, Mabury SA, Solomon KR, Muir DCG. Progress toward understanding the bioaccumulation of perfluorinated alkyl acids. *Environ Toxicol Chem*. 2013;32(11):2421-2423. doi:10.1002/etc.2376.
30. Schutzius TM, Bayer IS, Tiwari MK, Megaridis CM. Novel fluoropolymer blends for the fabrication of sprayable multifunctional superhydrophobic nanostructured composites. *Ind Eng Chem Res*. 2011;50(19):11117-11123. doi:10.1021/ie200814r.
31. Chengelis CP, Kirkpatrick JB, Radovsky A, Shinohara M. A 90-day repeated dose oral (gavage) toxicity study of perfluorohexanoic acid (PFHxA) in rats (with functional observational battery and motor activity determinations). *Reprod Toxicol*. 2009;27(3-4):342-351. doi:10.1016/j.reprotox.2009.01.006.
32. Mazrouei-Sebdani Z, Khoddami A. Alkaline hydrolysis: A facile method to manufacture superhydrophobic polyester fabric by fluorocarbon coating. *Prog Org Coatings*. 2011;72(4):638-646. doi:10.1016/j.porgcoat.2011.07.006.
33. Liu Y, Xin JH, Choi CH. Cotton fabrics with single-faced superhydrophobicity. *Langmuir*. 2012;28(50):17426-17434. doi:10.1021/la303714h.
34. Zhou X, Zhang Z, Xu X, et al. Robust and durable superhydrophobic cotton fabrics for oil/water separation. *ACS Appl Mater Interfaces*. 2013;5(15):7208-7214. doi:10.1021/am4015346.
35. Deng B, Cai R, Yu Y, et al. Laundering durability of superhydrophobic cotton fabric. *Adv Mater*. 2010;22(48):5473-5477. doi:10.1002/adma.201002614.
36. JARVIS NL, Zisman WA. *Surface Chemistry of Fluorochemicals*.; 1965.

37. Manatunga DC, De Silva RM, De Silva KMN. Double layer approach to create durable superhydrophobicity on cotton fabric using nano silica and auxiliary non fluorinated materials. *Appl Surf Sci*. 2016;360:777-788. doi:10.1016/j.apsusc.2015.11.068.

38. Xue CH, Yin W, Zhang P, Zhang J, Ji PT, Jia ST. UV-durable superhydrophobic textiles with UV-shielding properties by introduction of ZnO/SiO2 core/shell nanorods on PET fibers and hydrophobization. *Colloids Surfaces A Physicochem Eng Asp*. 2013;427:7-12. doi:10.1016/j.colsurfa.2013.03.021.

39. Zhu Q, Gao Q, Guo Y, Yang CQ, Shen L. Modified silica sol coatings for highly hydrophobic cotton and polyester fabrics using a one-step procedure. *Ind Eng Chem Res*. 2011;50(10):5881-5888. doi:10.1021/ie101825d.

40. Shateri Khalil-Abad M, Yazdanshenas ME. Superhydrophobic antibacterial cotton textiles. *J Colloid Interface Sci*. 2010;351(1):293-298. doi:10.1016/j.jcis.2010.07.049.

41. Yazdanshenas ME, Shateri-Khalilabad M. One-step synthesis of superhydrophobic coating on cotton fabric by ultrasound irradiation. *Ind Eng Chem Res*. 2013;52(36):12846-12854. doi:10.1021/ie401133q.

42. Wu Y, Qi H, Li B, Zhanhua H, Li W, Liu S. Novel hydrophobic cotton fibers adsorbent for the removal of nitrobenzene in aqueous solution. *Carbohydr Polym*. 2017;155:294-302. doi:10.1016/j.carbpol.2016.08.088.

43. Hou K, Zeng Y, Zhou C, et al. Facile generation of robust POSS-based superhydrophobic fabrics via thiol- ene click chemistry. 2018;332(September 2017):150-159.

44. Shirgholami MA, Shateri Khalil-Abad M, Khajavi R, Yazdanshenas ME. Fabrication of superhydrophobic polymethylsilsesquioxane nanostructures on cotton textiles by a solution-immersion process. *J Colloid Interface Sci*. 2011;359(2):530-535. doi:10.1016/j.jcis.2011.04.031.

45. Shirgholami MA, Shateri-Khalilabad M, Yazdanshenas ME. Effect of reaction duration in the formation of superhydrophobic polymethylsilsesquioxane nanostructures on cotton fabric. *Text Res J*. 2012;83(1):100-110. doi:10.1177/0040517512444335.

46. Zimmermann J, Reifler FA, Fortunato G, Gerhardt LC, Seeger S. A simple, one-step approach to durable and robust superhydrophobic textiles. *Adv Funct Mater*. 2008;18(22):3662-3669. doi:10.1002/adfm.200800755.

47. Li J, Yan L, Tang X, Feng H, Hu D, Zha F. Robust Superhydrophobic Fabric Bag Filled with Polyurethane Sponges Used for Vacuum-Assisted Continuous and Ultrafast Absorption and Collection of Oils from Water. *Adv Mater Interfaces*. 2016;3(9):3-10. doi:10.1002/admi.201500770.

48. Xue CH, Ji PT, Zhang P, Li YR, Jia ST. Fabrication of superhydrophobic and superoleophilic textiles for oil-water separation. *Appl Surf Sci*. 2013;284:464-471. doi:10.1016/j.apsusc.2013.07.120.

49. Xue C-H, Li Y-R, Hou J-L, Zhang L, Ma J-Z, Jia S-T. Self-roughened superhydrophobic coatings for continuous oil–water separation. *J Mater Chem A*. 2015;3(19):10248-10253. doi:10.1039/C5TA01014D.

50. Zhu T, Li S, Huang J, Mihailiasa M, Lai Y. Rational design of multi-layered superhydrophobic coating on cotton fabrics for UV shielding, self-cleaning and oil-water separation. *Mater Des*. 2017;134:342-351. doi:10.1016/j.matdes.2017.08.071.

51. Mishra H, Schrader AM, Lee DW, et al. Time-Dependent Wetting Behavior of PDMS Surfaces with Bioinspired, Hierarchical Structures. *ACS Appl Mater Interfaces*. 2016;8(12):8168-8174. doi:10.1021/acsami.5b10721.

52. Wang Y, Jiang H, Tao Y, et al. Polypyrrole/poly(vinyl alcohol-co-ethylene) nanofiber composites on polyethylene terephthalate substrate as flexible electric heating elements. *Compos Part A Appl Sci Manuf*. 2016;81:234-242. doi:10.1016/j.compositesa.2015.11.011.

53. Fugetsu B, Akiba E, Hachiya M, Endo M. The production of soft, durable, and electrically conductive polyester multifilament yarns by dye-printing them with carbon nanotubes. *Carbon N Y*. 2009;47(2):527-530. doi:10.1016/j.carbon.2008.11.013.

54. Zhao H, Hou L, Lu Y. Electromagnetic interference shielding of layered linen fabric / polypyrrole / nickel (LF / PPy / Ni) composites. *Jmade*. 2016;95:97-106. doi:10.1016/j.matdes.2016.01.088.

55. Cherenack K, Van Pieterson L. Smart textiles: Challenges and opportunities. *J Appl Phys*. 2012;112(9). doi:10.1063/1.4742728.

56. Gao M, Li L, Song Y. Inkjet printing wearable electronic devices. *J Mater Chem C*. 2017;5(12):2971-2993. doi:10.1039/C7TC00038C.

57. Shim BS, Chen W, Doty C, Xu C, Kotov NA. Smart electronic yarns and wearable fabrics for human biomonitoring made by carbon nanotube coating with polyelectrolytes. *Nano Lett*. 2008;8(12):4151-4157. doi:10.1021/nl801495p.

58. Park S, Jayaraman S. Smart Textiles:Wearable Electronic Systems. *Mrs Bull*. 2003;(August):585-591. doi:10.1557/mrs2003.170.

59. Zeng W, Shu L, Li Q, Chen S, Wang F, Tao XM. Fiber-based wearable electronics: A review of materials, fabrication, devices, and applications. *Adv Mater*. 2014;26(31):5310-5336. doi:10.1002/adma.201400633.

60. Atwa Y, Maheshwari N, Goldthorpe IA. Silver nanowire coated threads for electrically conductive textiles. *J Mater Chem C*. 2015;3(16):3908-3912. doi:10.1039/C5TC00380F.

61. Stoppa M, Chiolerio A. Wearable electronics and smart textiles: A critical review. *Sensors (Switzerland)*. 2014;14(7):11957-11992. doi:10.3390/s140711957.

62. Avloni J, Ouyang M, Florio L, Henn AR, Sparavigna A. Shielding effectiveness evaluation of metallized and polypyrrole-coated fabrics. *J Thermoplast Compos Mater*. 2007;20(3):241-254. doi:10.1177/0892705707076718.

63. Liu H, Zhu L li, He Y, Cheng B wen. A novel method for fabricating elastic conductive polyurethane filaments by in-situ reduction of polydopamine and electroless silver plating. *Mater Des*. 2017;113:254-263. doi:10.1016/j.matdes.2016.10.027.

64. Kaushik V, Lee J, Hong J, et al. Textile-Based Electronic Components for Energy Applications: Principles, Problems, and Perspective. *Nanomaterials*. 2015;5(3):1493-1531. doi:10.3390/nano5031493.

65. Hu L, Pasta M, La Mantia F, et al. Stretchable, porous, and conductive energy textiles. *Nano Lett*. 2010;10(2):708-714. doi:10.1021/nl903949m.

66. Hu X, Tian M, Qu L, Zhu S, Han G. Multifunctional cotton fabrics with graphene/polyurethane coatings with far-infrared emission, electrical conductivity, and ultraviolet-blocking properties. *Carbon N Y*. 2015;95:625-633. doi:10.1016/j.carbon.2015.08.099.

67. Cai G, Xu Z, Yang M, Tang B, Wang X. Applied Surface Science Functionalization of cotton fabrics through thermal reduction of graphene oxide. *Appl Surf Sci*. 2017;393:441-448. doi:10.1016/j.apsusc.2016.10.046.

68. Cataldi P, Ceseracciu L, Athanassiou A, Bayer IS. Healable Cotton-Graphene Nanocomposite Conductor for Wearable Electronics. *ACS Appl Mater Interfaces*. 2017;9(16):13825-13830. doi:10.1021/acsami.7b02326.

69. Shirakawa H, Louis J, Macdiarmid AG. Synthesis of Electrically Conducting Organic Polymers : Halogene Derivatives of Polyacetylene, (CH)x. *J C S Chem Comm*. 1977;(578):578-580. doi:10.1039/C39770000578.

70. Stenger-Smith JD. Intrinsically electrically conducting polymers. Synthesis, characterization, and their applications. *Prog Polym Sci*. 1998;23(1):57-79. doi:10.1016/S0079-6700(97)00024-5.

71. Kutanis S, Karakişla M, Akbulut U, Saçak M. The conductive polyaniline/poly(ethylene terephthalate) composite fabrics. *Compos Part A Appl Sci Manuf*. 2007;38(2):609-614. doi:10.1016/j.compositesa.2006.02.008.

72. Tang X, Tian M, Qu L, et al. A facile fabrication of multifunctional knit polyester fabric based on chitosan and polyaniline polymer nanocomposite. *Appl Surf Sci*. 2014;317:505-510. doi:10.1016/j.apsusc.2014.08.105.

73. Kumar J, Takagi H, Norio A, Ram D, Ahn S. Composites : Part B An overview on the cellulose based conducting composites. 2012;43:2822-2826. doi:10.1016/j.compositesb.2012.04.045.

74. Li Y, Leung MY, Tao XM, Cheng XY, Tsang J, Yuen MCW. Polypyrrole-coated conductive fabrics as a candidate for strain sensors. *J Mater Sci*. 2005;40(15):4093-4095. doi:10.1007/s10853-005-0791-8.

75. Ding Y, Invernale MA, Sotzing GA. Conductivity trends of pedot-pss impregnated fabric and the effect of conductivity on electrochromic textile. *ACS Appl Mater Interfaces*. 2010;2(6):1588-1593. doi:10.1021/am100036n.

76. Choi CM, Kwon SN, Na SI. Conductive PEDOT:PSS-coated poly-paraphenylene terephthalamide thread for highly durable electronic textiles. *J Ind Eng Chem*. 2017;50(2016):155-161. doi:10.1016/j.jiec.2017.02.009.

77. Kirihara K, Wei Q, Mukaida M, Ishida T. Thermoelectric power generation using nonwoven fabric module impregnated with conducting polymer PEDOT:PSS. *Synth Met*. 2017;225:41-48. doi:10.1016/j.synthmet.2017.01.001.

78. Alhashmi Alamer F. A simple method for fabricating highly electrically conductive cotton fabric without metals or nanoparticles, using PEDOT:PSS. *J Alloys Compd*. 2017;702:266-273. doi:10.1016/j.jallcom.2017.01.001.

79. Moraes MR, Alves AC, Toptan F, et al. Glycerol/PEDOT:PSS coated woven fabric as a flexible heating element on textiles. *J Mater Chem C*. 2017;5(15):3807-3822. doi:10.1039/C7TC00486A.

80. Yeon C, Kim G, Lim JW, Yun SJ. Highly conductive PEDOT:PSS treated by sodium dodecyl sulfate for stretchable fabric heaters. *RSC Adv*. 2017;7(10):5888-5897. doi:10.1039/C6RA24749K.

81. Kirchmeyer S, Reuter K. Scientific importance, properties and growing applications of poly(3,4-ethylenedioxythiophene). *J Mater Chem*. 2005;15(21):2077. doi:10.1039/b417803n.

82. Rivnay J, Owens RM, Malliaras GG. The rise of organic bioelectronics. *Chem Mater*. 2014;26(1):679-685. doi:10.1021/cm4022003.

83. Na S-I, Wang G, Kim S-S, et al. Evolution of nanomorphology and anisotropic conductivity in solvent-modified PEDOT:PSS films for polymeric anodes of polymer solar cells. *J Mater Chem*. 2009;19(47):9045. doi:10.1039/b915756e.

84. Mengistie DA, Ibrahem MA, Wang PC, Chu CW. Highly conductive PEDOT:PSS treated with formic acid for ITO-free polymer solar cells. *ACS Appl Mater Interfaces*. 2014;6(4):2292-2299. doi:10.1021/am405024d.

85. Alemu Mengistie D, Wang P-C, Chu C-W. Effect of molecular weight of additives on the conductivity of PEDOT:PSS and efficiency for ITO-free organic solar cells. *J Mater Chem A*. 2013;1(34):9907. doi:10.1039/c3ta11726j.

86. Chang SH, Chiang CH, Kao FS, Tien CL, Wu CG. Unraveling the Enhanced Electrical Conductivity of PEDOT:PSS Thin Films for ITO-Free Organic Photovoltaics. *IEEE Photonics J*. 2014;6(4). doi:10.1109/JPHOT.2014.2331254.

87. Calvert P, Duggal D, Patra P, Agrawal A, Sawhney A. Conducting Polymer and Conducting Composite Strain Sensors on Textiles. *Mol Cryst Liq Cryst*. 2008;484(1):291/[657]-302/[668]. doi:10.1080/15421400801904690.

88. Opwis K, Knittel D, Gutmann JS. Oxidative in situ deposition of conductive PEDOT:PTSA on textile substrates

and their application as textile heating element. *Synth Met*. 2012;162(21-22):1912-1918. doi:10.1016/j.synthmet.2012.08.007.

89. Du Y, Cai K, Chen S, et al. Thermoelectric Fabrics: Toward Power Generating Clothing. *Sci Rep*. 2015;5(1):6411. doi:10.1038/srep06411.

90. Mochizuki Y, Horii T, Okuzaki H. Effect of pH on Structure and Conductivity of PEDOT / PSS. *Trans Mater Res Soc Japan*. 2012;310:307-310.

91. Shi H, Liu C, Jiang Q, Xu J. Effective Approaches to Improve the Electrical Conductivity of PEDOT:PSS: A Review. *Adv Electron Mater*. 2015;1(4):1-16. doi:10.1002/aelm.201500017.

92. Huang Y-B, Fu Y. Hydrolysis of cellulose to glucose by solid acid catalysts. *Green Chem*. 2013;15(5):1095. doi:10.1039/c3gc40136g.

93. Mattana G, Cosseddu P, Fraboni B, Malliaras GG, Hinestroza JP, Bonfiglio A. Organic electronics on natural cotton fibres. *Org Electron physics, Mater Appl*. 2011;12(12):2033-2039. doi:10.1016/j.orgel.2011.09.001.

94. Hu B, Li D, Manandharm P, Fan Q, Kasilingam D, Calvert P. CNT/conducting polymer composite conductors impart high flexibility to textile electroluminescent devices. *J Mater Chem*. 2012;22(4):1598-1605. doi:10.1039/C1JM14121J.

95. Tian M, Hu X, Qu L, Zhu S, Sun Y, Han G. Versatile and ductile cotton fabric achieved via layer-by-layer self-assembly by consecutive adsorption of graphene doped PEDOT: PSS and chitosan. *Carbon N Y*. 2016;96:1166-1174. doi:10.1016/j.carbon.2015.10.080.

96. Shaheen TI, El-Naggar ME, Abdelgawad AM, Hebeish A. Durable antibacterial and UV protections of in situ synthesized zinc oxide nanoparticles onto cotton fabrics. *Int J Biol Macromol*. 2016;83:426-432. doi:10.1016/j.ijbiomac.2015.11.003.

97. Mishra A, Butola BS. Deposition of Ag doped TiO2 on cotton fabric for wash durable UV protective and antibacterial properties at very low silver concentration. *Cellulose*. 2017:1-17. doi:10.1007/s10570-017-1352-4.

98. Wu D, Long M. Realizing visible-light-induced self-cleaning property of cotton through coating N-TiO 2 film and loading AgI particles. *ACS Appl Mater Interfaces*. 2011;3(12):4770-4774. doi:10.1021/am201251d.

99. Pasqui D, Barbucci R. Synthesis, characterization and self cleaning properties of titania nanoparticles grafted on polyester fabrics. *J Photochem Photobiol A Chem*. 2014;274:1-6. doi:10.1016/j.jphotochem.2013.08.017.

100. Balakumaran MD, Ramachandran R, Jagadeeswari S, Kalaichelvan PT. In vitro biological properties and characterization of nanosilver coated cotton fabrics - An application for antimicrobial textile finishing. *Int Biodeterior Biodegrad*. 2016;107:48-55. doi:10.1016/j.ibiod.2015.11.011.

101. Velmurugan P, Shim J, Bang KS, Oh BT. Gold nanoparticles mediated coloring of fabrics and leather for antibacterial activity. *J Photochem Photobiol B Biol*. 2016;160:102-109. doi:10.1016/j.jphotobiol.2016.03.051.

102. Yang J, Xu H, Zhang L, Zhong Y, Sui X, Mao Z. Lasting superhydrophobicity and antibacterial activity of Cu nanoparticles immobilized on the surface of dopamine modified cotton fabrics. *Surf Coatings Technol*. 2017;309:149-154. doi:10.1016/j.surfcoat.2016.11.058.

103. Hussain SM, Hess KL, Gearhart JM, Geiss KT, Schlager JJ. In vitro toxicity of nanoparticles in BRL 3A rat liver cells. *Toxicol Vitr*. 2005;19(7):975-983. doi:10.1016/j.tiv.2005.06.034.

104. Kulthong K, Srisung S, Boonpavanitchakul K, Kangwansupamonkon W, Maniratanachote R. Determination of silver nanoparticle release from antibacterial fabrics into artificial sweat. *Part Fibre Toxicol*. 2010;7(1):8. doi:10.1186/1743-8977-7-8.

105. Celá P, Veselá B, Matalová E, Večeřa Z, Buchtová M. Embryonic toxicity of nanoparticles. *Cells Tissues*

Organs. 2014;199(1):1-23. doi:10.1159/000362163.

106. Perelshtein I, Applerot G, Perkas N, Grinblat J, Gedanken A. A one-step process for the antimicrobial finishing of textiles with crystalline TiO 2 nanoparticles. *Chem - A Eur J*. 2012;18(15):4575-4582. doi:10.1002/chem.201101683.

107. Aksit A, Onar Camlibel N, Topel Zeren E, Kutlu B. Development of antibacterial fabrics by treatment with Ag-doped TiO $_2$ nanoparticles. *J Text Inst*. 2017;5000(April):1-11. doi:10.1080/00405000.2017.1311766.

108. Zaleska A. Doped-TiO 2 : A Review. *Recent Patents Eng 2008, 2, 157-164*. 2008;(1):157-164. doi:1872-2121/08.

109. Hoffmann MR, Martin ST, Choi W, Bahnemann DW. Environmental Applications of Semiconductor Photocatalysis. *Chem Rev*. 1995;95(1):69-96. doi:10.1021/cr00033a004.

110. Fujishima A, Rao TN, Tryk DA. Titanium dioxide photocatalysis. *J Photochem Photobiol C Photochem Rev*. 2000;1(1):1-21. doi:10.1016/S1389-5567(00)00002-2.

111. Senić Ž, Bauk S, Vitorović-Todorović M, Pajić N, Samolov A, Rajić D. Application of TiO 2 Nanoparticles for Obtaining Self- Decontaminating Smart Textiles. *Sci Tech Rev*. 2011;61(4):63-72.

112. Vorontsov A V., Lion C, Savinov EN, Smirniotis PG. Pathways of photocatalytic gas phase destruction of HD simulant 2-chloroethyl ethyl sulfide. *J Catal*. 2003;220(2):414-423. doi:10.1016/S0021-9517(03)00293-8.

113. Dong Y, Bai Z, Liu R, Zhu T. Preparation of fibrous TiO2 photocatalyst and its optimization towards the decomposition of indoor ammonia under illumination. *Catal Today*. 2007;126(3-4 SPEC. ISS.):320-327. doi:10.1016/j.cattod.2007.06.034.

114. Uyguner-Demirel CS, Birben NC, Bekbolet M. Elucidation of background organic matter matrix effect on photocatalytic treatment of contaminants using TiO2: A review. *Catal Today*. 2017;284:202-214. doi:10.1016/j.cattod.2016.12.030.

115. Zhao Z, Liu Q. Mechanism of higher photocatalytic activity of anatase TiO $_2$ doped with nitrogen under visible-light irradiation from density functional theory calculation. *J Phys D Appl Phys*. 2008;41(2):25105. doi:10.1088/0022-3727/41/2/025105.

116. Dong H, Zeng G, Tang L, et al. An overview on limitations of TiO<inf>2</inf>-based particles for photocatalytic degradation of organic pollutants and the corresponding countermeasures. *Water Res*. 2015;79:128-146. doi:10.1016/j.watres.2015.04.038.

117. Zhang X, Wang DK, Diniz Da Costa JC. Recent progresses on fabrication of photocatalytic membranes for water treatment. *Catal Today*. 2014;230:47-54. doi:10.1016/j.cattod.2013.11.019.

118. Gaminian H, Montazer M. Enhanced Self-Cleaning Properties on Polyester Fabric under Visible Light Through Single-Step Synthesis of Cuprous Oxide Doped Nano-TiO<inf>2</inf>. *Photochem Photobiol*. 2015;91(5):1078-1087. doi:10.1111/php.12478.

119. Rana M, Hao B, Mu L, Chen L, Ma PC. Development of multi-functional cotton fabrics with Ag/AgBr-TiO2 nanocomposite coating. *Compos Sci Technol*. 2016;122:104-112. doi:10.1016/j.compscitech.2015.11.016.

120. Khani A, Talebian N. In vitro bactericidal effect of ultrasonically sol–gel-coated novel CuO/TiO2/PEG/cotton nanocomposite for wound care. *J Coatings Technol Res*. 2017;14(3):651-663. doi:10.1007/s11998-016-9870-9.

121. Uddin MJ, Cesano F, Scarano D, et al. Cotton textile fibres coated by Au/TiO2 films: Synthesis, characterization and self cleaning properties. *J Photochem Photobiol A Chem*. 2008;199(1):64-72. doi:10.1016/j.jphotochem.2008.05.004.

122. Nica I, Stan M, Dinischiotu A, et al. Innovative Self-Cleaning and Biocompatible Polyester Textiles Nano-

Decorated with Fe–N-Doped Titanium Dioxide. *Nanomaterials*. 2016;6(11):214. doi:10.3390/nano6110214.

123. Xue C-H, Bai X, Jia S-T. Robust, Self-Healing Superhydrophobic Fabrics Prepared by One-Step Coating of PDMS and Octadecylamine. *Sci Rep*. 2016;6(1):27262. doi:10.1038/srep27262.

124. Wang H, Xue Y, Ding J, Feng L, Wang X, Lin T. Durable, self-healing superhydrophobic and superoleophobic surfaces from fluorinated-decyl polyhedral oligomeric silsesquioxane and hydrolyzed fluorinated alkyl silane. *Angew Chemie - Int Ed*. 2011;50(48):11433-11436. doi:10.1002/anie.201105069.

125. Szostak-Kotowa J. Biodeterioration of textiles. *Int Biodeterior Biodegrad*. 2004;53(3):165-170. doi:10.1016/S0964-8305(03)00090-8.

126. Vasiljević J, Gorjanc M, Tomšič B, et al. The surface modification of cellulose fibres to create super-hydrophobic, oleophobic and self-cleaning properties. *Cellulose*. 2013;20(1):277-289. doi:10.1007/s10570-012-9812-3.

127. Bae GY, Min BG, Jeong YG, Lee SC, Jang JH, Koo GH. Superhydrophobicity of cotton fabrics treated with silica nanoparticles and water-repellent agent. *J Colloid Interface Sci*. 2009;337(1):170-175. doi:10.1016/j.jcis.2009.04.066.

128. Aslanidou D, Karapanagiotis I, Panayiotou C. Superhydrophobic, superoleophobic coatings for the protection of silk textiles. *Prog Org Coatings*. 2016;97:44-52. doi:10.1016/j.porgcoat.2016.03.013.

129. Yoshimitsu Z, Nakajima A, Watanabe T, Hashimoto K. Effects of surface structure on the hydrophobicity and sliding behavior of water droplets. *Langmuir*. 2002;18(15):5818-5822. doi:10.1021/la020088p.

130. Liu F, Ma M, Zang D, Gao Z, Wang C. Fabrication of superhydrophobic/superoleophilic cotton for application in the field of water/oil separation. *Carbohydr Polym*. 2014;103(1):480-487. doi:10.1016/j.carbpol.2013.12.022.

131. Xu L, Zhuang W, Xu B, Cai Z. Fabrication of superhydrophobic cotton fabrics by silica hydrosol and hydrophobization. *Appl Surf Sci*. 2011;257(13):5491-5498. doi:10.1016/j.apsusc.2010.12.116.

132. Subhash Latthe S, Basavraj Gurav A, Shridhar Maruti C, Shrikant Vhatkar R. Recent Progress in Preparation of Superhydrophobic Surfaces: A Review. *J Surf Eng Mater Adv Technol*. 2012;2(2):76-94. doi:10.4236/jsemat.2012.22014.

133. Yin Y, Huang R, Zhang W, Zhang M, Wang C. Superhydrophobic-superhydrophilic switchable wettability via TiO2 photoinduction electrochemical deposition on cellulose substrate. *Chem Eng J*. 2016;289:99-105. doi:10.1016/j.cej.2015.12.049.

134. Yang SH, Liu CH, Hsu WT, Chen H. Preparation of super-hydrophobic films using pulsed hexafluorobenzene plasma. *Surf Coatings Technol*. 2009;203(10-11):1379-1383. doi:10.1016/j.surfcoat.2008.11.007.

135. Jiang Y, Wang Z, Yu X, et al. Self-assembled monolayers of dendron thiols for electrodeposition of gold nanostructures: Toward fabrication of superhydrophobic/superhydrophilic surfaces and pH-responsive surfaces. *Langmuir*. 2005;21(5):1986-1990. doi:10.1021/la047491b.

136. Gao Q, Zhu Q, Guo Y, Yang CQ. Formation of highly hydrophobic surfaces on cotton and polyester fabrics using silica sol nanoparticles and nonfluorinated alkylsilane. *Ind Eng Chem Res*. 2009;48(22):9797-9803. doi:10.1021/ie9005518.

137. Liu H, Gao SW, Cai JS, et al. Recent progress in fabrication and applications of superhydrophobic coating on cellulose-based substrates. *Materials (Basel)*. 2016;9(3):1-37. doi:10.3390/ma9030124.

138. Zhao Y, Wang H, Zhou H, Lin T. Directional Fluid Transport in Thin Porous Materials and its Functional Applications. *Small*. 2017;13(4):1-22. doi:10.1002/smll.201601070.

139. Ceseracciu L, Heredia-Guerrero JA, Dante S, Athanassiou A, Bayer IS. Robust and biodegradable elastomers

based on corn starch and polydimethylsiloxane (PDMS). *ACS Appl Mater Interfaces*. 2015;7(6):3742-3753. doi:10.1021/am508515z.

140. Horcas I, Fernández R, Gómez-Rodríguez JM, Colchero J, Gómez-Herrero J, Baro AM. WSXM: A software for scanning probe microscopy and a tool for nanotechnology. *Rev Sci Instrum*. 2007;78(1). doi:10.1063/1.2432410.
141. McArthur SL. Thin films of Vanadium Oxide Grown on Vanadium metal. *Surf Interface Anal*. 2006;38(c):1380-1385. doi:10.1002/sia.
142. Zimmermann J, Seeger S, Reifler FA. Water Shedding Angle: A New Technique to Evaluate the Water-Repellent Properties of Superhydrophobic Surfaces. *Text Res J*. 2009;79(17):1565-1570. doi:10.1177/0040517509105074.
143. Rykaczewski K, Osborn WA, Chinn J, et al. How nanorough is rough enough to make a surface superhydrophobic during water condensation? *Soft Matter*. 2012;8(33):8786. doi:10.1039/c2sm25502b.
144. Garside P, Wyeth P. Identification of Cellulosic Fibres by FTIR Spectroscopy. *Stud Conserv*. 2003;48(4):269-275. doi:10.1179/sic.2003.48.4.269.
145. Davis A, Mele E, Heredia-Guerrero JA, Bayer IS, Athanassiou A. Omniphobic nanocomposite fiber mats with peel-away self similarity. *J Mater Chem A*. 2015;3(47):23821-23828. doi:10.1039/c5ta06333g.
146. Saikia BJ, Parthasarathy G, Sarmah NC. Fourier transform infrared spectroscopic estimation of crystallinity in SiO 2 based rocks. 2008;31(5):775-779.
147. Stana-Kleinschek K, Strnad S, Ribitsch V. Surface characterization and adsorption abilities of cellulose fibers. *Polym Eng Sci*. 1999;39(8):1412-1424. doi:10.1002/pen.11532.
148. Hoefnagels HF, Wu D, De With G, Ming W. Biomimetic superhydrophobic and highly oleophobic cotton textiles. *Langmuir*. 2007;23(26):13158-13163. doi:10.1021/la702174x.
149. Michielsen S, Lee HJ, Carolina N. Design of a Superhydrophobic Surface Using Woven Structures Design of a Superhydrophobic Surface Using Woven Structures. *Langmuir*. 2007;23(11):6004-6010. doi:10.1021/la063157z.
150. Gao N, Yan Y. Modeling Superhydrophobic Contact Angles and Wetting Transition. *J Bionic Eng*. 2009;6(4):335-340. doi:10.1016/S1672-6529(08)60135-3.
151. Xu B, Cai Z, Wang W, Ge F. Preparation of superhydrophobic cotton fabrics based on SiO2 nanoparticles and ZnO nanorod arrays with subsequent hydrophobic modification. *Surf Coatings Technol*. 2010;204(9-10):1556-1561. doi:10.1016/j.surfcoat.2009.09.086.
152. Mates JE, Schutzius TM, Bayer IS, Qin J, Waldroup DE, Megaridis CM. Water-based superhydrophobic coatings for nonwoven and cellulosic substrates. *Ind Eng Chem Res*. 2014;53(1):222-227. doi:10.1021/ie402836x.
153. Gibson P. Water-repellent Treatment on Military Uniform Fabrics: Physiological and Comfort Implications. *J Ind Text*. 2008;38(1):43-54. doi:10.1177/1528083707087833.
154. Gallego-Juarez JA, Riera E, Acosta V, Rodríguez G, Blanco A. Ultrasonic system for continuous washing of textiles in liquid layers. *Ultrason Sonochem*. 2010;17(1):234-238. doi:10.1016/j.ultsonch.2009.06.005.
155. Choi J, Kim TH, Kim HY, Kim W. Ultrasonic washing of textiles. *Ultrason Sonochem*. 2016;29:563-567. doi:10.1016/j.ultsonch.2015.07.018.
156. Durville D. Simulation of the mechanical behaviour of woven fabrics at the scale of fibers. *Int J Mater Form*. 2010;3(SUPPL. 2):1241-1251. doi:10.1007/s12289-009-0674-7.

157. Kendall K, Fuller KNG. J-shaped stress/strain curves and crack resistance of biological materials. *J Phys D Appl Phys*. 1987;20(12):1596-1600. doi:10.1088/0022-3727/20/12/008.

158. Hirokazu MI. A Multi-Step Linear Approximation Method for Nonlinear Analysis of Stress and Deformation of Coated Plain-Weave Fabric. 2006;52(5):189-195.

159. Galliot C, Luchsinger RH. Non-linear properties of PVC-coated fabrics used in Tensairity structures C3 - ICCM International Conferences on Composite Materials. *17th Int Conf Compos Mater ICCM-17*. 2009;(January). http://www.scopus.com/inward/record.url?eid=2-s2.0-80052074174&partnerID=40&md5=75c3ac5ec05f43d159148ed7fe8dda2f.

160. Grosberg P. TEXTILE The Mechanical Properties of Woven Fabrics. *Text Res J*. 1966:205-211. doi:10.1177/004051756603600301.

161. Cao C, Ge M, Huang J, et al. Robust fluorine-free superhydrophobic PDMS–ormosil@fabrics for highly effective self-cleaning and efficient oil–water separation. *J Mater Chem A*. 2016;4(31):12179-12187. doi:10.1039/C6TA04420D.

162. Yadav A, Prasad V, Kathe AA, et al. Functional finishing in cotton fabrics using zinc oxide nanoparticles. *Bull Mater Sci*. 2006;29(6):641–645. doi:10.1007/s12034-006-0017-y.

163. Tao X, Koncar V, Dufour C. Geometry Pattern for the Wire Organic Electrochemical Textile Transistor. *J Electrochem Soc*. 2011;158(5):H572. doi:10.1149/1.3562962.

164. Hansora DP, Shimpi NG, Mishra S. Performance of hybrid nanostructured conductive cotton materials as wearable devices: an overview of materials, fabrication, properties and applications. *RSC Adv*. 2015;5(130):107716-107770. doi:10.1039/C5RA16478H.

165. Wang YL, Rouabhia M, Zhang Z. PPy-coated PET fabrics and electric pulse-stimulated fibroblasts. *J Mater Chem B*. 2013;1(31):3789-3796. doi:Doi 10.1039/C3tb20257g.

166. Akerfeldt M, Straat M, Walkenstrom P. Electrically conductive textile coating with a PEDOT-PSS dispersion and a polyurethane binder. *Text Res J*. 2012;83:618-627. doi:10.1177/0040517512444330.

167. Groenendaal BL, Jonas F, Freitag D, Pielartzik H, Reynolds JR. Its Derivatives : Past , Present , and Future **. 2000:481-494. doi:10.1144/GSL.SP.2000.173.01.01.

168. Liu S, Hu M, Yang J. A facile way of fabricating flexible and conductive cotton fabric. *J Mater Chem C*. 2016;4:1320-1325. doi:10.1039/C5TC03679H.

169. Cataldi P, Bayer IS, Nanni G, et al. Effect of graphene nano-platelet morphology on the elastic modulus of soft and hard biopolymers. *Carbon N Y*. 2016;109:331-339. doi:10.1016/j.carbon.2016.08.026.

170. Tran TN, Paul U, Heredia-Guerrero JA, et al. Transparent and flexible amorphous cellulose-acrylic hybrids. *Chem Eng J*. 2016;287:196-204. doi:10.1016/j.cej.2015.10.114.

171. Heredia-Guerrero JA, Benítez JJ, Cataldi P, et al. All-Natural Sustainable Packaging Materials Inspired by Plant Cuticles. *Adv Sustain Syst*. 2017;1(1-2):1600024. doi:10.1002/adsu.201600024.

172. Rantanen J, Impiö J, Karinsalo T, et al. Smart clothing prototype for the arctic environment. *Pers Ubiquitous Comput*. 2002;6(1):3-16. doi:10.1007/s007790200001.

173. Jost K, Perez CR, McDonough JK, et al. Carbon coated textiles for flexible energy storage. *Energy Environ Sci*. 2011;4(12):5060. doi:10.1039/c1ee02421c.

174. Cataldi P, Ceseracciu L, Marras S, Athanassiou A, Bayer IS. Electrical conductivity enhancement in thermoplastic polyurethane-graphene nanoplatelet composites by stretch-release cycles. *Appl Phys Lett*. 2017;110(12):3-8. doi:10.1063/1.4978865.

175. Cataldi P, Bayer IS, Bonaccorso F, Pellegrini V, Athanassiou A, Cingolani R. Foldable Conductive Cellulose Fiber Networks Modified by Graphene Nanoplatelet-Bio-Based Composites. *Adv Electron Mater*. 2015;1(12):1-8. doi:10.1002/aelm.201500224.

176. Duchemin BJC. Mercerisation of cellulose in aqueous NaOH at low concentrations. *Green Chem*. 2015;17(7):3941-3947. doi:10.1039/C5GC00563A.

177. Kovacik P, Hierro G Del, Livernois W, Gleason KK. Scale-up of oCVD: large-area conductive polymer thin films for next-generation electronics. *Mater Horizons*. 2015;2:221-227. doi:10.1039/C4MH00222A.

178. Keshk SMAS, Hamdy MS, Badr IHA. Physicochemical Characterization of Mercerized Cellulose / TiO 2 Nano-Composite. *Am J Polym Sci*. 2015;5(1):24-29. doi:10.5923/j.ajps.20150501.04.

179. Eronen P, Österberg M, Jääskeläinen AS. Effect of alkaline treatment on cellulose supramolecular structure studied with combined confocal Raman spectroscopy and atomic force microscopy. *Cellulose*. 2009;16(2):167-178. doi:10.1007/s10570-008-9259-8.

180. Lindfors T, Boeva ZA, Latonen R-M. Electrochemical synthesis of poly(3,4-ethylenedioxythiophene) in aqueous dispersion of high porosity reduced graphene oxide. *RSC Adv*. 2014;4(48):25279-25286. doi:10.1039/C4RA03423F.

181. Selvaganesh SV, Mathiyarasu J, Phani KLN, Yegnaraman V. Chemical synthesis of PEDOT-Au nanocomposite. *Nanoscale Res Lett*. 2007;2(11):546-549. doi:10.1007/s11671-007-9100-6.

182. Teng C, Lu X, Ren G, Zhu Y, Wan M, Jiang L. Underwater Self-Cleaning PEDOT-PSS Hydrogel Mesh for Effective Separation of Corrosive and Hot Oil/Water Mixtures. *Adv Mater Interfaces*. 2014;1(6). doi:10.1002/admi.201400099.

183. Wang G, Yang J, Park J, et al. Facile synthesis and characterization of graphene nanosheets. *Phys Chem C*. 2008;112(22):8192-8195. doi:10.1021/jp710931h.

184. Ferrari AC, Meyer JC, Scardaci V, et al. Raman spectrum of graphene and graphene layers. *Phys Rev Lett*. 2006;97(18):1-4. doi:10.1103/PhysRevLett.97.187401.

185. Credou J, Berthelot T. Cellulose: from biocompatible to bioactive material. *J Mater Chem B*. 2014;2(30):4767-4788. doi:10.1039/C4TB00431K.

186. Eng JTS, Perumalraj R. Electrical Surface Resistivity of Polyaniline Coated Woven Fabrics. *J Text Sci Eng*. 2015;5(3). doi:10.4172/2165-8064.1000196.

187. Stöcker T, Köhler A, Moos R. Why does the electrical conductivity in PEDOT:PSS decrease with PSS content? A study combining thermoelectric measurements with impedance spectroscopy. *J Polym Sci Part B Polym Phys*. 2012;50(14):976-983. doi:10.1002/polb.23089.

188. Li J, Liu JC, Gao CJ. On the mechanism of conductivity enhancement in PEDOT/PSS film doped with multi-walled carbon nanotubes. *J Polym Res*. 2010;17(5):713-718. doi:10.1007/s10965-009-9360-1.

189. Futaba DN, Hata K, Yamada T, et al. Shape-engineerable and highly densely packed single-walled carbon nanotubes and their application as super-capacitor electrodes. *Nat Mater*. 2006;5(12):987-994. doi:10.1038/nmat1782.

190. Vosgueritchian M, Lipomi DJ, Bao Z. Highly conductive and transparent PEDOT:PSS films with a fluorosurfactant for stretchable and flexible transparent electrodes. *Adv Funct Mater*. 2012;22(2):421-428. doi:10.1002/adfm.201101775.

191. Suchand Sangeeth CS, Jaiswal M, Menon R. Correlation of morphology and charge transport in poly(3,4-ethylenedioxythiophene)-polystyrenesulfonic acid (PEDOT-PSS) films. *J physics Condens Matter*.

2009;21(7):72101. doi:10.1088/0953-8984/21/7/072101.

192. Pasha A, Roy AS, Murugendrappa M V., Al-Hartomy OA, Khasim S. Conductivity and dielectric properties of PEDOT-PSS doped DMSO nano composite thin films. *J Mater Sci Mater Electron*. 2016;27(8):8332-8339. doi:10.1007/s10854-016-4842-5.

193. Li Y, Cheng XY, Leung MY, Tsang J, Tao XM, Yuen MCW. A flexible strain sensor from polypyrrole-coated fabrics. *Synth Met*. 2005;155(1):89-94. doi:10.1016/j.synthmet.2005.06.008.

194. Wu J, Zhou D, Too CO, Wallace GG. Conducting polymer coated lycra. *Synth Met*. 2005;155(3):698-701. doi:10.1016/j.synthmet.2005.08.032.

195. Wu Q, Hu J. Waterborne polyurethane based thermoelectric composites and their application potential in wearable thermoelectric textiles. *Compos Part B Eng*. 2016;107:59-66. doi:10.1016/j.compositesb.2016.09.068.

196. Biener J, Stadermann M, Suss M, et al. Advanced carbon aerogels for energy applications. *Energy Environ Sci*. 2011;4(3):656. doi:10.1039/c0ee00627k.

197. Yun TG, Hwang B Il, Kim D, Hyun S, Han SM. Polypyrrole-MnO<inf>2</inf>-coated textile-based flexible-stretchable supercapacitor with high electrochemical and mechanical reliability. *ACS Appl Mater Interfaces*. 2015;7(17):9228-9234. doi:10.1021/acsami.5b01745.

198. Cheng Q, Tang J, Ma J, Zhang H, Shinya N, Qin L-C. Graphene and carbon nanotube composite electrodes for supercapacitors with ultra-high energy density. *Phys Chem Chem Phys*. 2011;13(39):17615. doi:10.1039/c1cp21910c.

199. Binas VD, Sambani K, Maggos T, Katsanaki A, Kiriakidis G. Synthesis and photocatalytic activity of Mn-doped TiO2 nanostructured powders under UV and visible light. *Appl Catal B Environ*. 2012;113-114:79-86. doi:10.1016/j.apcatb.2011.11.021.

200. Wiegand C, Abel M, Ruth P, Elsner P, Hipler UC. In vitro assessment of the antimicrobial activity of wound dressings: influence of the test method selected and impact of the pH. *J Mater Sci Mater Med*. 2015;26(1):5343. doi:10.1007/s10856-014-5343-9.

201. Barani H, Montazer M, Samadi N, Toliyat T. Nano silver entrapped in phospholipids membrane: synthesis, characteristics and antibacterial kinetics. *Mol Membr Biol*. 2011;28(4):206-215. doi:10.3109/09687688.2011.565484.

202. Zahid M, Heredia-Guerrero JA, Athanassiou A, Bayer IS. Robust water repellent treatment for woven cotton fabrics with eco-friendly polymers. *Chem Eng J*. 2017;319:321-332. doi:10.1016/j.cej.2017.03.006.

203. Jagessar RC, Alleyne R. Antimicrobial Potency of the Aqueous Extract of Leaves of Terminalia Catappa. *Acad Res Int*. 2011;1(3):362-371. http://www.savap.org.pk/journals/ARInt./Vol.1(3)/2011(1.3-37).pdf.

204. Wu D, Long M, Zhou J, et al. Synthesis and characterization of self-cleaning cotton fabrics modified by TiO2 through a facile approach. *Surf Coatings Technol*. 2009;203(24):3728-3733. doi:10.1016/j.surfcoat.2009.06.008.

205. Hebeish AA, Abdelhady MM, Youssef AM. TiO2 nanowire and TiO2 nanowire doped Ag-PVP nanocomposite for antimicrobial and self-cleaning cotton textile. *Carbohydr Polym*. 2013;91(2):549-559. doi:10.1016/j.carbpol.2012.08.068.

206. Frunza L, Diamandescu L, Zgura I, et al. Photocatalytic activity of wool fabrics deposited at low temperature with ZnO or TiO2 nanoparticles: Methylene blue degradation as a test reaction. *Catal Today*. 2016. doi:10.1016/j.cattod.2017.02.044.

207. Ba-Abbad MM., Kadhum AAH., Mohamad AB., Takriff MS., Sopian K. Synthesis and catalytic activity of TiO

2 nanoparticles for photochemical oxidation of concentrated chlorophenols under direct solar radiation. *Int J Electrochem Sci*. 2012;7(6):4871-4888. http://www.scopus.com/inward/record.url?eid=2-s2.0-84862741634&partnerID=40&md5=023a2e49689851e247ea3d3d3ed555da.

208. Cabrales L, Abidi N, Manciu F. Characterization of Developing Cotton Fibers by Confocal Raman Microscopy. *Fibers*. 2014;2(4):285-294. doi:10.3390/fib2040285.

209. Atanasov PA, Nedyalkov NN, Valova EI, et al. Fs-laser processing of polydimethylsiloxane. *J Appl Phys*. 2014;116(2). doi:10.1063/1.4887812.

210. Khafaga MR, Ali HE, El-Naggar AWM. Antimicrobial finishing of cotton fabrics based on gamma irradiated carboxymethyl cellulose/poly(vinyl alcohol)/TiO 2 nanocomposites. *J Text Inst*. 2015;5000(December):1-8. doi:10.1080/00405000.2015.1061762.

211. Fu G, Vary PS, Lin C-T. Anatase TiO2 nanocomposites for antimicrobial coatings. *J Phys Chem B*. 2005;109(18):8889-8898. doi:10.1021/jp0502196.

212. Zhang H, Zhu H. Preparation of Fe-doped TiO 2 nanoparticles immobilized on polyamide fabric. *Appl Surf Sci*. 2012;258(24):10034-10041. doi:10.1016/j.apsusc.2012.06.069.

213. Solis KJ, Martin JE. Field-structured magnetic platelets as a route to improved thermal interface materials. *J Appl Phys*. 2012;111(7). doi:10.1063/1.3699013.

214. Hansson J, J Nilsson TM, Ye L, Liu J. Novel nanostructured thermal interface materials: a review. *Int Mater Rev*. 2016;0(April). doi:10.1080/09506608.2017.1301014.

215. Yu H, Li L, Zhang Y. Silver nanoparticle-based thermal interface materials with ultra-low thermal resistance for power electronics applications. *Scr Mater*. 2012;66(11):931-934. doi:10.1016/j.scriptamat.2012.02.037.

216. Narumanchi S, Mihalic M, Kelly K, Eesley G. Thermal interface materials for power electronics applications. *11th Intersoc Conf Therm Thermomechanical Phenom Electron Syst*. 2008:395-404. doi:10.1109/ITHERM.2008.4544297.

217. Moore GE. Creaming more components onto integrated circuits. *Electronics*. 1965;38(8):114-117. doi:10.1109/jproc.1998.658762.

218. Prasher R, Chiu C. Thermal Interface Materials. *Interface*. 2009;10(February):437-458. doi:10.1007/978-0-387-78219-5.

219. Otiaba KC, Ekere NN, Bhatti RS, Mallik S, Alam MO, Amalu EH. Thermal interface materials for automotive electronic control unit: Trends, technology and R&D challenges. *Microelectron Reliab*. 2011;51(12):2031-2043. doi:10.1016/j.microrel.2011.05.001.

220. Prasher RS, Shipley J, Prstic S, Koning P, Wang J. Thermal Resistance of Particle Laden Polymeric Thermal Interface Materials. *J Heat Transfer*. 2003;125(6):1170. doi:10.1115/1.1621893.

221. Barkoula NM, Alcock B, Cabrera NO, Peijs T. Fatigue properties of highly oriented polypropylene tapes and all-polypropylene composites. *Polym Polym Compos*. 2008;16(2):101-113. doi:10.1002/pc.

222. Ishida H, Rimdusit S. Very high thermal conductivity obtained by boron nitride-filled polybenzoxazine. *Thermochim Acta*. 1998;320(1-2):177-186. doi:10.1016/S0040-6031(98)00463-8.

223. Alm K, Kim K, Kim J. Fabrication of surface-treated BN/ETDS composites for enhanced thermal and mechanical properties. *Ceram Int*. 2015;41(8):9488-9495. doi:10.1016/j.ceramint.2015.04.006.

224. Lin Z, Liu Y, Raghavan S, Moon KS, Sitaraman SK, Wong CP. Magnetic alignment of hexagonal boron nitride platelets in polymer matrix: Toward high performance anisotropic polymer composites for electronic encapsulation. *ACS Appl Mater Interfaces*. 2013;5(15):7633-7640. doi:10.1021/am401939z.

225. Xu J, Munari A, Dalton E, Mathewson A, Razeeb KM. Silver nanowire array-polymer composite as thermal interface material. *J Appl Phys*. 2009;106(12):1-8. doi:10.1063/1.3271149.

226. Wang S, Cheng Y, Wang R, Sun J, Gao L. Highly thermal conductive copper nanowire composites with ultralow loading: Toward applications as thermal interface materials. *ACS Appl Mater Interfaces*. 2014;6(9):6481-6486. doi:10.1021/am500009p.

227. Balachander N, Seshadri I, Mehta RJ, et al. Nanowire-filled polymer composites with ultrahigh thermal conductivity Nanowire-filled polymer composites with ultrahigh thermal conductivity. 2014;93117(2013):1-6. doi:10.1063/1.4793419.

228. Razeeb KM, Roy S. Thermal diffusivity of nonfractal and fractal nickel nanowires. *J Appl Phys*. 2008;103(8). doi:10.1063/1.2906347.

229. Balandin AA. Thermal properties of graphene and nanostructured carbon materials. *Nat Mater*. 2011;10(8):569-581. doi:10.1038/nmat3064.

230. Hong W-T, Tai N-H. Investigations on the thermal conductivity of composites reinforced with carbon nanotubes. *Diam Relat Mater*. 2008;17(7-10):1577-1581. doi:10.1016/j.diamond.2008.03.037.

231. Jakubinek MB, White MA, Mu M, Winey KI. Temperature dependence of thermal conductivity enhancement in single-walled carbon nanotube/polystyrene composites. *Appl Phys Lett*. 2010;96(8):1-4. doi:10.1063/1.3323095.

232. Shahil KMF, Balandin AA. Graphene-multilayer graphene nanocomposites as highly efficient thermal interface materials. *Nano Lett*. 2012;12(2):861-867. doi:10.1021/nl203906r.

233. Tang B, Hu G, Gao H, Hai L. International Journal of Heat and Mass Transfer Application of graphene as filler to improve thermal transport property of epoxy resin for thermal interface materials. *Heat Mass Transf*. 2015;85:420-429. doi:10.1016/j.ijheatmasstransfer.2015.01.141.

234. Yu A, Ramesh P, Itkis ME, Bekyarova E, Haddon RC. Graphite nanoplatelet-epoxy composite thermal interface materials. *J Phys Chem C*. 2007;111(21):7565-7569. doi:10.1021/jp071761s.

235. Raza M a., a.V.K. Westwood, Stirling C. Graphite nanoplatelet/silicone composites for thermal interface applications. *2010 Int Symp Adv Packag Mater Microtech*. 2010:34-48. doi:10.1109/ISAPM.2010.5441382.

236. Uetani K, Ata S, Tomonoh S, Yamada T, Yumura M, Hata K. Elastomeric thermal interface materials with high through-plane thermal conductivity from carbon fiber fillers vertically aligned by electrostatic flocking. *Adv Mater*. 2014;26(33):5857-5862. doi:10.1002/adma.201401736.

237. Guzman-Puyol S, Ceseracciu L, Heredia-Guerrero JA, et al. Effect of trifluoroacetic acid on the properties of polyvinyl alcohol and polyvinyl alcohol-cellulose composites. *Chem Eng J*. 2015;277:242-251. doi:10.1016/j.cej.2015.04.092.

238. Bayer IS, Guzman-Puyol S, Heredia-Guerrero JA, et al. Direct transformation of edible vegetable waste into bioplastics. *Macromolecules*. 2014;47(15):5135-5143. doi:10.1021/ma5008557.

239. Guzman-Puyol S, Heredia-Guerrero JA, Ceseracciu L, et al. Low-Cost and Effective Fabrication of Biocompatible Nanofibers from Silk and Cellulose-Rich Materials. *ACS Biomater Sci Eng*. 2016;2(4):526-534. doi:10.1021/acsbiomaterials.5b00500.

240. Guzman-Puyol S, Russo D, Penna I, et al. Facile production of seaweed-based biomaterials with antioxidant and anti-inflammatory activities. *Algal Res*. 2017;27(February):1-11. doi:10.1016/j.algal.2017.08.015.

241. Cataldi P, Bayer IS, Nanni G, et al. Effect of graphene nano-platelet morphology on the elastic modulus of soft and hard biopolymers. *Carbon N Y*. 2016;109:331-339. doi:10.1016/j.carbon.2016.08.026.

242. Thermal Conductivity of common Materials and Gases. https://www.engineeringtoolbox.com/thermal-conductivity-d_429.html. Accessed December 4, 2017.

243. Man Z, Muhammad N, Sarwono A, Bustam MA, Kumar MV, Rafiq S. Preparation of Cellulose Nanocrystals Using an Ionic Liquid. *J Polym Environ*. 2011;19(3):726-731. doi:10.1007/s10924-011-0323-3.

244. Yue Y, Han G, Wu Q. Transitional properties of cotton fibers from cellulose i to cellulose II structure. *BioResources*. 2013;8(4):6460-6471. doi:10.15376/biores.8.4.6460-6471.

245. Zhbankov RG, Firsov SP, Buslov DK, Nikonenko NA, Marchewka MK, Ratajczak H. Structural physico-chemistry of cellulose macromolecules. Vibrational spectra and structure of cellulose. *J Mol Struct*. 2002;614(1-3):117-125. doi:10.1016/S0022-2860(02)00252-1.

246. Sun X, Chi Y, Mu T. Studies on staged precipitation of cellulose from an ionic liquid by compressed carbon dioxide. *Green Chem*. 2014;16(5):2736-2744. doi:10.1039/C4GC00085D.

247. Tran TN, Paul U, Heredia-Guerrero JA, et al. Transparent and flexible amorphous cellulose-acrylic hybrids. *Chem Eng J*. 2016;287(November 2015):196-204. doi:10.1016/j.cej.2015.10.114.

248. Raza MA, Westwood A, Brown A, Hondow N, Stirling C. Characterisation of graphite nanoplatelets and the physical properties of graphite nanoplatelet/silicone composites for thermal interface applications. *Carbon N Y*. 2011;49(13):4269-4279. doi:10.1016/j.carbon.2011.06.002.